

**HYPersonic NONEQUILIBRIUM FLOW SIMULATION
OVER A BLUNT BODY USING BGK METHOD**

A Thesis

by

SUNNY JAIN

Submitted to the Office of Graduate Studies of
Texas A&M University
in partial fulfillment of the requirements for the degree of

MASTER OF SCIENCE

December 2007

Major Subject: Aerospace Engineering

**HYPersonic NONEquilibrium FLOW SIMULATION OVER A
BLUNT BODY USING BGK METHOD**

A Thesis

by

SUNNY JAIN

Submitted to the Office of Graduate Studies of
Texas A&M University
in partial fulfillment of the requirements for the degree of

MASTER OF SCIENCE

Approved by:

Chair of Committee,	Sharath Girimaji
Committee Members,	Adonios Karpetis
Head of Department,	Prabir Daripa
	Helen L. Reed

December 2007

Major Subject: Aerospace Engineering

ABSTRACT

Hypersonic Nonequilibrium Flow Simulation Over a Blunt
Body Using BGK Method. (December 2007)

Sunny Jain, B.Tech., Indian Institute of Technology, Bombay

Chair of Advisory Committee: Dr. Sharath Girimaji

There has been a continuous effort to unveil the physics of hypersonic flows both experimentally and numerically, in order to achieve an efficient hypersonic vehicle design. With the advent of the high speed computers, a lot of focus has been given on research pertaining to numerical approach to understand this physics. The features of such flows are quite different from those of subsonic, transonic and supersonic ones and thus normal CFD methodologies fail to capture the high speed flows efficiently. Such calculations are made even more challenging by the presence of nonequilibrium thermodynamic and chemical effects. Thus further research in the field of nonequilibrium thermodynamics is required for the accurate prediction of such high enthalpy flows.

The objective of this thesis is to develop improved computational tools for hypersonic aerodynamics accounting for non-equilibrium effects. A survey of the fundamental theory and mathematical modeling pertaining to modeling high temperature flow physics is presented. The computational approaches and numerical methods pertaining to high speed flows are discussed.

In the first part of this work, the fundamental theory and mathematical modeling

pertaining to modeling high temperature flow physics is presented. Continuum based approach (Navier Stokes) and Boltzmann equation based approach (Gas Kinetic) are discussed. It is shown mathematically that unlike the most popular continuum based methods, Gas Kinetic method presented in this work satisfies the entropy condition.

In the second part of this work, the computational approaches and numerical methods pertaining to high speed flows is discussed. In the continuum methods, the Steger Warming schemes and Roe's scheme are discussed. The kinetic approach discussed is the Boltzmann equation with Bhatnagar Gross Krook (BGK) collision operator.

In the third part, the results from new computational fluid dynamics code developed are presented. A range of validation and verification test cases are presented. A comparison of the two common reconstruction techniques: Green Gauss gradient method and MUSCL scheme are discussed. Two of the most common failings of continuum based methods: excessive numerical dissipation and carbuncle phenomenon techniques, are investigated. It is found that for the blunt body problem, Boltzmann BGK method is free of these failings.

ACKNOWLEDGMENTS

The completion of this thesis would not have been possible without the contributions of many people. I would like to sincerely thank Dr. Sharath Girimaji for his moral, financial and scientific support during the course of my graduate school. I also thank my committee members, Dr. Prabir Daripa and Dr. Adonios Karpetis, for their support and advice.

I extend thanks to my fellow graduate students involved in this project, Sawan Suman, Dr. Johannes Kerimo and Gaurav Kumar. Success of this project can be undoubtedly attributed to their help and assistance at every phase. I would also like to thank Ben Riley and Tucker Lavin for the invaluable discussions related to this work. Additionally, I would like to thank Dr. Jacques Richard, whose expert knowledge and advice on computational fluid dynamics methods has been invaluable.

I would also like to thank the members of Turbulence Research Group, with whom I had the privilege of working with. They have all helped make graduate school an enjoyable experience for me.

Finally, I would like to thank my family for their support. I wouldn't have even made it to the start of graduate school without my parents, V.K. Jain and Pramila Jain. My brother, Kapil Jain has always been there for me and has been my inspiration. Thanks to everyone, I am very lucky to have all of you in my life.

TABLE OF CONTENTS

	Page
ABSTRACT.....	iii
ACKNOWLEDGMENTS.....	v
TABLE OF CONTENTS.....	vi
LIST OF FIGURES.....	ix
 CHAPTER	
I INTRODUCTION	1
1.1 Computational Approaches	6
1.2 Outline	6
II NAVIER STOKES EQUATIONS	8
2.1 Navier Stokes Equations	8
2.2 Turbulence Modeling	9
2.3 Statistical Turbulence Models	11
2.4 Reynolds Averaged Flow Equations.....	11
2.4.1 Reynolds Averaging	11
2.4.2 Reynolds Averaged Navier Stokes Equations (RANS).....	12
2.5 Favre-Averaged Navier Stokes Equations.....	14
2.5.1 Favre Averaging	14
2.5.2 Favre Averaged Navier Stokes Equations (FANS).....	15
2.6 Eddy Viscosity.....	17
2.7 Classification of Turbulence Models.....	20
2.8 Spalart-Allmaras Turbulence Model	20
2.9 Incompressible Model	21
2.10 Compressible Model	25
2.11 Advantages and Disadvantages of Spalart-Allmaras Model	26

CHAPTER	Page
III BOLTZMANN GAS KINETIC SCHEMES.....	28
3.1 Boltzmann Equation.....	28
3.2 Modeling the Collision Term	32
3.2.1 Compatibility Conditions	34
3.2.2 Entropy Condition	34
3.3 Moments of Boltzmann BGK Equation	36
3.4 Deriving Navier Stokes Equations	40
IV HIGH TEMPERATURE FLOWS: MATHEMATICAL FORMULATIONS AND MODELS.....	48
4.1 Variables and Their Dependencies	48
4.1.1 Conservation of Mass.....	48
4.1.2 Conservation of Momentum.....	48
4.1.3 Conservation of Energy	48
4.2 Physics of Vibrational Nonequilibrium.....	49
4.3 Harmonic and Anharmonic Oscillators	51
4.4 Vibrational Energy Transfer Modes	53
4.4.1 Vibrational Translational EnergyTransfer	54
4.4.2 Vibrational-Vibrational-Translational Transfer	54
4.4.3 Vibrational-Vibrational Transfer	54
4.5 Vibrational Population Distribution	55
4.6 Modeling Vibrational Energy Evolution	57
4.6.1 Multiquantum Transition Approach	58
4.6.2 Landau- Teller Approach.....	60
4.6.3 Ruffin's Model	64
4.6.4 Comparison of the Three Vibrational Models	68
4.7 Chemical Models.....	69
4.7.1 Vibration –Chemistry Coupling	71
4.7.2 Chemistry-Vibration Coupling.....	72
4.7.3 Coupled Vibrational-Chemistry-Vibrational(CVCV) Modeling.....	73
4.8 Transport Models.....	75
V NUMERICAL METHODS: NS, BGK AND SA MODELS.....	83
5.1 Navier Stokes Equations	83

CHAPTER	Page
5.2 Finite Volume Methods	85
5.3 Inviscid Fluxes	88
5.3.1 Steger Warming Schemes.....	88
5.3.2 Roe's Scheme	91
5.4 Boundary Conditions.....	93
5.5 BGK Boltzmann Equation	96
5.6 CollisionTime	98
5.7 Spalart Allmaras Model.....	99
5.8 Boundary and Initial Conditions	100
VI RECONSTRUCTION AND LIMITERS	102
6.1 Introduction	102
6.2 Linear Interpolation	102
6.2.1 MUSCL Based Scheme.....	104
6.2.2 Green Gauss Reconstruction	105
6.3 Limiters	106
6.4 TVD Schemes.....	107
6.4.1 MinMod Limiter.....	110
6.4.2 Van Albada Limiter	111
VII NUMERICAL ISSUES	112
7.1 Introduction	112
7.2 CFD Solver for Nonequilibrium Flow	112
7.3 Grid Generation.....	115
7.4 Time Integration Schemes	117
7.5 Spatial Differencing Schemes	119
VIII RESULTS	122
8.1 Geometric Conservation Law Test	122
8.2 Shock Tube Problem	124
8.3 Viscous Flow over Flat Plate: BGK Scheme	128
8.4 Reconstruction Schemes: Green Gauss and MUSCL Scheme.....	131
8.5 Nonequilibrium Hypersonic Flow over Blunt Body	135

CHAPTER	Page
IX CONCLUSIONS AND SCOPE FOR FUTURE WORK	146
9.1 Conclusions	146
9.2 Scope for Future Work	147
REFERENCES.....	152
VITA.....	160

LIST OF FIGURES

	Page
Figure 1.1: Flow field around a space shuttle reentering the earth's atmosphere.....	2
Figure 1.2: The energy levels in different modes of excitations.....	4
Figure 1.3: Schematic chart for the effects of nonequilibrium.....	5
Figure 3.1: Summary of steps involved in derivation of Boltzmann equation.....	29
Figure 3.2: Parameters used to describe a binary collision.....	30
Figure 3.3: Interparticle forces.....	32
Figure 4.1: Various processes and their interrelations for the case of hypersonic flows..	50
Figure 4.2: Vibrational excitation of molecule A through single quantum transition.....	51
Figure 4.3: Vibrational energy levels for Harmonic Oscillator.....	52
Figure 4.4: Vibrational energy levels for Anharmonic Oscillator.....	53
Figure 4.5: Nonequilibrium vibrational population distribution (expanding flows).....	55
Figure 4.6: Nonequilibrium vibrational population distribution (post shock flows).....	56
Figure 4.7: Overview of derivation for Landau Teller model.....	61
Figure 4.8: Overview of derivation for Ruffin's model.....	65
Figure 4.9: Comparison of the three models.....	69
Figure 4.10: Classification of the chemistry models.....	76
Figure 5.1: Fluxes across the edges of a cell.....	86
Figure 5.2: Flux across a cell interface.....	87

	Page
Figure 5.3: Piecewise-constant reconstruction (Riemann problem).....	92
Figure 5.4: Layout of the ghost cell.....	94
Figure 5.5: Boundary condition for inviscid wall.....	95
Figure 6.1: Left and right states of Q.....	103
Figure 6.2: Gradient at vertex 0 using values of immediate neighbors 1,2, and 3.....	106
Figure 6.3: Example of monotonic and non-monotonic solution.....	107
Figure 6.4: Solution without use of limiter.....	109
Figure 6.5: Solution after using limiter.....	110
Figure 7.1: Basic Steps for a general CFD solver.....	114
Figure 7.2: Timestepping limitations and the methods to eliminate it.....	118
Figure 7.3: Comparison of different Implicit methods.....	119
Figure 7.4: Classification of upwind schemes.....	121
Figure 8.1: Mesh for the channel flow.....	123
Figure 8.2: Pressure profiles along the shock tube.....	125
Figure 8.3: Velocity profiles along the shock tube.....	126
Figure 8.4: Compressive and expansive sonic points.....	127
Figure 8.5: Verification of the Crocco-Busemann relationship.....	129
Figure 8.6: Van Driest profile using BGK scheme.....	130
Figure 8.7: Computational mesh for the blunt body problem.....	131

	Page
Figure 8.8: Normalized temperature profiles along stagnation line.....	132
Figure 8.9: Contour plot for translational temperature using Green Gauss scheme.....	133
Figure 8.10: Contour plot for the translational temperature using MUSCL scheme.....	133
Figure 8.11: Contour plot for the translational temperature using Roe's scheme.....	136
Figure 8.12: Contour plot for the Mach number using Roe's scheme.....	137
Figure 8.13: Contour plot for the translational temperature using Steger Warming....	138
Figure 8.14: Contour plot for the vibrational temperature using Steger Warming.....	139
Figure 8.15: Contour plot for the translational temperature using BGK's scheme.....	139
Figure 8.16: Contour plot for the vibrational temperature using BGK's scheme.....	140
Figure 8.17: Normalized temperature profiles along stagnation line.....	143
Figure 8.18: Normalized vibrational temperature profiles along stagnation line.....	143

CHAPTER I

INTRODUCTION

The feasibility of hypersonic flight depends, to a large extent, on our ability to understand and predict high temperature gas effects on aerodynamics. Key aerodynamic features of hypersonic flows are generally different from those of sub- and super-sonic flows. Over the last several decades, there have been various efforts, both computational and experimental, to unveil hypersonic flow physics. Unlike other flow regimes, hypersonic flight conditions are virtually impossible to replicate in ground-based experiments. Therefore computational fluid dynamics (CFD) can be expected to play a crucial role in the design and development of future hypersonic vehicles.

While CFD methods are mature and sophisticated for subsonic and even supersonic flows, it is quite inadequate in its current form for hypersonic flows. This is due to the fact that computer models of the interaction between high-temperature gas effects and aerodynamics, in general, and turbulence, in particular, are very poor. High temperature gas effects can be categorized into two parts: non-equilibrium thermodynamics and air-chemistry effects. The objective of this thesis is to develop improved computational tools for hypersonic aerodynamics accounting for non-equilibrium effects.

Shocks occur in compressible flows and are characterized by rapid spatial variations (perhaps can be treated as a discontinuity) in velocity, pressure and temperature. Upstream of the shock, the Mach number is high. The upstream kinetic energy is converted in the shock to internal energy. Therefore, downstream of the shock, the

This thesis follows the format of *International Journal of Numerical Methods in Fluids*.

velocity is much lower and pressure and temperature are much higher.

The downstream-to-upstream ratio of thermodynamic variables indicates the shock strength. In hypersonic flows, the shocks are much stronger than in supersonic flows. The resulting high temperatures trigger non-equilibrium effects downstream of the shock. Such a high temperature region can be seen in figure 1.1.

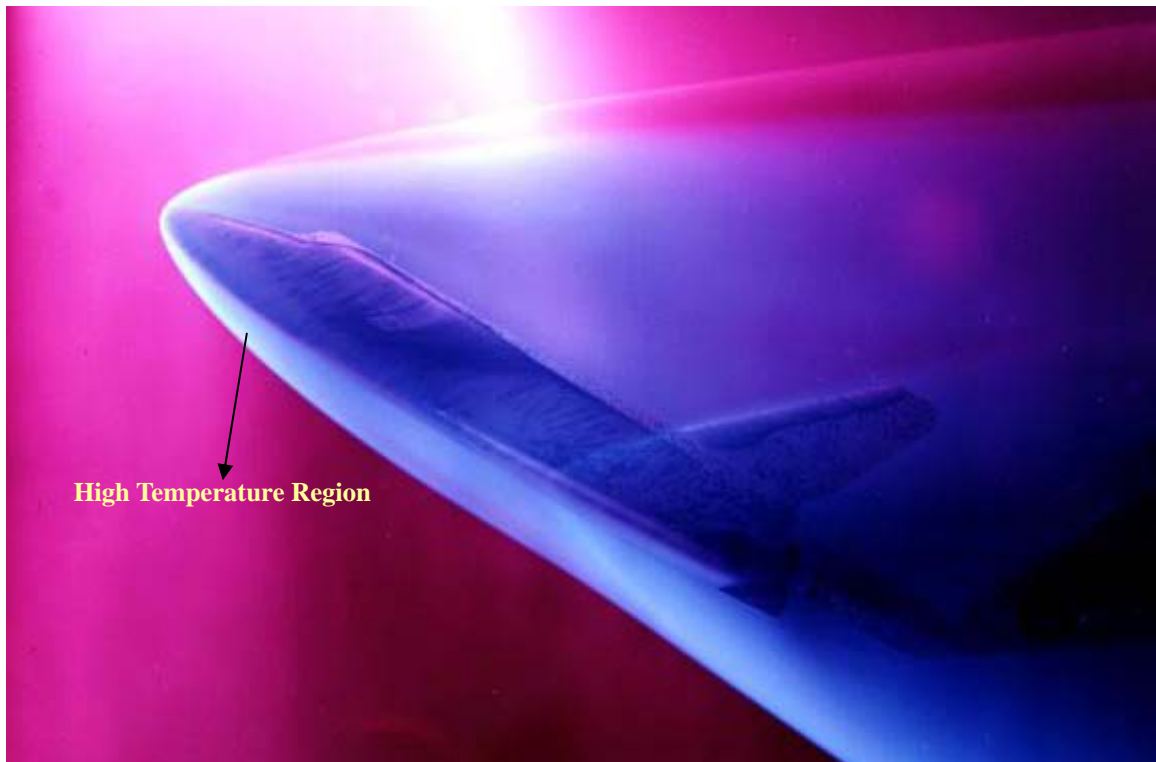


Fig 1.1 Flow field around a space shuttle reentering the earth's atmosphere. The high temperature region is where nonequilibrium of the flow occurs

Internal energy of a gas molecule comprises of translational, rotational, vibrational and electronic forms. These modes can be shown graphically in figure. 1.2. In a gas at

thermodynamic equilibrium, the total internal energy is partitioned equally between the active forms. At high temperatures, all energy forms maybe active. As a volume of gas passes through a shock, the various energy forms must transition from upstream equilibrium condition to downstream equilibrium conditions. Molecular collision brings about this transfer. However, different energy forms equilibrate at different rates. The rate of relaxation from upstream to downstream conditions for the different energy forms are as follows:

$$\tau(\text{trans}) < \tau(\text{rot}) < \tau(\text{vib}) < \tau(\text{elec})$$

In low strength shock typical of low mach numbers, the flow transit time is larger than the time taken for equilibration of various forms of energy from upstream conditions to downstream distributions. As a result, in low-strength shocks, the gas on either side of a shock can be considered to be in equilibrium and equipartition principle is valid on the high temperature side as well.

In strong shocks that occur at high Mach numbers, the flow transit time may be smaller than equilibrium relaxation time. In such a case, the energy form not in equilibrium must be treated appropriately in CFD computations. In this thesis, we will consider hypersonic flow regime in which translational and rotational modes can be reasonably taken to be in equilibrium and electronic form is not active. Thus we will only consider vibrational non-equilibrium.

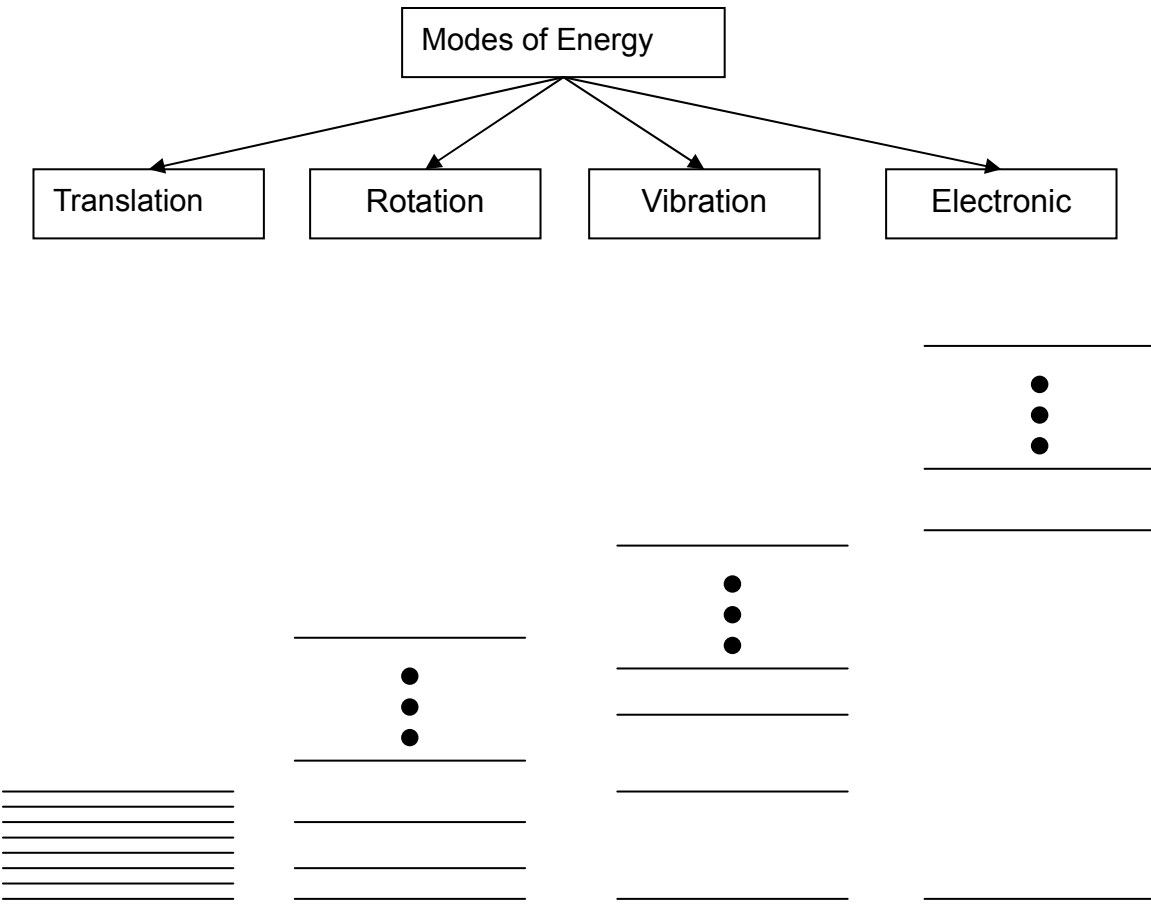


Fig 1.2 The energy levels in different modes of excitations

Overall, it is widely accepted that the problems of hypersonic aerodynamics are characterized not only by exchange of mass, momentum and energy of the fluid flow and its environment, but also by the different internal exchanges of masses and energy (due to chemical reactions and excitation of vibrational DOFs resp.). The effect of nonequilibrium on the physics and computational approach is shown graphically in figure. 1.3 .

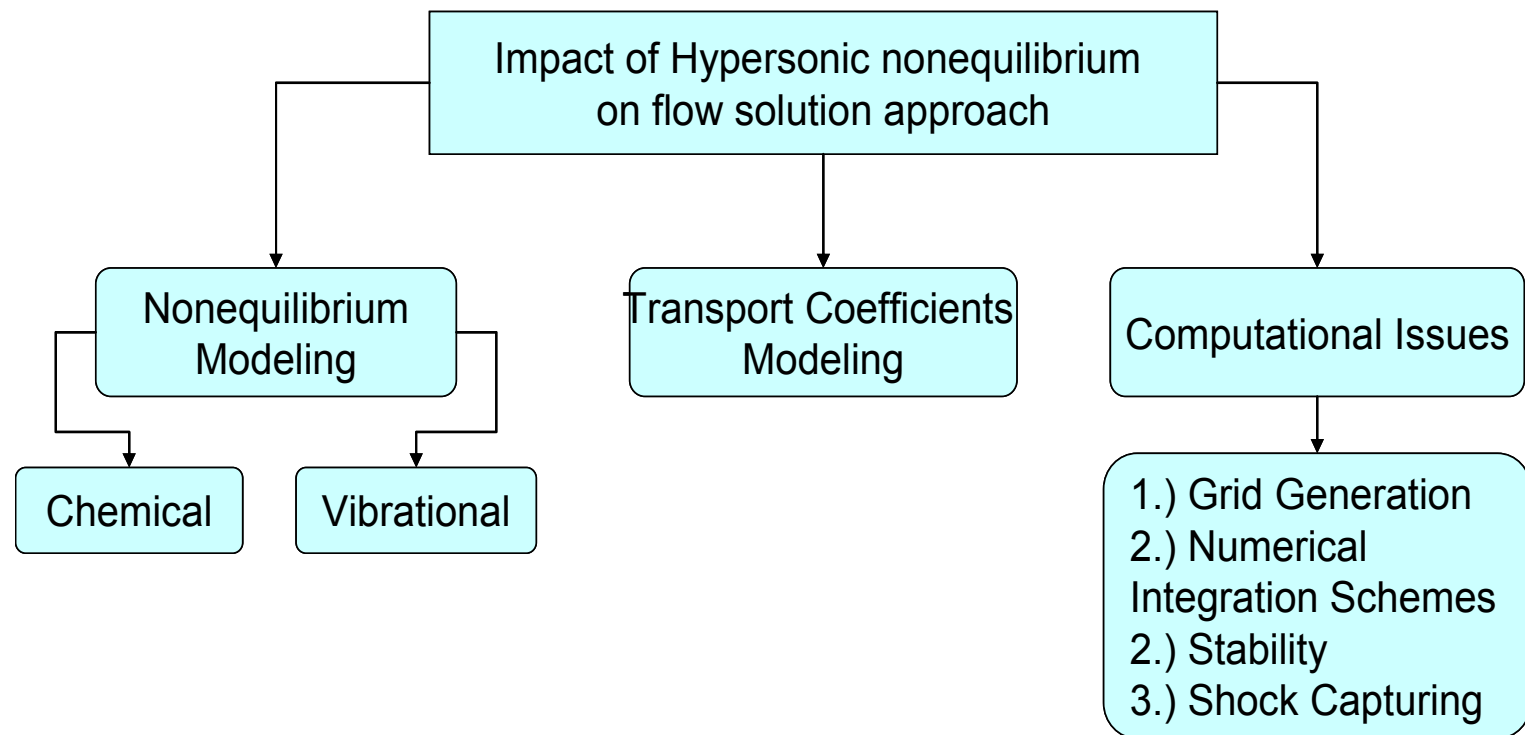


Fig. 1.3 Schematic chart for the effects of nonequilibrium

1.1 Computational Approaches

The experimental modeling of hypersonic vibrational and chemical nonequilibrium flows presents a lot of challenges. The problems arising with the wind tunnels such as HEG (Eitelberg 1994), F4 (Eitelberg et al 1992) and LENS (Holden 1993) are widely known. Thus for such flows, using a computational approach becomes much more attractive.

These approaches are broadly divided into two categories:

- (a) Models based on continuum or macroscopic approaches which were proposed during the 1960's and 1970's [2]
- (b) Models based on kinetic or microscopic approaches using Boltzmann equation, which have been pursued during the last decade (eg. [3])

Simulation of flows with both continuum and non-continuum regions using a hybrid approach is an area of current research. The use of information preserving methods is one such methodology on such problems [61]. A different approach allowing communication between a standard Navier Stokes (NS) code and Direct Simulation Monte Carlo (DSMC) code is also being developed [6].

In this study both the approaches are considered. One of the objectives of this work is to compare the capabilities of BGK method with that of conventional Navier Stokes based methods for the high Mach number regime.

1.2 Outline

The thesis is divided into three parts:

Part A: Fundamental Theory and Mathematical Models

The Navier Stokes equations and the one equation Spalart Allmaras model are described in the second chapter. The third chapter discusses the Boltzmann Gas Kinetic Schemes and the assumptions made in deriving it. The fourth chapter corresponds to the

mathematical models given in literature to numerically simulate the vibrational nonequilibrium effects, chemical nonequilibrium effects and the high temperature effects on the transport coefficients.

Part B: Numerical Methodology

The fifth chapter discusses the numerical methodologies used to implement Navier Stokes model, Boltzmann Gas Kinetic model and Spalart Allmaras turbulence model. The sixth chapter presents reconstruction schemes required for increasing the accuracy of the solvers. Chapter VII presents the CFD techniques: grid generation issues and numerical integration schemes required to solve the Navier Stokes equations for hypersonic flows.

Part C: Results and Conclusions

The results obtained from the Computational Fluid Dynamics (CFD) code are presented in chapter VIII. The code is validated against standard test cases followed by the results for nonequilibrium flow over blunt body. Finally, the conclusions and scope for future work are presented in chapter IX

CHAPTER II

NAVIER STOKES EQUATIONS

2.1 Navier Stokes Equations

The Navier Stokes equations describe the viscous fluid motion by solving for the density, velocity and energy of the fluid particle. For a single species flow, these equations can be represented in 2D as shown in equations and:

$$\frac{\partial Q}{\partial t} + \frac{\partial(G - G_v)}{\partial x} + \frac{\partial(H - H_v)}{\partial y} = 0 \quad (2.1)$$

where

$$Q = \begin{Bmatrix} \rho & \rho u & \rho v & E \end{Bmatrix}^T \quad (2.2)$$

The inviscid matrix G and viscous flow matrix G_v are shown in eq.

$$G = \begin{Bmatrix} \rho u \\ \rho u^2 + p \\ \rho u v \\ (E + p)u \end{Bmatrix}, \quad G_v = \begin{Bmatrix} 0 \\ \tau_{xx} \\ \tau_{xy} \\ \tau_{xx}u + \tau_{xy}v - q \end{Bmatrix} \quad (2.3)$$

Expressions for matrix H and viscous matrix H_v are obtained by the cyclic arrangement of the velocity and spatial components. The other variables used in the literature are expressed in equations through

$$E = \rho C_v T + \frac{1}{2} \rho |\bar{u}|^2 \quad (2.4)$$

$$\tau_{ij} = \mu \left(\frac{\partial u_i}{\partial x_j} + \frac{\partial u_j}{\partial x_i} \right) + \delta_{ij} \lambda' \frac{\partial u_k}{\partial x_k}, \quad \lambda' = -\frac{2}{3} \mu \quad (2.5)$$

$$\vec{q} = -\kappa \nabla T \quad (2.6)$$

$$P = \rho R T \quad (2.7)$$

In the finite volume method, the integral form of Navier Stokes equation is more applicable and is represented as in equations and

$$\frac{\partial}{\partial t} \int_V Q dV + \int_S F \cdot d\vec{S} = 0 \quad (2.8)$$

$$F = G\vec{i} + H\vec{j} \quad (2.9)$$

where S and V is the boundary and volume, which for 2D case is parameter and the area of the cell.

2.2 Turbulence Modeling

Most practical engineering problems involving fluid flows are turbulent in nature. At a very basic level, turbulence can be interpreted as a collection of eddies or vortices, of different sizes and strengths, giving the flow a random appearance. Turbulence often originates as instability of laminar flows when the Reynolds number becomes too high. The instabilities are related to interaction between viscous terms and nonlinear inertia

terms in the equations of motion, the mechanism for which is complicated. It is very difficult to give a precise definition of turbulence. However, one can enlist some of the characteristics exhibited by turbulent flows [82]:

- 1.) Irregularity: Due to the randomness of the flow, it is impossible to use deterministic approach to turbulence problems and one has to rely on statistical methods.
- 2.) Diffusivity: Turbulence amplifies the diffusivity and hence enhances the mixing of flows as well as increases the heat transfer rates.
- 3.) Three-dimensional vorticity fluctuations: Turbulence is rotational and three dimensional and is characterized by high levels of fluctuating vorticity. Therefore vorticity dynamics plays an important role in the description of turbulent flows.
- 4.) Dissipation: Turbulent flows are always dissipative and the dissipation occurs at the smaller scales or smaller eddies. Therefore turbulence requires a continuous supply of energy for sustenance.
- 5.) Large Reynolds Number: As mentioned before, turbulence always occurs at high Reynolds numbers.

The prediction of turbulence computationally becomes a challenging task because of the presence of wide range of scales. To incorporate the physics of such a wide spectrum, one needs to solve the fluid flow governing equations on very large grids. One also requires an exceptionally accurate discretization method so that both large and small scale aspects of turbulence can be captured. Such an approach is called the Direct Numerical Simulation (DNS) of turbulence. Although DNS has been used to give accurate prediction of turbulence in the past, it still needs tremendous amount of computing resources. Hence, it is not feasible for most of the practical problems.

In an attempt to alleviate the computational burden, the approach of Large Eddy Simulation (LES) is used. In this approach, the large energy containing scales of turbulence are resolved or explicitly calculated, whereas the small scales of turbulence which are more universal in nature are modeled. Although LES is more feasible compared to DNS, both LES and DNS require enormous computing resources. With the increase in computing power, it is expected that these approaches will gain even more popularity.

2.3 Statistical Turbulence Models

Currently, the most popular approaches for turbulence modeling are the statistical turbulence models. In this approach, the flow quantities are broken down into a mean and a fluctuating part. The equations are then averaged over time thus resulting in a set of mean flow equations. Statistics of the fluctuating field influence the mean flow evolution. Based on the type of averaging method, two kinds of averaged equations can be obtained. These are discussed in the next two sections.

2.4 Reynolds Averaged Flow Equations

2.4.1 Reynolds Averaging

The Reynolds Averaging method was introduced by Reynolds (1895). Here averaging can represent ensemble, time or space average. Let $F(t)$ be the instantaneous value of a flow variable. The Reynolds average is defined as the following ensemble average:

$$\langle F(t) \rangle_N \equiv \frac{1}{N} \sum_{n=1}^N F^{(n)}(t), \quad (2.9)$$

where $F^{(n)}(t)$ is the measurement on the n th realization. This type of averaging is most general, but the experiment has to be replicated N times, where N should be very large.

In simulation of statistically homogenous flow in a cubic domain of side L , the above average can be approximated using the spatial averages, which are defined as

$$\langle F(t) \rangle_L \equiv \frac{1}{L^3} \iiint_0^L F(x, t) dx_1 dx_2 dx_3 \quad (2.10)$$

The most commonly used definition is the time averaging. This technique is applicable for statistically stationary flows. The average over a time interval T is defined as

$$\langle F(x, t) \rangle_T \equiv \frac{1}{T} \int_t^{t+T} F(x, t') dt' \quad (2.11)$$

As $T \rightarrow \infty$ the time average approaches the ensemble average.

Thus any of the flow variables, for example, the velocity field can be broken down into its average and fluctuating components.

$$u_i(x, t) = U_i(x) + u_i'(x, t)$$

where $u_i'(x, t)$ is the fluctuation and $U_i(x, t)$ is the averaged part which can be defined using any of the above definitions given in equations , and .

2.4.2 Reynolds Averaged Navier Stokes Equations (RANS)

The Navier Stokes Equations for unsteady incompressible flows are given as

$$\begin{aligned} \frac{\partial u_i}{\partial x_i} &= 0 \\ \rho \frac{\partial u_i}{\partial t} + \rho \frac{\partial(u_j u_i)}{\partial x_j} &= -\frac{\partial p}{\partial x_i} + \frac{\partial \tau_{ji}}{\partial x_j} \end{aligned} \quad (2.12)$$

where u_i , x_i are velocity and position, t is time, p is pressure, ρ is density and τ_{ij} is viscous stress and is given in terms of strain rate tensor as:

$$\tau_{ij} = \mu \left(\frac{\partial u_i}{\partial x_j} + \frac{\partial u_j}{\partial x_i} \right)$$

Averaging these equations leads to the Reynolds Averaged Navier Stokes:

$$\begin{aligned} \frac{\partial \bar{u}_i}{\partial x_i} &= 0 \\ \rho \frac{\partial \bar{u}_i}{\partial t} + \rho \frac{\partial(\bar{u}_j \bar{u}_i)}{\partial x_j} &= -\frac{\partial \bar{p}}{\partial x_i} + \frac{\partial(\bar{\tau}_{ji} - \rho \bar{u}_j \bar{u}_i)}{\partial x_j}, \end{aligned} \quad (2.13)$$

$$\text{where } \bar{\tau}_{ij} = \mu \left(\frac{\partial \bar{u}_i}{\partial x_j} + \frac{\partial \bar{u}_j}{\partial x_i} \right).$$

The only unknown quantity in the above equations is the correlation term $\tau_{ij}^{turb} = -\rho \bar{u}_j \bar{u}_i$. This term is known as the Reynolds stress tensor. Therefore the turbulence is introduced in the mean flow equations by the presence of this new term. It can be seen that τ_{ij}^{turb} is a symmetric tensor and introduces six new components in the system. The number of equations are, however still the same. Thus the system is not closed and the correlation terms need to be modeled.

2.5 Favre-Averaged Navier Stokes Equations

2.5.1 Favre Averaging

In compressible flows, the density and temperature fluctuations are significant and should be taken into account. Therefore, applying the Reynolds Averaging technique to the compressible Navier-Stokes (NS) equations produces many new correlation terms such as $\overline{\rho' u_i}$ and $\overline{\rho' T_i}$ etc. An alternative way to average the compressible NS equations is the Favre averaging, suggested by Favre (1965).

The Favre Average for a quantity u_i can be given as

$$\tilde{u}_i \equiv \frac{\langle \rho u_i \rangle_N}{\langle \rho \rangle_N} = \frac{\sum_{n=1}^N (\rho u_i)^{(n)}}{\sum_{n=1}^N \rho^{(n)}} \quad (2.14)$$

Similar to the Reynolds Averaging, the Favre average can be approximated using spatial and time averages defined as:

Spatial averaging for statistically homogeneous flows:

$$\tilde{u}_i \equiv \frac{\langle \rho u_i \rangle_L}{\langle \rho \rangle_L} = \frac{\int_0^L \int_0^L \int_0^L \rho u_i dx_1 dx_2 dx_3}{\int_0^L \int_0^L \int_0^L \rho dx_1 dx_2 dx_3}$$

Time averaging for statistically stationary flows:

$$\tilde{u}_i \equiv \frac{\langle \rho u_i \rangle_T}{\langle \rho \rangle_T} = \frac{\int_t^{t+T} \rho u_i dt}{\int_t^{t+T} \rho dt}$$

One can break down the instantaneous velocity component into its Favre Averaged part and the fluctuating part, i.e., $u_i = \tilde{u}_i + \tilde{u}_i''$. If both sides are scaled with density and Reynolds averaging is done, the following can be obtained

$$\overline{\rho u_i} = \bar{\rho} \tilde{u}_i + \overline{\rho u_i''}$$

$$\text{i.e., } \overline{\rho u_i''} = 0$$

where the Reynolds average $\langle F \rangle$ is denoted by \bar{F} .

2.5.2 Favre Averaged Navier Stokes Equations (FANS)

The compressible Navier Stokes Equations can be written as

$$\begin{aligned} \frac{\partial \rho}{\partial t} + \frac{\partial (\rho u_i)}{\partial x_i} &= 0 \\ \frac{\partial (\rho u_i)}{\partial t} + \frac{\partial (\rho u_j u_i)}{\partial x_j} &= -\frac{\partial p}{\partial x_i} + \frac{\partial \tau_{ji}}{\partial x_j}, \\ \frac{\partial (\rho(e + u_i u_i / 2))}{\partial t} + \frac{\partial (\rho u_j (h + u_i u_i / 2))}{\partial x_j} &= -\frac{\partial q_j}{\partial x_j} + \frac{\partial (u_i \tau_{ij})}{\partial x_j} \end{aligned} \quad (2.15)$$

where,

$$\tau_{ij} = 2\mu s_{ij} + \lambda \frac{\partial u_k}{\partial x_k} \delta_{ij} = 2\mu \left(s_{ij} - \frac{1}{3} \frac{\partial u_k}{\partial x_k} \delta_{ij} \right),$$

$$s_{ij} = \frac{1}{2} \left(\frac{\partial u_i}{\partial x_j} + \frac{\partial u_j}{\partial x_i} \right)$$

$$e = C_v T, \quad h = e + p / \rho = C_p T, \quad p = \rho R T$$

$$q_j = -\kappa \frac{\partial T}{\partial x_j} = -\frac{\mu}{\text{Pr}} \frac{\partial h}{\partial x_j}, \quad \text{Pr} = \frac{\mu C_p}{\kappa}$$

For the averaging of equations, the above variables are decomposed as follows:

$$u_i = \tilde{u}_i + u_i''$$

$$\rho = \bar{\rho} + \rho'$$

$$p = \bar{p} + p'$$

$$h = \tilde{h} + h''$$

$$e = \tilde{e} + e''$$

$$T = \tilde{T} + T''$$

$$q_j = \bar{q}_j + q_j'$$

Substituting these values followed by averaging the resulting equations, one can get Favre Averaged Navier Stokes (FANS) equations:

$$\begin{aligned}
\frac{\partial \bar{\rho}}{\partial t} + \frac{\partial(\bar{\rho}\tilde{u}_i)}{\partial x_i} &= 0 \\
\frac{\partial(\bar{\rho}\tilde{u}_i)}{\partial t} + \frac{\partial(\bar{\rho}\tilde{u}_j\tilde{u}_i)}{\partial x_j} &= -\frac{\partial \bar{p}}{\partial x_i} + \frac{\partial(\bar{\tau}_{ji} - \overline{\rho u_j' u_i'})}{\partial x_j}, \\
\frac{\partial(\bar{\rho}(\tilde{e} + \tilde{u}_i\tilde{u}_i/2) + \overline{\rho u_i' u_i'})/2}{\partial t} + \frac{\partial(\bar{\rho}\tilde{u}_j(\tilde{h} + \tilde{u}_i\tilde{u}_i/2) + \tilde{u}_j \overline{\rho u_i' u_i'})/2}{\partial x_j} &= \\
\frac{\partial(-\bar{q}_j - \overline{\rho u_j' h} + \overline{\tau_{ji} u_i'} - \overline{\rho u_j' u_i' u_i'}/2)}{\partial x_j} + \frac{\partial(\tilde{u}_i(\bar{\tau}_{ij} - \overline{\rho u_i' u_j'}))}{\partial x_j} &
\end{aligned} \tag{2.16}$$

where,

$$\bar{p} = \bar{\rho}R\tilde{T}, \quad \tilde{e} = C_v\tilde{T}, \quad \tilde{h} = C_p\tilde{T}, \quad \bar{q}_j = -\kappa \frac{\partial \tilde{T}}{\partial x_j}$$

There are 26 unknowns introduced due to averaging whereas the number of equations is still 5. Therefore, the unknown terms need to be modeled in order to close the terms. It is remarkable that Reynolds averaging of the compressible NS equations would have led to an even higher number of new correlations. This explains the popularity of Favre averages for compressible flows.

2.6 Eddy Viscosity

The RANS momentum equation for incompressible flow derived in previous section can be written as

$$\rho \frac{\partial \bar{u}_i}{\partial t} + \rho \frac{\partial(\bar{u}_j \bar{u}_i)}{\partial x_j} = -\frac{\partial \bar{p}}{\partial x_i} + \frac{\partial(\bar{\tau}_{ji} - \overline{\rho u_j' u_i'})}{\partial x_j} \tag{2.17}$$

The viscous stress is given as

$$\bar{\tau}_{ij} = \mu \left(\frac{\partial \bar{u}_i}{\partial x_j} + \frac{\partial \bar{u}_j}{\partial x_i} \right)$$

An analogy can be drawn between the correlation term $\rho \bar{u}_j \bar{u}_i$ and the viscous stress term to get the following expression for the correlation term:

$$\bar{\tau}_{ij}^{turb} = \rho \bar{u}_j \bar{u}_i = \mu^{turb} \left(\frac{\partial \bar{u}_i}{\partial x_j} + \frac{\partial \bar{u}_j}{\partial x_i} \right) \quad (2.18)$$

Therefore the total stress term can be denoted as $\bar{\tau}_{ij}^{total} = \bar{\tau}_{ij}^{viscous} + \bar{\tau}_{ij}^{turb}$.

Thus, the RANS equations for incompressible flows become exactly the same as Navier Stokes equations for laminar flows by just replacing the viscosity by effective viscosity given as $\mu^{eff} = \mu + \mu^{turb}$. Therefore, if eddy viscosity μ^{turb} is known, the RANS system of equations is closed and can be solved using the same methodology as for laminar Navier Stokes Equations.

In case of Favre averaged equations for compressible flows, making such a substitution for viscosity does not lead to the recovery of laminar compressible NS equations. However, the above analogy can still be applied for FANS equations if following assumptions are made:

- a) Turbulent kinetic energy is negligible compared to the mean enthalpy, i.e.

$$\bar{\rho}k = \frac{1}{2} \overline{\rho u_i'' u_i''} \ll \bar{\rho} \tilde{e}$$

This assumption is reasonable for all flows below the hypersonic regime. Even in hypersonic regime, this assumption holds well if the flow is continuously contracting and the free stream flow had negligible turbulent kinetic energy.

- b) The molecular diffusion $\overline{\tau_{ji}'' u_i''}$ and turbulent transport $\frac{1}{2} \overline{\rho u_j'' u_i'' u_i''}$ are neglected in the energy equation. The molecular diffusion can be safely neglected since it is small when compared to the following term:

$$\overline{\tau_{ji}'' u_i''} < \overline{\tau_{ji}'' u_i''}$$

On the other hand the turbulent transport would be negligible if assumption (a) holds true.

- c) It is also assumed that the heat flux term can be represented as

$$q_j^{turb} = \overline{\rho u_j'' h''} = -\frac{\mu^{turb}}{\text{Pr}^{turb}} \frac{\partial \tilde{h}}{\partial x_j}$$

where Pr^{turb} is the turbulent Prandtl number.

- d) The Favre averaged Reynolds Stress tensor can be represented as

$$\tau_{ij}^{turb} = -\overline{\rho u_j'' u_i''} = 2\mu^{turb} \left(\overline{s}_{ij} - \frac{1}{3} \frac{\partial u_k}{\partial x_k} \delta_{ij} \right) - \frac{2}{3} \bar{\rho} k \delta_{ij}$$

The term $2\bar{\rho}k\delta_{ij}/3$ can be ignored on the basis of assumption (a).

Thus after making the above assumptions the Navier Stokes Equations can be recovered from FANS equation by making the following substitutions:

$$\mu^{eff} = \mu + \mu^{turb}$$

$$\left(\frac{\mu}{Pr}\right)^{eff} = \frac{\mu}{Pr} + \frac{\mu^{turb}}{Pr^{turb}}$$

2.7 Classification of Turbulence Models

The objective of turbulence models is to provide closure for the RANS or FANS equations. Depending on the number of differential equations needed for closure, the turbulence models can be classified as

- (a) Zero Equation or Algebraic Models
- (b) One Equation Models
- (c) Two Equation Models
- (d) Stress Equation Models

The models (a)-(c) are based on the eddy viscosity approximation discussed in the last section. However the models of class (d) solve the Reynolds Stress terms directly by solving the corresponding evolution equation (wherein the higher order terms are required to be modeled). Currently the one equation and two equation models are popular approaches for engineering problems involving turbulence. In this study, the turbulence model discussed belongs to the category (b), i.e. one equation model.

2.8 Spalart-Allmaras Turbulence Model

The Spalart-Allmaras model [83] is a one equation model for turbulent viscosity for incompressible as well as compressible flows. This model was first developed in 1992 and uses Baldwin and Barth's [84] model as a framework. The key modification made in Spalart-Allmaras (SA) model is the approach used for determining the near wall semi-local term. Its formulation and coefficients were defined using dimensional

analysis, Galilean invariance, and selected empirical results. The empirical results used were the 2-D mixing layers, wakes and flat plate boundary layer flows.

One of the objectives of this model was to improve upon the predictions obtained with zero equation or algebraic mixing length models in order to develop a local model for complex flows. It also provides a simpler alternative to two equation turbulence models.

The model uses distance from the nearest wall in its formulation and has provision of including a smooth laminar to turbulent transition assuming that the transition point is known.

2.9 Incompressible Model

The eddy viscosity function ν_t is given in terms of eddy viscosity variable $\tilde{\nu}$ and the wall function f_{vl} as

$$\nu_t = \tilde{\nu} f_{vl}(\chi) \quad (2.19)$$

where $\chi = \tilde{\nu}/\nu$.

The function f_{vl} is formulated such that away from the wall boundaries, its value becomes one.

$$f_{vl}(\chi) = \frac{\chi^3}{(\chi^3 + C_{vl}^3)} \quad (2.20)$$

where $C_{vl} = 7.1$ is a constant.

The convective transport equation of the eddy viscosity is modeled as

$$\frac{D\tilde{v}}{Dt} = b_{prod}(S, \tilde{v}, d) - b_{dest}(\tilde{v}, d) + b_{trip}(d_T) + b_{dif}(\tilde{v}) \quad (2.21)$$

The terms on the RHS are as follows:

1) Production Term $b_{prod}(S, \bar{v}, d)$

The eddy viscosity production term is related to the vorticity. This choice allows good modeling of the near wall flows but is not consistent with the homogeneous turbulence behavior. The production term is defined as

$$b_{prod} = c_{bl}[1 - f_{t2}(\chi)]\tilde{S}\tilde{v},$$

$$\tilde{S} = S + \frac{\bar{v}}{k^2 d^2} f_{v2}(\chi)$$

Here, S is the magnitude of the mean vorticity and f_{v2} is another damping function defined as

$$f_{v2}(\chi) = 1 - \frac{\chi}{1 + \chi f_{vl}(\chi)}$$

k is the von Karman's constant and its value is 0.41,

c_{bl} is calibration constant with value 0.1355

f_{t2} is related to transition modeling.

2) Destruction Term $b_{dest}(\bar{v}, d)$

In a boundary layer, the blocking effect of a wall is felt at a distance through the pressure term, which acts as the main destruction term for the Reynolds shear stress.

Therefore the wall distance d appears directly in the expression for destruction term, which is given as

$$b_{dest} = [c_{wl} f_w(r) - \frac{c_{b1}}{k^2} f_{t2}(\chi)] (\frac{\tilde{\nu}}{d})^2,$$

$$r = \frac{\tilde{\nu}}{\tilde{S} k^2 d^2}$$

The role of the function f_w is to provide with a better calibration in the outer region of boundary layer, and is defined as

$$f_w(r) = g(r) \left[\frac{1 + c_{w3}^6}{g(r)^6 + c_{w3}^6} \right]^{\frac{1}{6}},$$

$$g(r) = r + c_{w2}(r^6 - r)$$

Here, $c_{w2} = 0.2$, $c_{w3} = 2.0$ and c_{wl} is given as

$$c_{wl} = \frac{c_{b1}}{k^2} + \frac{1 + c_{b2}}{\sigma}$$

3) Trip term $b_{trip}(d_T)$

The transition to turbulence is achieved due to the presence of two terms. The first term is the function $f_{t2}(\chi)$ used in the expressions for production and destruction terms. The function of this term is to restrict the eddy viscosity in the regions where $\tilde{\nu} < \nu / 2$. Therefore if eddy viscosity is initialized to a small value in some region, turbulence will not develop. The second term used for transition is the source term or the trip term defined as

$$b_{trip} = f_{t1} \Delta u^2, \\ f_{t1} = c_t g_t \exp(-c_{t2} \frac{w_t^2}{\Delta u^2} [d^2 + g_t^2 d_t^2])$$

Here, Δu is the norm of difference between the velocities at the transition point and the field point being considered,

Δx_t is the grid spacing along the wall at the location of the trip,

ω_t is the vorticity at the wall at the transition point,

c_{t1} and c_{t2} are two calibration constants with $c_{t1} = 1$, $c_{t2} = 2$ and g_t is given as

$$g_t = \min\left(0.1, \frac{\Delta u}{\omega_t \Delta x_t}\right)$$

Near the transition point, the trip term produces a positive peak in the eddy viscosity production overcoming the limit imposed by the function f_{t2} on the eddy viscosity increase. Therefore, the turbulent region spreads from the transition point by means of the convective terms. Once steady state is reached, turbulent flow is obtained in the region downstream of the transition point while the upstream region remains laminar. However, one needs to know the transition point beforehand.

4.) Diffusion terms $b_{dif}(\tilde{v})$

The diffusion term is expressed as

$$b_{dif}(\tilde{v}) = \frac{1}{\sigma} [\nabla \cdot ((\nu + \tilde{v}) \nabla \tilde{v}) + c_{b2} (\nabla \tilde{v})^2]$$

For numerical efficiency, these terms are rearranged as

$$\begin{aligned} b_{dif}(\tilde{v}) &= \frac{1+c_{b2}}{\sigma} \nabla \cdot [(\nu + \tilde{v}) \nabla \tilde{v}] - \frac{c_{b2}}{\sigma} \nabla^2 \tilde{v} - \frac{c_{b2}}{\sigma} (\nabla \nu) (\nabla \tilde{v}) \\ &\approx \frac{1+c_{b2}}{\sigma} \nabla \cdot [(\nu + \tilde{v}) \nabla \tilde{v}] - \frac{c_{b2}}{\sigma} \nabla^2 \tilde{v} \end{aligned}$$

The term $\frac{c_{b2}}{\sigma} (\nabla \nu) (\nabla \tilde{v})$ is small and can be neglected.

The alternate form avoids discretization of the term $(\nabla \tilde{v})^2$, which does not easily results in positive discrete operators.

The constant σ has value $2/3$, and $c_{b2} = 0.622$.

2.10 Compressible Model

The formulation for compressible model is almost the same as the incompressible one except for a few modifications to account for the change in density. The expression of eddy viscosity function is modified to the following

$$\nu_t = \rho \tilde{v} f_{vl}(\chi) \quad (2.21)$$

where ρ is the local mean density.

The convective transport equation of the eddy viscosity is modified to give the following equation:

$$\rho \frac{D\tilde{v}}{Dt} = \rho b_{prod}(S, \tilde{v}, d) - \rho b_{dest}(\tilde{v}, d) + \rho b_{trip}(d_T) + b'_{dif}(\tilde{v}) \quad (2.22)$$

The definitions of production, destruction and trip term are the same as for the incompressible model. However, the diffusion term is defined as

$$b_{dif}(\tilde{v}) = \frac{1}{\sigma} [\nabla \cdot ((\mu + \rho \tilde{v}) \nabla \tilde{v}) + c_{b2} \rho (\nabla \tilde{v})^2]$$

To avoid discretization of $(\nabla \tilde{v})^2$, the above expression is rearranged to give

$$b_{dif}(\tilde{v}) = \frac{1}{\sigma} [\nabla \cdot ((\mu + \rho \tilde{v}) \nabla \tilde{v}) + c_{b2} \{\rho \nabla \cdot (\tilde{v} \nabla \tilde{v}) - \rho \tilde{v} \nabla^2 \tilde{v}\}]$$

In this thesis work, we use the compressible SA model. Its numerical implementation is described next.

2.11 Advantages and Disadvantages of Spalart-Allmaras Model

The following advantages can be listed for the Spalart-Allmaras model:

- 1.) It does not require a finer grid near wall as required for the two-equation models.
- 2.) It is computationally inexpensive as well as simpler compared to the two-equation models since only one extra equation needs to be solved.
- 3.) It is applicable to free shear flows as well as viscous flows past solid bodies.
- 4.) Gives very good predictions in 2-D mixing layers, wake flows, flat plate boundary layer, wake region and shows improvements in the prediction of flows with adverse pressure gradient compared to the two equation models.

Some of the drawbacks of the model are:

- 1.) The model does not give very accurate predictions for jet flows.
- 2.) The model only predicts the turbulent shear term ($\rho \overline{u'v'}$) but cannot predict the turbulent kinetic energy.
- 3.) It is generally inadequate for more complex flows.

CHAPTER III

BOLTZMANN GAS KINETIC SCHEMES

3.1 Boltzmann Equation

In the continuum formulation leading to the Navier-Stokes equations, the constitutive relations between viscous stress and velocity gradients and heat flux and temperature gradient are taken as assumptions that can be verified by experiment. However, another logical approach to predict the fluid flow would be by following the dynamical trajectories of individual molecules from given initial conditions. This is only feasible in rarefied medium especially in the free molecular regime. Direct Simulation Monte Carlo(DSMC) is a well developed tool for such rarefied gas flows. For the problems of our present interest, any significant volume of gas will contain molecules of the order of Avogadro number, making the latter approach impossible to solve computationally.

Another approach would be to concentrate on the distribution function where statistically averaged quantities are of interest rather than dealing with individual particles. Thus we require an equation which describes the rate of change with respect to position and time of the distribution function. The Boltzmann Equation provides us with such a relation and it represents the time evolution of distribution function $f(c_i, x_i, t)$ in one particle phase space. To derive this equation we start with the more general Liouville Equation. A summary of the derivation is shown in the figure. 3.1.

The Boltzmann equation in the final form can be written as

$$\frac{\partial}{\partial t} \left[f_{x_1}(\underline{q}, \underline{c}; t) \right] + \sum_{k=1}^3 c_k \frac{\partial \left[f_{x_1}(\underline{q}, \underline{c}; t) \right]}{\partial q_k} = \\ \int_{-\infty}^{+\infty} \int_0^{2\pi} \int_0^{\pi/2} \left[f_{x_1}(\underline{q}, \underline{c}') f_{x_1}(\underline{q}, \underline{z}') - f_{x_1}(\underline{q}, \underline{c}) f_{x_1}(\underline{q}, \underline{z}) \right] g d^2 \sin \psi \cos \psi d\psi d\varepsilon d\underline{z}$$

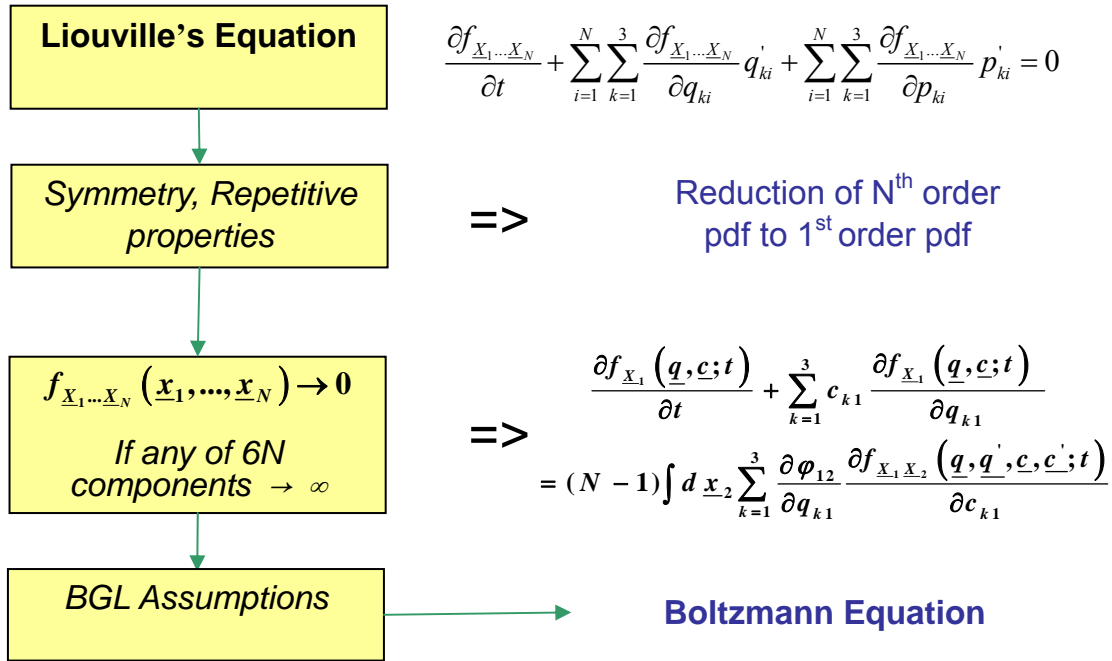


Fig 3.1 Summary of steps involved in derivation of Boltzmann equation

Here, $f_{\underline{X}_1}(\underline{q}, \underline{c}; t)$ represents the distribution function such that the quantity $f_{\underline{X}_1}(\underline{q}, \underline{c}; t) dq dc$ represents the expected number of molecules in volume element dq in physical space and dc in velocity space; $q = (q_1, q_2, q_3)$ is the position vector; and $c = (c_1, c_2, c_3)$ is the velocity vector.

The quantities on the right hand side of Boltzmann equation represent the parameters involved in binary collision of any two molecules in the system. These parameters are depicted in figure 3.2.

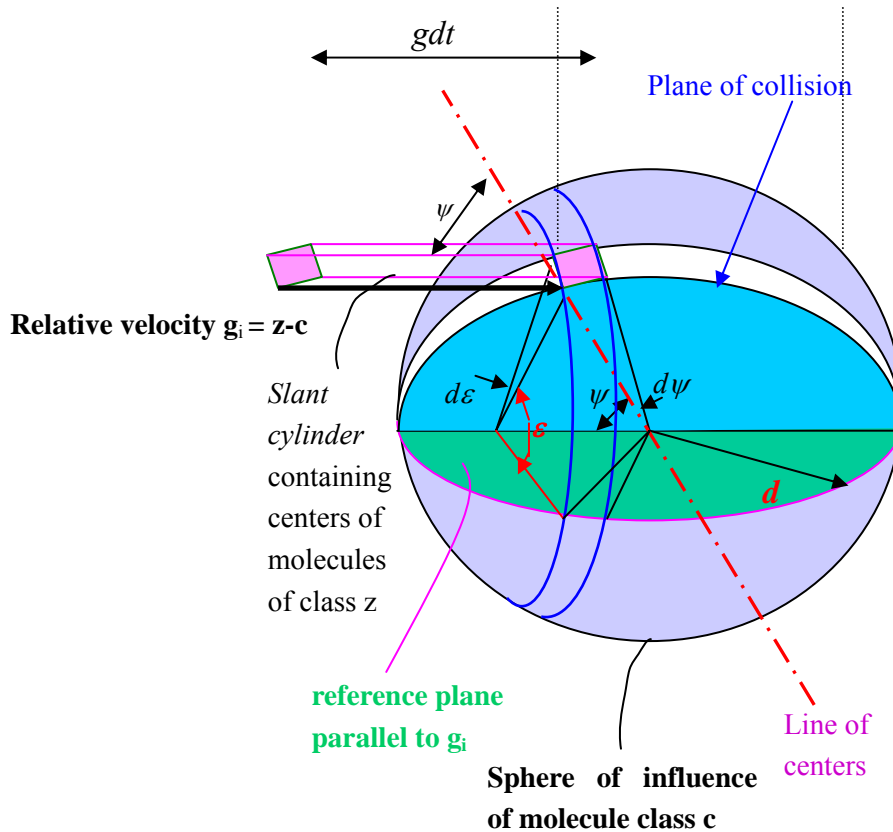


Fig 3.2 Parameters used to describe a binary collision

The terms in the final form of Boltzmann equation can be interpreted as follows:

$\sum_{k=1}^3 c_k \frac{\partial [f_{x_1}(q, \underline{c}; t)]}{\partial q_k} dqdc$: Represents the net flux of molecules that are in the velocity

range dV_c across the six surfaces of dV_x . Therefore this term represents the convective flux in the physical space.

The integration term on the RHS represents the rate of increase of the number of molecules of class c resulting from collisions.

As shown in figure 3.1, the Boltzmann Equation is only applicable to cases which satisfy the Boltzmann gas limit (BGL), which is a set of following assumptions ([70]):

1.) Dilute Gas Assumption :

The density is sufficiently low so that only binary collisions between the constituent molecules need to be considered.

2.) Slow Spatial dependence of the gas properties

Due to this assumption, the collisions can be thought of as being localized in the physical space.

3.) Interparticle potential is sufficiently short range

As a consequence of this assumption, two molecules only interact with each other when the distance between the molecules is equal to the sum of their radii. This effect is shown in the figure 3.3, where the long range forces are zero for distances greater than d . Therefore, the consequence of the first assumption is further reinforced and collisions involving three or more molecules can be safely neglected.

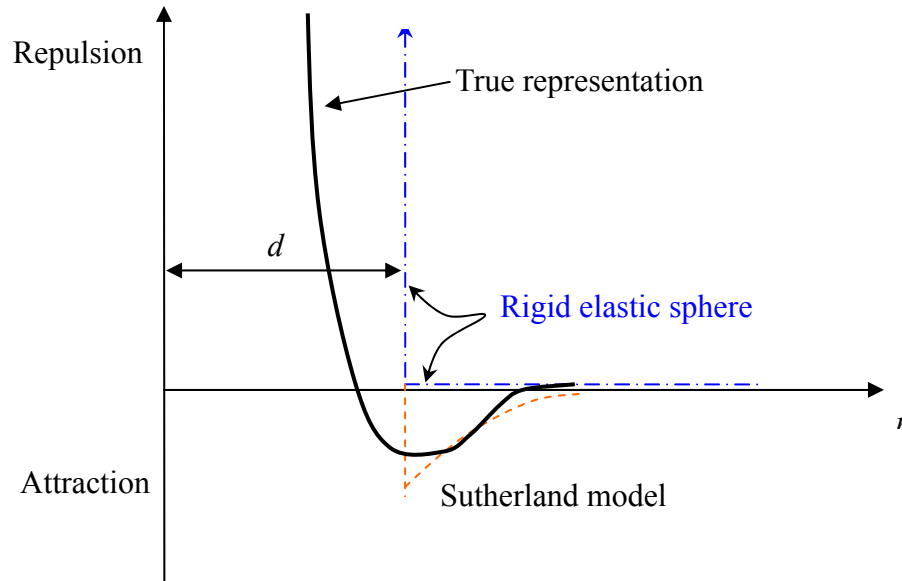


Fig 3.3 Interparticle forces

3.2 Modeling the Collision Term

As shown in last section, the classical Boltzmann equation is a nonlinear integral-differential equation and is difficult to solve. Thus in order to use the Boltzmann kinetic based approach for fluid flow simulations, the complicated collision term needs to be modeled with a simpler expression without sacrificing the accuracy of the method. One can find a few models developed on this idea in the literature: Chapman Enskog method, model equation method, moment methods, Monte Carlo Methods, and the BGK method.

In the BGK method, the basic idea is to find a simplified collision term which emulates the following properties of the actual collision term:

- (a) The approximate collision term should satisfy the compatibility conditions.

This property follows from the properties of elastic collisions of molecules. In a system of N molecules, the collision is a process internal to the system and should not affect the total mass, momentum and energy of the system.

(b) It should satisfy the entropy condition.

This follows from the second law of thermodynamics and the approximate collision term should not violate it.

One of the important consequences of the collision term is that it should bring the nonequilibrium distribution function closer to the equilibrium function. Also, it is reasonable to assume that the rate at which the nonequilibrium distribution function approaches equilibrium is proportional to the difference between them. Thus a simple expression which emulates the above properties is:

$$\text{Collision term} = K(f_{X_1}^{eq} - f_{X_1})$$

This was the basic idea used by P.L. Bhatnagar, E. P. Gross and M. Krook in their 1954 paper [71]. Thus the BGK - Boltzmann equation is

$$\frac{\partial f}{\partial t} + c_j \frac{\partial f}{\partial x_i} = \frac{f^{eq} - f}{\tau} \quad (3.1)$$

The constant τ is called the relaxation time and represents the average time between two consecutive collisions for a molecule in the system. Thus during a time dt , a fraction of dt/τ of molecules in a given small volume undergoes collision. This quantity is constant with respect to the particle velocities but can be a function of the local state of the particles and hence vary in time and space.

3.2.1 Compatibility Conditions

The BGK model should satisfy the properties (a) and (b) listed above. The compatibility conditions [70] can be expressed as:

$$\int \frac{f^{eq} - f}{\tau} \begin{pmatrix} 1 \\ \vec{c} \\ c^2 \end{pmatrix} dc = 0, \quad \text{or} \quad \int f^{eq} \begin{pmatrix} 1 \\ \vec{c} \\ c^2 \end{pmatrix} dc = \int f \begin{pmatrix} 1 \\ \vec{c} \\ c^2 \end{pmatrix} dc \quad (3.2)$$

Writing the individual components of the compatibility conditions in the second form, we can see that

$$\rho = \int f^{eq} dc = \int f dc \quad (3.3)$$

$$\rho \vec{c} = \int f^{eq} \vec{c} dc = \int f \vec{c} dc \quad (3.4)$$

$$\rho e + \rho \frac{u^2}{2} = \int f^{eq} c^2 dc = \int f c^2 dc \quad (3.5)$$

This is a consequence of the fact that internal collisions do not affect the overall density, momentum and energy of a system of N molecules. Therefore, the approximate BGK model satisfies the compatibility conditions.

3.2.2 Entropy Condition

For a system of N molecules going from nonequilibrium to equilibrium state through the internal process of collisions, the entropy should increase. Thus the BGK collision term should result in positive entropy production, which ensures that the solution obtained is

physical. An example of an unphysical solution is the presence of expansion shocks. These are typically obtained in high Mach number flows which occur in the cases we are interested in.

The original Boltzmann equations satisfy the H-theorem [72] and therefore the BGK model should also satisfy it. The H-theorem has been described as the bridge connecting equilibrium thermodynamics with non-equilibrium statistical mechanics. It states that the H-function defined by $H = \int f \ln f d\Xi$ monotonically decreases with time as a homogenous gas in statistical non-equilibrium evolves to equilibrium. A more generic form of the theorem is:

$$\frac{\partial H}{\partial t} + \frac{\partial H_i}{\partial x_i} \leq 0 \quad (3.6)$$

A detailed proof showing that the BGK collision term satisfies eq. (3.6) can be found in [73]. A simpler and more intuitive approach will be considered in this thesis.

It should be noted that the entropy is $S = -kH$, with k being the Boltzmann constant. Thus, to show that the entropy increases, one needs to show that H decreases as the system of molecules at distribution f goes towards the equilibrium. It can be written:

$$\begin{aligned} \Delta H &= \int f^{eq} \ln f^{eq} d\Xi - \int f \ln f d\Xi \\ &= \int (f^{eq} - f) \ln f^{eq} d\Xi + \int f (\ln(f^{eq} / f)) d\Xi \\ &= \int f \ln(f^{eq} / f) d\Xi \\ &\leq \int f (f^{eq} / f - 1) d\Xi \\ &= \int (f^{eq} - f) d\Xi = 0 \end{aligned}$$

Thus H decreases with time for the system considered here. It should also be noted that $f \rightarrow f^{eq}$ monotonically, implying H decreases monotonically with time. Thus the H -theorem is satisfied and this will ensure that the system will approach to a state with larger entropy. Hence the formation of unphysical rarefaction shocks is prevented.

3.3 Moments of Boltzmann BGK Equation

In this section, the moments of the Boltzmann BGK equation are evaluated. It will be later shown that these moment equations represent the Navier-Stokes equations if appropriate assumptions are made.

The first moment of the BGK equation can be written as

$$Q(c_i) = m: \quad \int_{-\infty}^{\infty} Q(c_i) \left[\frac{\partial f}{\partial t} + c_j \frac{\partial f}{\partial x_j} - \frac{f^{eq} - f}{\tau} \right] dV_c \quad (3.7)$$

The RHS will vanish as a consequence of the compatibility condition. Therefore we get

$$\begin{aligned} & \int_{-\infty}^{\infty} m \left[\frac{\partial f}{\partial t} + c_j \frac{\partial f}{\partial x_j} \right] dV_c \\ &= \int_{-\infty}^{\infty} \left[\frac{\partial mf}{\partial t} + \frac{\partial mc_j f}{\partial x_j} \right] dV_c \\ &= \left[\frac{\partial \int_{-\infty}^{\infty} m f dV_c}{\partial t} + \frac{\partial \int_{-\infty}^{\infty} m f c_j dV_c}{\partial x_j} \right] = 0 \end{aligned}$$

i.e.,

$$\frac{\partial \rho}{\partial t} + \frac{\partial(\rho \bar{c}_j)}{\partial x_j} = 0$$

The second moment can be calculated as follows:

$$\begin{aligned}
 Q(c_i) &= mc_i \\
 &= \int_{-\infty}^{\infty} mc_i \left[\frac{\partial f}{\partial t} + c_j \frac{\partial f}{\partial x_j} \right] dV_c \\
 &= \int_{-\infty}^{\infty} \left[\frac{\partial mc_i f}{\partial t} + \frac{\partial mc_i c_j f}{\partial x_j} \right] dV_c \\
 &= \left[\frac{\partial \int_{-\infty}^{\infty} mc_i f dV_c}{\partial t} + \frac{\partial \int_{-\infty}^{\infty} mfc_i c_j dV_c}{\partial x_j} \right] = 0
 \end{aligned} \tag{3.8}$$

i.e.,

$$\frac{\partial \rho \bar{c}_i}{\partial t} + \frac{\partial \int_{-\infty}^{\infty} mfc_i c_j dV_c}{\partial x_j} = 0 \tag{3.9}$$

The second term on the LHS of the last equation is an unknown quantity. However, it can be simplified in terms of known quantities as follows:

$$c_i c_j = (C_i + \bar{c}_i)(C_j + \bar{c}_j) = C_i C_j + C_i \bar{c}_j + C_j \bar{c}_i + \bar{c}_i \bar{c}_j$$

where $C_i = c_i - \bar{c}_i$ is defined as the peculiar velocity.

Therefore, we have

$$\begin{aligned}\int_{-\infty}^{\infty} mfc_i c_j dV_c &= \int_{-\infty}^{\infty} mf \left[C_i C_j + C_i \bar{c}_j + C_j \bar{c}_i + \bar{c}_i \bar{c}_j \right] dV_c \\ &= \int_{-\infty}^{\infty} mf C_i C_j dV_c + \int_{-\infty}^{\infty} mf \left[C_i \bar{c}_j + C_j \bar{c}_i \right] dV_c + \int_{-\infty}^{\infty} mf \bar{c}_i \bar{c}_j dV_c\end{aligned}$$

The second term on the RHS vanishes because of the compatibility conditions. Thus, we can write

$$\int_{-\infty}^{\infty} mfc_i c_j dV_c = \int_{-\infty}^{\infty} mf C_i C_j dV_c + \rho \bar{c}_i \bar{c}_j$$

Defining pressure as

$$p \equiv \frac{1}{3} \rho \bar{C}_i \bar{C}_i = \frac{1}{3} \rho \int_{-\infty}^{\infty} f [C_1 C_1 + C_2 C_2 + C_3 C_3] dV_c = \frac{1}{3} \rho [\bar{C}_1^2 + \bar{C}_2^2 + \bar{C}_3^2] = \frac{1}{3} \rho \bar{C}^2 \quad (3.10)$$

and the stress tensor as $\tau_{ij} = -[\rho \bar{C}_i \bar{C}_j - p \delta_{ij}]$, we can write

$$\frac{\partial \int_{-\infty}^{\infty} mfc_i c_j dV_c}{\partial x_j} = \frac{\partial p}{\partial x_j} - \frac{\partial \tau_{ij}}{\partial x_j},$$

This gives the equation

$$\frac{\partial \rho \bar{c}_i}{\partial t} + \frac{\partial \rho \bar{c}_i \bar{c}_j}{\partial x_j} = -\frac{\partial p}{\partial x_i} + \frac{\partial \tau_{ij}}{\partial x_j}$$

The third moment of the BGK equation can be obtained as follows,

$$\begin{aligned}
Q(c_i) &= mc^2/2 \\
&\int_{-\infty}^{\infty} \frac{1}{2} mc^2 \left[\frac{\partial f}{\partial t} + c_j \frac{\partial f}{\partial x_j} \right] dV_c \\
&= \frac{1}{2} \left[\frac{\partial \int_{-\infty}^{\infty} mc^2 f dV_c}{\partial t} + \frac{\partial \int_{-\infty}^{\infty} mfc^2 c_j dV_c}{\partial x_j} \right] = 0
\end{aligned}$$

Using $\rho \overline{c^2} = \rho \overline{c_i c_i} = \rho \overline{C^2} + \rho \overline{c_i^2}$ and $e = e_{tr} = \frac{1}{2} \rho \overline{C^2}$, we can write the first term of LHS as

$$\frac{1}{2} \frac{\partial \int_{-\infty}^{\infty} mnc^2 f dV_c}{\partial t} = \frac{\partial (e + \frac{1}{2} \rho \overline{c_i^2})}{\partial t} \quad (3.11)$$

In the second term, we have the quantity $\overline{c^2 c_j}$. This term can be expressed as

$$\begin{aligned}
\overline{c^2 c_j} &= \overline{c_i c_i c_j} = \overline{(\overline{c_i} + C_i)(\overline{c_i} + C_i)(\overline{c_j} + C_j)} \\
&= \overline{(\overline{c}^2 + C^2 + 2\overline{c_i}C_i)(\overline{c_j} + C_j)} \\
&= \overline{c}^2 \overline{c_j} + \overline{c_j} \overline{C^2} + 2\overline{c_i} \overline{c_j} \overline{C_i} + \overline{c}^2 \overline{C_j} + \overline{C^2 C_j} + 2\overline{c_i} \overline{C_i C_j} \\
&= \overline{c_j} (\overline{c}^2 + \overline{C^2}) + \overline{C^2 C_j} + 2\overline{c_i} \overline{C_i C_j}
\end{aligned}$$

The highlighted terms vanish because of the properties of random variables C_i .

Therefore, we can write

$$\begin{aligned}\frac{1}{2}\rho\overline{c^2}c_j &= \bar{c}_j\left(\frac{1}{2}\rho\bar{c}^2 + \frac{1}{2}\rho\overline{C^2}\right) + \frac{1}{2}\rho\overline{C^2C_j} + \rho\bar{c}_i\overline{C_iC_j} \\ &= \bar{c}_j\left(\frac{1}{2}\rho\bar{c}^2 + \frac{1}{2}\rho\overline{C^2}\right) + \frac{1}{2}\rho\overline{C^2C_j} + \bar{c}_i(p\delta_{ij} - \tau_{ij})\end{aligned}$$

$$\begin{aligned}\frac{\partial \int_{-\infty}^{\infty} mnfc^2 c_j dV_c}{\partial x_j} &= \frac{\partial \left[\bar{c}_j \left(\frac{1}{2}\rho\bar{c}^2 + \frac{1}{2}\rho\overline{C^2} \right) + \frac{1}{2}\rho\overline{C^2C_j} + \bar{c}_i(p\delta_{ij} - \tau_{ij}) \right]}{\partial x_j} \\ \text{i.e.,} \quad &= \frac{\partial \left[\bar{c}_j (\rho e + \frac{1}{2}\rho\bar{c}^2) \right]}{\partial x_j} + \frac{\partial \left[\frac{1}{2}\rho\overline{C^2C_j} \right]}{\partial x_j} + \frac{\partial [\bar{c}_j p]}{\partial x_j} - \frac{\partial [\bar{c}_i \tau_{ij}]}{\partial x_j} \quad (3.12)\end{aligned}$$

Defining $q_j = \frac{1}{2}\rho \left[\int_{-\infty}^{\infty} C_j C^2 f dV_c \right]$, we can write the second moment of the BGK equation in the final form as

$$\frac{\partial \left[(\rho e + \frac{1}{2}\rho\bar{c}^2) \right]}{\partial t} + \frac{\partial \left[\bar{c}_j (\rho e + \frac{1}{2}\rho\bar{c}^2) \right]}{\partial x_j} = -\frac{\partial q_j}{\partial x_j} - \frac{\partial [\bar{c}_j p]}{\partial x_j} + \frac{\partial [\bar{c}_i \tau_{ij}]}{\partial x_j} \quad (3.13)$$

3.4 Deriving Navier Stokes Equations

In the above three relations, the unknowns are p, τ_{ij} and q_j . From the above relations we find that pressure is related to energy as

$$p = 2e_{tr}/3 = \rho RT \quad (3.14)$$

Therefore, how accurately the equations obtained represent the true physics will

depend on the choice of τ_{ij} and q_j . In the case of Navier-Stokes equations, these unknowns are expressed as linear functions of the velocity and temperature gradients. The value of the corresponding constants is determined experimentally. However, such a linear relationship only holds for low Knudsen number or continuum cases where the higher order terms can be neglected. Therefore to simulate high Knudsen number flows we need to take into account higher order terms.

To show that the BGK moment equations actually recover the Navier Stoke equations in low Knudsen number regions, the Chapman-Enskog expansion of the BGK equation needs to be considered. Before starting the calculations, we first normalize the BGK equation using the following scaling parameters:

$$\text{Characteristic length:} \quad L$$

$$\text{Reference speed:} \quad c_r$$

$$\text{Characteristic time:} \quad 1/c_r$$

$$\text{Reference number density:} \quad n_r$$

$$\text{Reference } f: \quad c_r^{-3}$$

$$\text{Reference } v: \quad v_r$$

The scaled equation can be written as

$$\xi \left[\frac{\partial \tilde{f}}{\partial \tilde{t}} + \tilde{c}_j \frac{\partial \tilde{f}}{\partial \tilde{x}_j} \right] = \tilde{n} \tilde{v} (\tilde{f}^0 - \tilde{f}) \quad (3.15)$$

$$\text{where } \xi = \frac{c_r}{L v_r}, \tilde{f} = f c_r^3, \tilde{t} = \frac{t c_r}{L}, \tilde{x} = \frac{x}{L}, \tilde{c} = \frac{c}{c_r}, \tilde{v} = \frac{v}{v_r}$$

It can be shown that $\xi \sim$ Knudsen number ($\frac{\lambda_r}{L}$). Since we are working in the continuum regime for this derivation, we have $\xi \ll 1$. Then from the above equation we can see that \tilde{f}^0 is very close to \tilde{f} . This allows us to expand the distribution function around the equilibrium distribution as:

$$\begin{aligned}\tilde{f} &= \tilde{f}_0 + \xi \phi_1 \tilde{f}_0 + \xi^2 \phi_2 \tilde{f}_0 + \dots \\ &= \tilde{f}_0 (1 + \xi \phi_1 + \xi^2 \phi_2 + \dots)\end{aligned}$$

Here ϕ_1, ϕ_2, \dots are unknown quantities which are to be determined in terms of mean flow quantities.

Substituting this expansion in the normalized Boltzmann equation and by comparing the coefficients of ξ we get

$$\left[\frac{\partial \tilde{n} \tilde{f}_0}{\partial \tilde{t}} + \tilde{c}_j \frac{\partial \tilde{n} \tilde{f}_0}{\partial \tilde{x}_j} \right] = -\tilde{n} \tilde{v} \phi_1 \tilde{f}^0 \quad (3.16)$$

The normalized equilibrium distribution function being a Maxwellian can be expressed as

$$\begin{aligned}
\tilde{f}_0 &= \left(\frac{1}{2\pi\tilde{T}}\right)^{3/2} \exp\left[-\frac{1}{2\tilde{T}}(\tilde{c}_i - \tilde{\bar{c}}_i)^2\right] \\
&= \text{function}(\tilde{T}, \tilde{\bar{c}}_i, \tilde{c}_i) \\
\text{where } \tilde{T} &= \tilde{T}(\tilde{x}, t), \quad \tilde{\bar{c}}_i = \tilde{\bar{c}}_i(x, t)
\end{aligned} \tag{3.17}$$

Therefore, we can calculate the terms in the LHS of the above equation using the following relations:

$$\begin{aligned}
\frac{\partial \tilde{n}\tilde{f}_0}{\partial \tilde{t}} &= \frac{\partial \tilde{n}\tilde{f}_0}{\partial \tilde{n}} \frac{\partial \tilde{n}}{\partial \tilde{t}} + \frac{\partial \tilde{n}\tilde{f}_0}{\partial \tilde{\bar{c}}_j} \frac{\partial \tilde{\bar{c}}_j}{\partial \tilde{t}} + \frac{\partial \tilde{n}\tilde{f}_0}{\partial \tilde{T}} \frac{\partial \tilde{T}}{\partial \tilde{t}} \\
\frac{\partial \tilde{n}\tilde{f}_0}{\partial \tilde{x}_i} &= \frac{\partial \tilde{n}\tilde{f}_0}{\partial \tilde{n}} \frac{\partial \tilde{n}}{\partial \tilde{x}_i} + \frac{\partial \tilde{n}\tilde{f}_0}{\partial \tilde{\bar{c}}_j} \frac{\partial \tilde{\bar{c}}_j}{\partial \tilde{x}_i} + \frac{\partial \tilde{n}\tilde{f}_0}{\partial \tilde{T}} \frac{\partial \tilde{T}}{\partial \tilde{x}_i}
\end{aligned} \tag{3.18}$$

where

$$\begin{aligned}
\frac{\partial}{\partial \tilde{c}_i} (\tilde{n}\tilde{f}_0) &= -\tilde{n}\tilde{f}_0 \frac{\tilde{C}_i}{\tilde{T}}, \quad \frac{\partial}{\partial \tilde{n}} (\tilde{n}\tilde{f}_0) = \tilde{f}_0 \\
\frac{\partial}{\partial \tilde{\bar{c}}_i} (\tilde{n}\tilde{f}_0) &= \tilde{n}\tilde{f}_0 \frac{\tilde{C}_i}{\tilde{T}}, \quad \frac{\partial}{\partial \tilde{T}} (\tilde{n}\tilde{f}_0) = \tilde{n}\tilde{f}_0 \left[\frac{\tilde{C}^2}{2\tilde{T}^2} - \frac{3}{2\tilde{T}} \right]
\end{aligned} \tag{3.19}$$

The time derivatives $\frac{\partial \tilde{n}}{\partial \tilde{t}}$, $\frac{\partial \tilde{\bar{c}}_j}{\partial \tilde{t}}$ and $\frac{\partial \tilde{T}}{\partial \tilde{t}}$ can be found by making use of the continuity, momentum and energy equations:

$$\text{Continuity Equation: } \frac{\partial \rho}{\partial t} + \frac{\partial(\rho \bar{c}_j)}{\partial x_j} = 0 \Rightarrow \frac{\partial \tilde{n}}{\partial \tilde{t}} = -\frac{\partial(\tilde{n}\tilde{\bar{c}}_j)}{\partial \tilde{x}_j} \tag{3.20}$$

Momentum Equation:

$$\frac{\partial \rho \bar{c}_i}{\partial t} + \frac{\partial \rho \bar{c}_i \bar{c}_j}{\partial x_j} = -\frac{\partial p}{\partial x_i} + \frac{\partial \tau_{ij}}{\partial x_j} \Rightarrow \tilde{n} \frac{\partial \tilde{c}_i}{\partial \tilde{t}} = -\tilde{n} \tilde{c}_j \frac{\partial \tilde{c}_i}{\partial \tilde{x}_j} - \frac{\partial \tilde{p}}{\partial \tilde{x}_i} + \frac{\partial \tilde{\tau}_{ij}}{\partial \tilde{x}_j} \quad (3.21)$$

Energy Equation:

$$\begin{aligned} \frac{\partial \left[(\rho e + \frac{1}{2} \rho \bar{c}^2) \right]}{\partial t} + \frac{\partial \left[\bar{c}_j (\rho e + \frac{1}{2} \rho \bar{c}^2) \right]}{\partial x_j} &= -\frac{\partial \left[\frac{1}{2} \rho \bar{C}^2 C_j \right]}{\partial x_j} - \frac{\partial [\bar{c}_j p]}{\partial x_j} + \frac{\partial [\bar{c}_i \tau_{ij}]}{\partial x_j} \\ \Rightarrow \tilde{n} \frac{3}{2} \frac{\partial \tilde{T}}{\partial \tilde{t}} &= -\tilde{c}_j \tilde{n} \frac{3}{2} \frac{\partial \tilde{T}}{\partial \tilde{x}_j} - \frac{\partial \tilde{q}_j}{\partial \tilde{x}_j} - \tilde{p} \frac{\partial \tilde{c}_j}{\partial \tilde{x}_j} + \tilde{\tau}_{ij} \frac{\partial \tilde{c}_i}{\partial \tilde{x}_j} \end{aligned} \quad (3.22)$$

The expressions for normalized stress tensor and heat flux can be obtained as follows

$$\begin{aligned} \tilde{\tau}_{ij} &= - \left[\int_{-\infty}^{\infty} \tilde{n} \tilde{C}_i \tilde{C}_j (1 + \xi \phi_1) \tilde{f}_0 d\tilde{V}_c - \tilde{p} \delta_{ij} \right] \\ &= -\xi \tilde{n} \int_{-\infty}^{\infty} \tilde{C}_i \tilde{C}_j \phi_1 \tilde{f}_0 d\tilde{V} \end{aligned} \quad (3.23)$$

$$\begin{aligned} \tilde{q}_j &= \frac{1}{2} \tilde{n} \left[\int_{-\infty}^{\infty} \tilde{C}_i \tilde{C}^2 (1 + \xi \phi_1) \tilde{f}_0 d\tilde{V}_c \right] \\ &= \xi \tilde{n} \left[\int_{-\infty}^{\infty} \frac{1}{2} \tilde{C}_i \tilde{C}^2 \xi \phi_1 \tilde{f}_0 d\tilde{V}_c \right] \end{aligned} \quad (3.24)$$

Since we are interested in finding the coefficients of ξ in (3.15), we can neglect $\tilde{\tau}_{ij}$ and \tilde{q}_j from (3.21) and (3.22), since these are first order in ξ . Therefore the time derivative terms can be written as

$$\begin{aligned}
\frac{\partial \tilde{n}}{\partial \tilde{t}} &= -\frac{\partial(\tilde{n}\tilde{c}_j)}{\partial \tilde{x}_j} \\
\tilde{n} \frac{\partial \tilde{c}_i}{\partial \tilde{t}} &\approx -\tilde{n}\tilde{c}_j \frac{\partial \tilde{c}_i}{\partial \tilde{x}_j} - \frac{\partial \tilde{p}}{\partial \tilde{x}_i} \\
\tilde{n} \frac{3}{2} \frac{\partial \tilde{T}}{\partial \tilde{t}} &\approx -\tilde{c}_j \tilde{n} \frac{3}{2} \frac{\partial \tilde{T}}{\partial \tilde{x}_j} - \tilde{p} \frac{\partial \tilde{c}_j}{\partial \tilde{x}_j}
\end{aligned} \tag{3.25}$$

Making the substitutions of the above derivates in (3.16), we can derive ϕ_1 as

$$\phi_1 = -\frac{1}{\tilde{n}\tilde{v}\tilde{f}^0} \left[\frac{\partial \tilde{n}\tilde{f}_0}{\partial \tilde{n}} \left[\tilde{n} \frac{\partial \tilde{c}_i}{\partial \tilde{x}_i} + \tilde{C}_i \frac{\partial \tilde{n}}{\partial \tilde{x}_i} \right] + \frac{1}{\tilde{n}} \frac{\partial \tilde{n}\tilde{f}_0}{\partial \tilde{c}_j} \left[\frac{\partial \tilde{p}}{\partial \tilde{x}_j} + \tilde{n}\tilde{C}_i \frac{\partial \tilde{c}_j}{\partial \tilde{x}_i} \right] + \frac{1}{\tilde{n}} \frac{\partial \tilde{n}\tilde{f}_0}{\partial \tilde{T}} \left[-\frac{2}{3} \tilde{p} \frac{\partial \tilde{c}_j}{\partial \tilde{x}_j} + \tilde{n}\tilde{C}_i \frac{\partial \tilde{T}}{\partial \tilde{x}_i} \right] \right] \tag{3.26}$$

The normalized pressure can be obtained from the normalized equation of state:

$$p = \rho RT = nm \frac{k}{m} T = nkT \Rightarrow \tilde{p} = \tilde{n}\tilde{T}$$

Substituting the above in (3.26), we get

$$\phi_1 = -\frac{1}{\tilde{n}\tilde{v}} \left[\left[\frac{\tilde{C}^2}{2\tilde{T}} - \frac{5}{2} \right] \cdot \tilde{n} \frac{\tilde{C}_i}{\tilde{T}} \frac{\partial \tilde{T}}{\partial \tilde{x}_i} + \tilde{n} \frac{\tilde{C}_i \tilde{C}_j}{\tilde{T}} \frac{\partial \tilde{c}_j}{\partial \tilde{x}_i} - \tilde{n} \frac{\tilde{C}^2}{3\tilde{T}} \frac{\partial \tilde{c}_j}{\partial \tilde{x}_j} \right] \tag{3.27}$$

The expression can be written in dimensional form to give:

$$\xi\phi_1 = -\frac{1}{v} \left[C_j \left[\frac{mC^2}{2kT} - \frac{5}{2} \right] \cdot \frac{\partial \ln(T)}{\partial x_i} + \frac{m}{kT} (C_i C_j - \frac{1}{3} C^2 \delta_{ij}) \frac{\partial \bar{c}_i}{\partial x_j} \right] \quad (3.28)$$

Substituting the above value in expressions for $\tilde{\tau}_{ij}$ and q_j , we get

$$\begin{aligned} \tau_{ij} &= - \left[\int_{-\infty}^{\infty} \rho C_i C_j (1 + \xi\phi_1) f_0 dV_c - p \delta_{ij} \right] \\ &= -\rho \int_{-\infty}^{\infty} C_i C_j \xi\phi_1 f_0 dV \\ &= \frac{nkT}{v} \left[\frac{\partial \bar{c}_i}{\partial x_j} + \frac{\partial \bar{c}_j}{\partial x_i} - \frac{2}{3} \frac{\partial \bar{c}_k}{\partial x_k} \delta_{ij} \right] \end{aligned} \quad (3.29)$$

$$\begin{aligned} q_j &= \frac{1}{2} \rho \left[\int_{-\infty}^{\infty} C_j C^2 (1 + \xi\phi_1) f_0 dV_c \right] \\ &= \xi\rho \left[\int_{-\infty}^{\infty} \frac{1}{2} C_j C^2 \xi\phi_1 f_0 dV_c \right] \\ &= -\frac{5}{2} \frac{k}{m} \frac{nkT}{v} \frac{\partial T}{\partial x_j} \end{aligned} \quad (3.30)$$

Therefore by comparison with the expressions for stress tensor and heat flux in Navier Stokes equation, we can write

$$\begin{aligned} \mu &= \frac{nkT}{v} \\ K &= \frac{5}{2} \frac{k}{m} \frac{nkT}{v} \end{aligned} \quad (3.31)$$

Thus, the BGK Boltzmann moment equations represent the Navier Stokes equation in low Knudsen number or continuum regime, if (3.31) holds true.

CHAPTER IV

HIGH TEMPERATURE FLOWS: MATHEMATICAL FORMULATIONS AND MODELS

4.1 Variables and Their Dependencies

The various laws governing a high enthalpy flow and their interrelations are shown in the figure 4.1. The various blocks can be explained as follows:

4.1.1 Conservation of Mass

At very high temperatures dissociation and chemical reactions between air components set in. Thus conservation of mass equation needs to be written for each of the species and will have a contribution from the kinetics of reactions. The total density needs to be calculated by adding the individual densities. The total density is used in calculation of pressure in the equation of state.

4.1.2 Conservation of Momentum

Throughout this work, it is assumed that momentum conservation equation can be adequately represented by the Navier Stokes equation. The high temperature flow physics affects the momentum equation via pressure and body force effects. Due to the high enthalpy of the flow, the viscosity coefficient is no longer constant and becomes a function of temperature.

4.1.3 Conservation of Energy

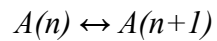
The total energy is conserved even as there is an active exchange between various modes:: translational-rotational, vibrational and chemical. The translational, rotational

energies are obtained using the temperature, while the chemical energy is dependent on the free energies of each of the species. However, we need to model the excited vibrational energy mode, which is done by writing an evolution equation for it. This will be discussed in the next section.

It is shown in figure 4.1 that all the three conservation laws are coupled through two parameters: pressure and temperature. Comparing to compressible flows, nonequilibrium flows have even more couplings due to temperature dependence of various transport and chemical rate coefficients. The presence of numerous species and the enhanced couplings due to temperature is what makes solving nonequilibrium flows expensive.

4.2 Physics of Vibrational Nonequilibrium

Vibrational excitation and relaxation processes take place by molecular collisions and radiative interactions. A molecule in ground state must experience a large number of collisions to become vibrationally excited. Such a process is represented as



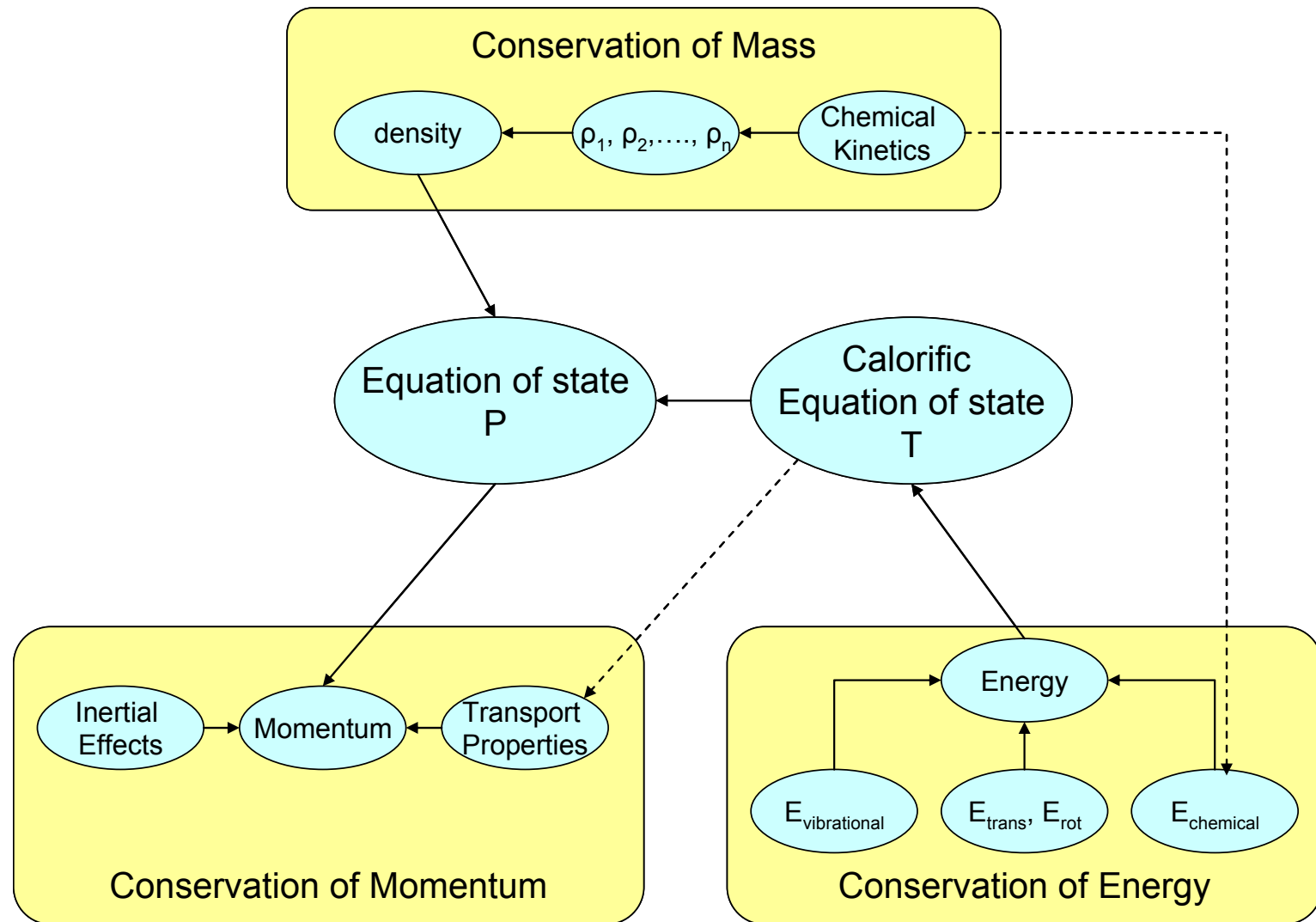


Fig 4.1 Various processes and their interrelations for the case of hypersonic flows

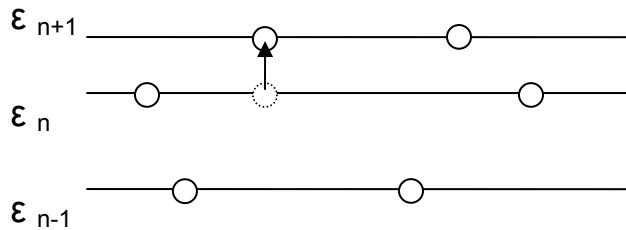


Fig 4.2 Vibrational excitation of molecule A through single quantum transition

Figure 4.2 shows that a molecule in n^{th} vibrational state goes to $(n+1)^{th}$ vibrational state (due to either collision or radiative process). The actual number of collisions required depends on factors such as type of molecule and relative kinetic energies of colliding particles. As the temperature of the gas is increased the molecular collisions become more violent and the molecule undergoes vibrational and chemical changes. The amount of time taken for these changes depends on the collision frequency Z , where

$$Z = p / \sqrt{T}$$

p is the pressure and T is the temperature. Therefore to study the nonequilibrium region, additional techniques need to be developed that take into account the time required for molecular collisions.

4.3 Harmonic and Anharmonic Oscillators

A molecule is modeled as a harmonic oscillator if the spacings between all the energy levels are assumed to be equal. Physically, such vibrations can be represented as the motion of two masses attached to a spring, which can only take equally spaced potential energy values. Such a representation is shown in figure 4.3.

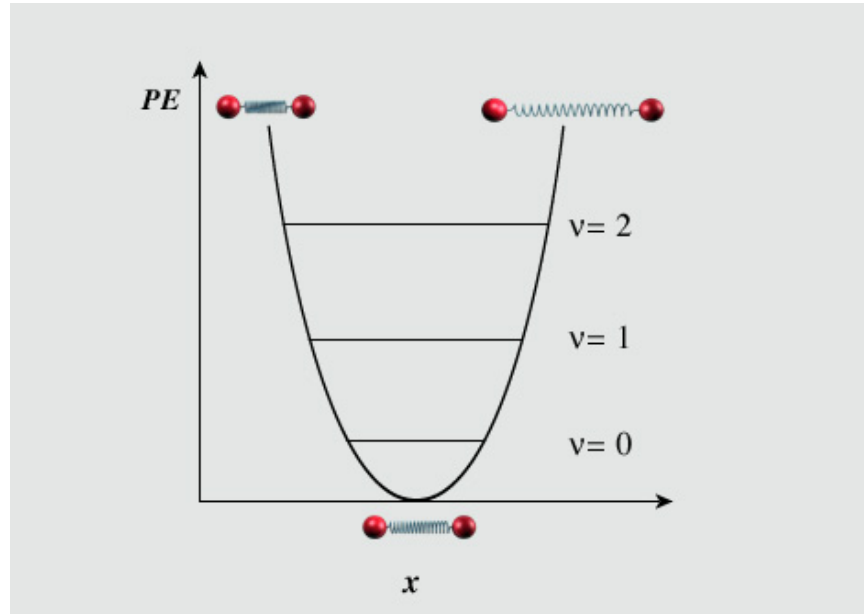


Fig 4.3 Vibrational energy levels for Harmonic Oscillator [87]

The energy levels for such harmonic oscillator are given as

$$E_n = (n + 1/2)\hbar\nu, \quad n = 0, 1, 2, 3, \dots$$

ν =frequency,
 \hbar =Planck's Constant

(4.1)

This model is the foundation for the understanding of complex modes of vibration in larger molecules, the motion of atoms in a solid lattice, the theory of heat capacity, etc. However it should be noted that in real systems, although the molecules behave as harmonic oscillator for lower energy levels, they deviate from such behavior at higher quantum number.

Thus to more accurately predict such exchanges at higher energy levels, anharmonic

oscillator model is used. As it can be seen in figure 4.4 the energy levels are no longer equispaced and become more closely packed for higher energy levels.

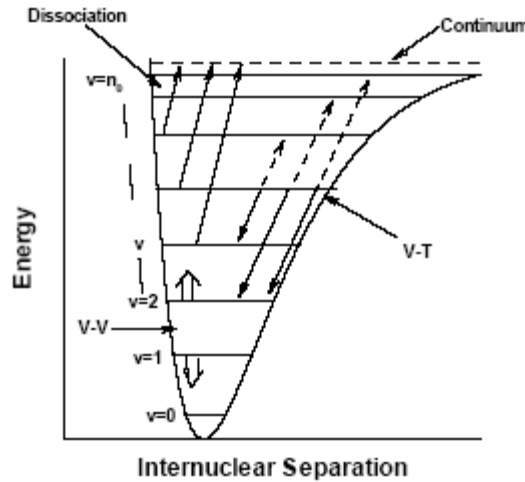


Fig 4.4 Vibrational energy levels for Anharmonic Oscillator [7]

The energy of such a system is found by one of the models which gives an expression of energy for the v^{th} vibrational (third order approximating formula), and is given as

$$\frac{\varepsilon_i}{hc} = \omega_e(i - 1/2) - \omega_e x_e (i - 1/2)^2 + \omega_e y_e (i - 1/2)^3 \quad i = 1, 2, \dots \quad (4.2)$$

This formula is discussed in greater details in section 4.6.1.

4.4 Vibrational Energy Transfer Modes

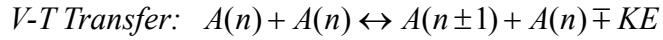
If the flow is assumed to be in electronic and rotational equilibrium, then vibrational

energy exchange is found to occur through three modes:

4.4.1 Vibrational Translational Energy Transfer

Here, a molecule upon collision with another will gain or lose vibrational energy which then reappears as a decrease or increase in translational kinetic energy of the molecules.

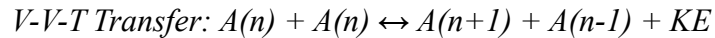
This process is represented as



Such a mechanism holds for both harmonic as well as anharmonic oscillators.

4.4.2 Vibrational-Vibrational-Translational Transfer

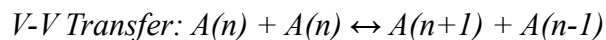
In this case, a molecule loses a vibrational quantum. A part of this energy is gained by another molecule to achieve higher vibrational state and rest is released and translational kinetic energy.



Such a mechanism only holds for anharmonic oscillators.

4.4.3 Vibrational-Vibrational Transfer

In previous case, unequal spacing between the vibrational energy levels cause some energy to be released as translational energy. However, if the energy levels are assumed to be equally spaced, the energy is contained on the vibrational mode and constitutes the vibrational-vibrational transfer.



This kind of mechanism can only occur for harmonic oscillators.

4.5 Vibrational Population Distribution

The population distribution for a diatomic species for the different vibrational energy levels varies from case to case. Broadly two different types of population distribution are found: for cooling relaxation cases or expanding flows, and for post shock flows.

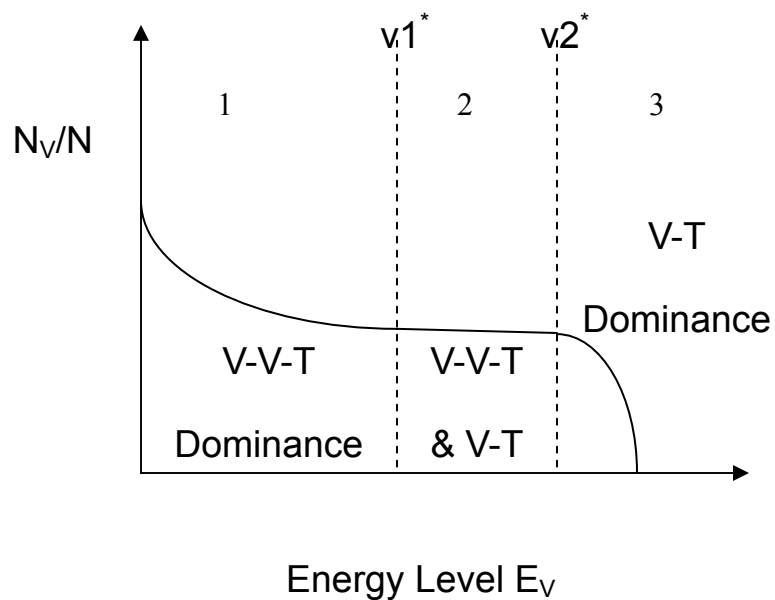


Fig 4.5 Nonequilibrium vibrational population distribution (expanding flows)

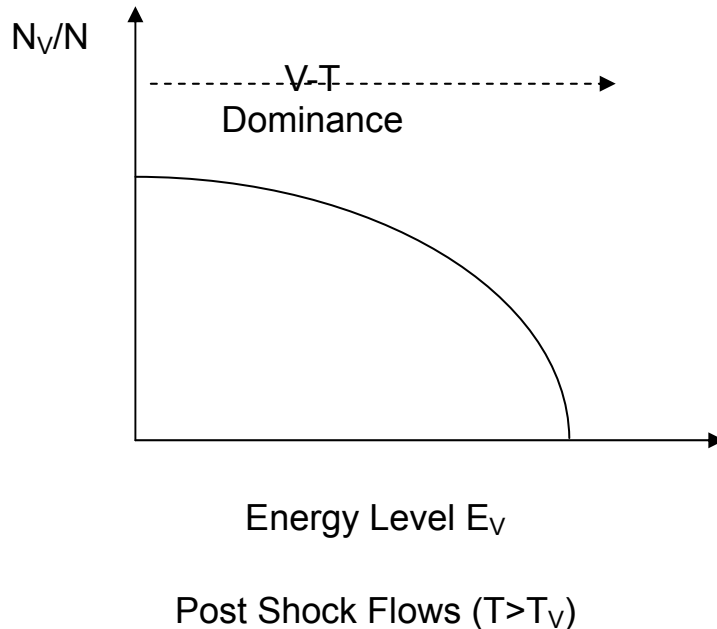


Fig 4.6 Nonequilibrium vibrational population distribution (post shock flows)

For expanding flows the distribution consists of the three regions as shown in the figure 4.5. Region 1 corresponds to the low vibrational levels in which V-V-T exchange rates are much greater than the V-T rates. The near resonant V-V-T exchanges pump vibrational quanta upward toward regions 2 and 3.

In region 2 the V-T transition rates also become important because the equilibrium rates are of the same magnitude or greater than the V-V-T exchange rates. In this region the V-V-T exchange rates still influence the distribution by tending to pump vibrational quanta upward. However the V-T rates then act to transfer the energy to translation. The V-T rates which increase with quantum number limit the overpopulation caused by the V-V-T exchange rates. This region is characterized by a nearly constant slope of the number densities. This region is often responsible for much of the acceleration in relaxation rates in expansion because the anharmonic V-T rates can be much greater than

those assumed by Landau Teller model.

In region 3, the V-T rates become much greater than the V-V exchange rates as well as the V-T rates at lower levels. Unlike region 2, vibrational quanta are not being pumped into this region and are only being lost to translation mode through V-T transfer. Thus region 3 reaches equilibrium much faster than the remainder of the vibrational levels. Hence the distribution in this region corresponds to the Boltzmann distribution at local translational temperature.

For the case of post shock flows, figure 4.6 shows that the V-T rates dominate the V-V-T transition rates for all levels. The distribution is similar to the distribution of region 3 for expanding flows.

4.6 Modeling Vibrational Energy Evolution

To write the vibrational rate equation, we need to write the net rate of change of population of i^{th} level. This can be written as

$$\frac{d\rho_i}{dt} = \sum_{j \neq i} k_{j,i} \rho_j - \sum_{j \neq i} k_{i,j} \rho_i, \quad (4.3)$$

where ρ_m represents the number of molecules in m^{th} vibrational level, and $k_{m,n}$ represents the vibrational rate constant for transition from m^{th} energy level to n^{th} energy level. This equation is called the master equation for vibrational relaxation. The first term on the RHS represents the number of molecules jumping to i^{th} level from all other energy levels, while the second term represents the number of molecules leaving the i^{th} level.

Corresponding equation for the rate of change of total energy of molecules in i^{th} level can be written as

$$\frac{de_{v,i}}{dt} = \sum_{j \neq i} k_{j,i} \rho_j \epsilon_j - \sum_{j \neq i} k_{i,j} \rho_i \epsilon_i . \quad (4.4)$$

Based on this equation, we can write vibrational rate equation for the total vibrational energy e_v as

$$\frac{de_v}{dt} = \sum_i \frac{de_{v,i}}{dt} = \sum_i \sum_{j \neq i} k_{j,i} \rho_j \epsilon_j - \sum_i \sum_{j \neq i} k_{i,j} \rho_i \epsilon_i , \quad (4.5)$$

where ϵ_n represents the energy of n^{th} vibrational level, and ρ_n represents the density of n^{th} vibrational level.

Further modeling of terms appearing in the above equation to obtain complete expression of the vibration rate equation is required. The three important approaches in this context are discussed below.

4.6.1 Multiquantum Transition Approach

In this approach we model the molecule as an Anharmonic oscillator. The vibrational energy for i^{th} level is represented using a result from quantum mechanics known as the third order approximating formula, as shown in [7] and [8],

$$\frac{\epsilon_i}{hc} = \omega_e(i - 1/2) - \omega_e x_e (i - 1/2)^2 + \omega_e y_e (i - 1/2)^3 \quad i = 1, 2, \dots \quad (4.6)$$

Here, h is the Planck's constant; c is the speed of light; and ω_e , $\omega_e x_e$ and $\omega_e y_e$ are the spectroscopic constants.

Therefore, in this case there is no need of a separate vibrational rate equation as the vibrational energy at any moment can be found by adding the energies of individual vibrational levels. Thus,

$$e_{vib}(t) = \sum_{v=0}^* \frac{\rho_v(t)}{\rho(t)} \epsilon_v, \quad (4.7)$$

where ρ_v is found using the master equation

$$\frac{d\rho_i}{dt} = \sum_{j \neq i} k_{j,i} \rho_j - \sum_{j \neq i} k_{i,j} \rho_i. \quad (4.8)$$

A common approach is to assume only single quantum transitions, used in [9], for which the above expression becomes

$$\frac{d\rho_i}{dt} = k_{i+1,i} \rho_j - k_{i,i+1} \rho_i + k_{i-1,i} \rho_j - k_{i,i-1} \rho_i \quad (4.9)$$

One of the problems faced is the accurate prediction for the transfer rates k_{ij} . There are three major approaches in literature [10] upon which the models for the transfer rates are based on:

- (i) Fully quantum calculations
- (ii) Classical, quasiclassical and semiclassical numerical trajectory calculations
- (iii) Analytic methods

While models based on (i) are extremely computationally expensive and those based on (ii) are applicable to very limited cases, most commonly used models are based on (iii) analytical approach. Most of these analytical models such as the Schwartz, Slawsky, Herzfeld (SSH) theory, Rapp–Englander–Golden model, Sharma–Brau theory etc.[11]-[14] are based on first-order perturbation theory (FOPT), and therefore, cannot be applied at high collision energies, high-quantum numbers, and for multiquantum

processes. However, an exception is the nonperturbative forced harmonic oscillator (FHO) model [15]–[18] which takes into account the coupling of many vibrational states during collisions and is, therefore, applicable for such conditions.

The Multi Quantum or master equation model is the most accurate models available to simulate the vibrational energy transfer rate. However, computational requirements for such a model make it unpractical for fairly complicated problems. Joysula et al. [7] solved the master equations assuming double quantum transitions only. It was found that the results had only a minor deviation from the single quantum transition results. Thus in most of the works based on anharmonic oscillator models, the single quantum transition assumption has been made which has given results in good agreement with experimental results. However, even the single quantum transition models turn out to be very expensive and make them unsuitable for use for complex geometries.

4.6.2 Landau- Teller Approach

To reduce the complexities and the number of equations involved in the multi quantum transition approach, simplifying assumptions are made to get an easy to use and inexpensive model. An outline of the important steps in the derivation of this model along with the implications of the assumptions made, are shown in figure 4.7:

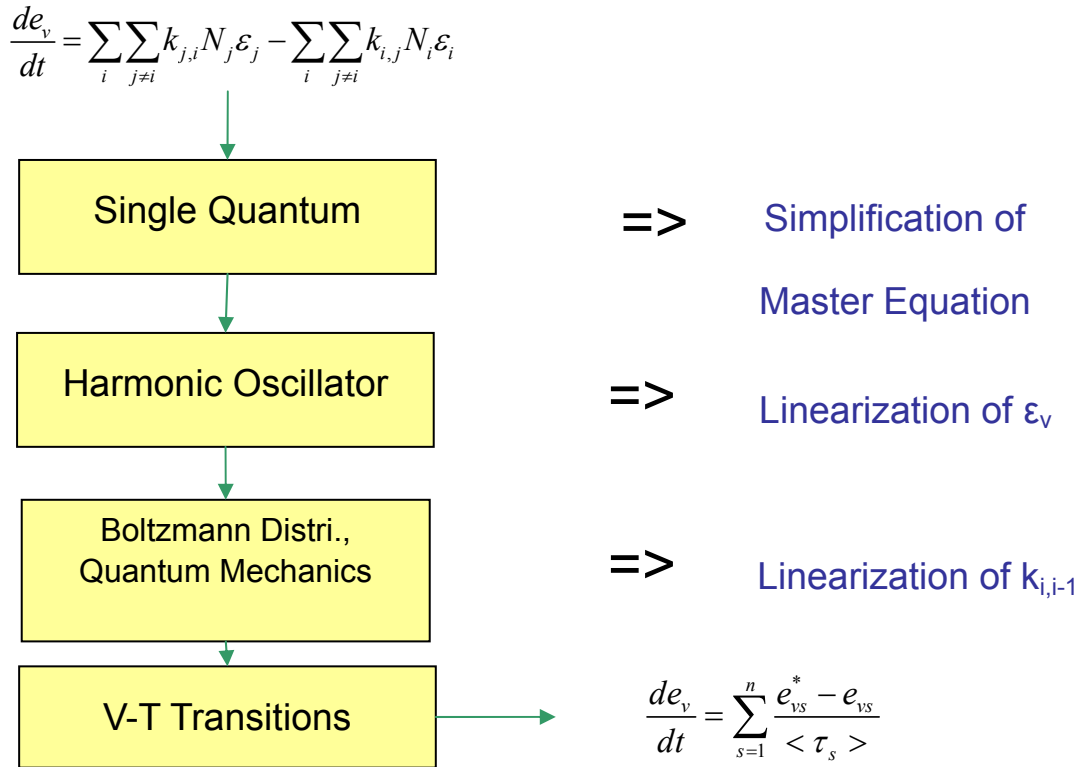


Fig 4.7 Overview of derivation for Landau Teller model

Thus we get the final expression as

$$\frac{de_v}{dt} = \sum_{s=1}^n \frac{e_{vs}^* - e_{vs}}{\langle \tau_s \rangle} \quad (4.10)$$

where e_{vs}^* is the value of e_v at equilibrium and is given as

$$e_{v,s}^{eq} = \frac{h\nu_s / kT}{e^{h\nu_s / kT} - 1} RT \quad (4.11)$$

and τ_s is the vibrational relaxation time. Physically the expression for vibrational rate can be understood as follows: suppose we instantaneously excite the vibrational mode above its equilibrium value, i.e. for $t = 0$

$$e_{vib_0} > e_{vib}^{eq}$$

Due to molecular collisions, the excited particles will exchange this excessive vibrational energy with the translational and rotational energies of the gas and after a period of time e_{vib} will decrease and approach its equilibrium value. However, as the vibrational energy decreases, it reappears in the form of translational energy and thus T increases. And thus the equilibrium value of vibrational energy will also increase. Thus at large times e_{vib} and e_{vib}^{eq} will approach the same value asymptotically.

As discussed in previous section, vibrational nonequilibrium occurs due to the presence of very high temperatures in the flow. For example in the case of shock wave in hypersonic flows, as p and T are suddenly changed, the equilibrium vibrational and chemical properties will change. The fluid element will start to seek these new equilibrium properties which require collisions between molecules and hence time. However by this time, the flow has covered a certain distance behind the shock and hence we get a region of vibrational nonequilibrium.

The relaxation time τ is a function of both local pressure and temperature. One of the most commonly used model for τ is the Millikan and White [19] formula. The following assumptions are made:

- (i) The system consists of diatomic oscillators only
- (ii) Only one type of collision is allowed (V-T transitions)

(iii) Vibration-vibration energy transfer is not important

However, this approach can be used for some special complicated cases also. Using experimental data and curve fitting, the expression obtained is

$$p\tau_{vs} = \exp[A_s(T^{-\frac{1}{3}} - 0.015\mu_s^{\frac{1}{4}}) - 18.42],$$

where τ_{vs} is the relaxation time for species 's'; p is the pressure; and A_s and μ_s are the constants specific to the species. The constant A_s has the expression

$$A_s \propto \mu^{\frac{1}{3}}\theta^{\frac{2}{3}},$$

where μ is the reduced mass of the colliding pair, and θ is the characteristic temperature of the oscillator. Values for some common species are given in [19]. This model has been found to be accurate for the following ranges of the above parameters:

$$1.75 < \mu < 127; 310^0 < \theta < 3395^0 K; 280^0 < T < 8000^0 K$$

For a mixture of species, the molar averaged Landau - Teller relaxation time is defined as

$$\frac{1}{\tau_v} = \sum_s X_s \frac{1}{\tau_{vs}}$$

where X_s is the molar fraction of species 's'. Landau Teller model is computationally

much easier to implement compared to the other models. It also happens to be computationally inexpensive. However, some issues of accuracy exist due to the simplifying assumptions made.

As seen earlier, V-V-T transfers gain importance for lower energy levels in the case of expanding flows while V-T transfers dominate for all energy levels for compressing flows. Since this model only assumes only V-T transfers, it has been found to give accurate results for post shock flows. However, for expanding flows, the V-V-T transfers result in an increase in population of mid and upper quantum levels. An over population of these states implies higher V-T rates, since V-T transfers dominate the upper energy levels. Landau-Teller model fails to capture this phenomenon as it neglects the V-V-T transfers and hence predicts slower V-T rates.

The vibrational population distribution was assumed to follow Boltzmann distribution for all the levels for the derivation of this model. However, the Boltzmann distribution exist only for lower quantum levels and thus the transition rate constants $k_{i,i-1}$ become non-linear for higher levels. This results in a further deviation between the real and predicted values of V-T transfer rate, Landau Teller model predicting the smaller rates. These limitations of Landau Teller model were studied and discussed in [58] by comparison of computational results with experimental data.

4.6.3 Ruffin's Model

Ruffin developed a simplified relaxation model with an objective to improve the accuracy of Landau Teller model by increasing its range of applicability, while at the same time ensuring it is not as expensive as master equation model. An outline of the important steps in the derivation of this model along with the implications of the assumptions made, are shown in figure 4.8 below:

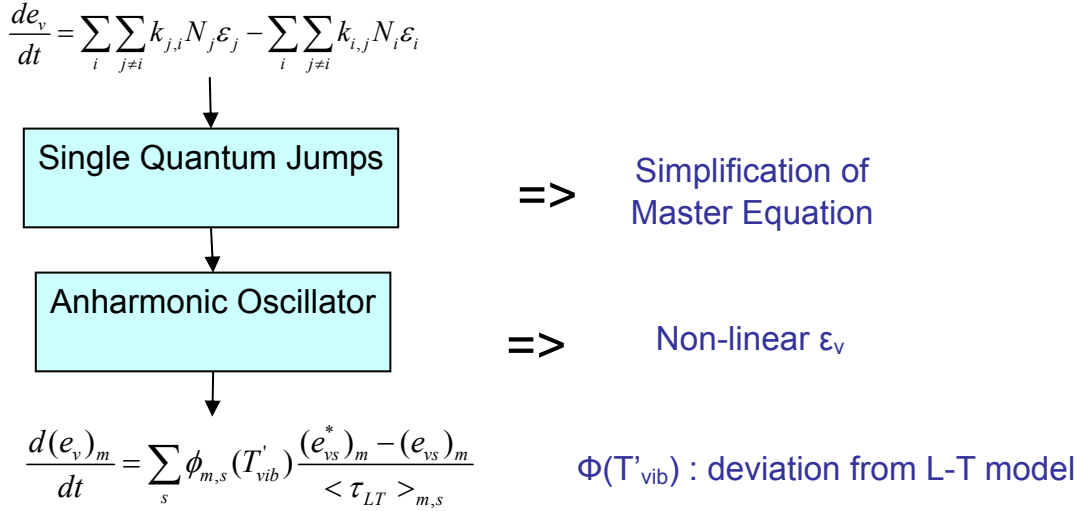


Fig 4.8 Overview of derivation for Ruffin's model

In the above relation, the LHS represents evolution of vibrational energy of m^{th} species.

The term on the RHS, $\phi_{m,s}(T'_{vib}) \frac{(e_{vs}^*)_m - (e_{vs})_m}{\langle \tau_{LT} \rangle_{m,s}}$, represents the contribution due to

collision of the m^{th} species with species s. Thus adding up the contributions due to all the species, we get the evolution equation for $(e_v)_m$. The basic idea behind this model is to increase the L-T energy transfer rate by a factor of $\varphi(T_{vib})$ for the cases when the predicted rate is slower compared to real case. However, the definition ensures that this factor remains nearly 1 for regions such as post shock flows. This happens mainly for the temperature range given by $T_{vib}/T < 1$.

To capture the physics of the process more accurately, Ruffin defines three different effective vibrational temperatures for the different ranges of quantum numbers. The choice of this effective vibrational temperature is such that it captures the dominant

physics for that particular range.

The first such range is defined as $\nu \leq \nu_1^*$, where

$$\nu_1^* = \text{minimum } \nu \text{ for which } (K_{v+1,v}^{VT})_{m,s} > (K_{v+1,v}^{VV})_{m,s}$$

Thus for this limit, the V-V-T transfers have more dominance and the distribution is approximated by Treanor Distribution. For the case of compression or post shock flows, V-T transfer dominates for all quantum levels and hence $\nu_1^* = 0$.

The second range is given as $\nu > \nu_2^*$, where the most rapid anharmonic V-T rates dominate, where $\nu_2^* = \text{minimum } \nu \text{ for which both of these conditions hold:}$

$$(K_{v+1,v}^{VT})_{m,s} > 1 \times 10^3 (K_{v+1,v}^{VV})_{m,s}$$

$$(K_{v+1,v}^{VT})_{m,s} > 10(\nu + 1) (K_{1,0}^{VT})_{m,s}$$

The third range, $\nu_1^* < \nu \leq \nu_2^*$, is characterized by V-T transition rates and the distribution can be approximated by Boltzmann distribution at effective vibrational temperature.

Expressions for ν_1^* and ν_2^* are obtained using curve fit methods. Data for these curves are available in [58] and [59] for combinations on N₂, CO₂, CO, Ar. It should be noted that a common value of ν_1^* as well as ν_2^* is used when a mixture of species is present. This common value is the molar fraction weighted average of individual species combination values.

$$(\nu_1^*)_m = \sum_s (\nu_1^*)_{m,s} W_{m,s} / \sum_s W_{m,s}$$

$$(\nu_2^*)_m = \sum_s (\nu_2^*)_{m,s} W_{m,s} \Bigg/ \sum_s W_{m,s} \quad (4.12)$$

Thus the rate acceleration factor $\varphi_{m,s}(T_{vib})$ is defined as

$$\varphi_{m,s} = \frac{1}{\rho(e_{vib})_m} \sum_{\nu=0}^{\nu_{\max}} (\nu+1) \Delta E_\nu (F_\nu)_{m,s} (N_{\nu+1})_m, \quad (4.13)$$

where population distribution can be expressed as

$$(N_\nu)_m = [(N)_m / Q_{vib}] \exp \left[-\nu \left(\frac{\theta_\nu}{T'_{vib}} \right) \right] \quad (4.14)$$

and

$$Q_{vib} = \sum_{\nu=0}^{\nu_{\max}} \exp \left(-\nu \frac{\theta_\nu}{T'_{vib,\nu}} \right). \quad (4.15)$$

The effective vibrational temperature for level ν can be defined as

$$\begin{aligned} T'_{vib} &= \frac{T_{vib_0}}{1 - x_e \frac{T_{vib_0}}{T} (\nu + 1)}, & \nu < \nu_1^* \\ &= \frac{T_{vib_0}}{1 - x_e \frac{T_{vib_0}}{T} (\nu_1^* + 1)} \left[\frac{1 - x_e (\nu_1^* + 1)}{1 - x_e (\nu + 1)} \right] & \nu_1^* < \nu < \nu_2^* \\ &= T'_{vib} \left[\frac{\nu}{(\nu - 1) + \frac{T'_{vib}}{T} (1 - 2x_e \nu)} \right] & \nu > \nu_2^* \end{aligned} \quad (4.16)$$

4.6.4 Comparison of the Three Vibrational Models

Ruffin [58] has shown the comparison between the three approaches to model the vibrational energy transfer rate (figure 4.9). In this figure, Y-axis (ϕ) represents how much the Ruffin's simplified anharmonic model and other models deviate from each other:

$$\phi = \frac{(de/dt)_{\text{Model}}}{(de/dt)_{\text{Landau Teller}}}$$

The value of ϕ is 1 for Landau Teller model by definition.

It can be seen in the figure that for heating environments ($T_{vib}/T < 1$), ϕ is not very different from unity. Thus the temperatures in the range $1000 \text{ K} < T < 5000 \text{ K}$, the Landau–Teller relaxation model is a reasonable approximation for relaxations in heating environments such as those in postshock flows. In cooling relaxations though, $T_{vib}/T > 1$, Landau Teller model predicts slower V-T transfer rates compared to anharmonic models. This deviation becomes prominent for $T_{vib}/T > 2.5$.

However using the Ruffin's simplified relaxation model, the predictions for ϕ are in good agreement with the master equation results for cases where V-T energy transfer rates dominate [60]. For extreme cases of thermal nonequilibrium($T_{vib}/T > 4.5$), the V-V energy transfer becomes significant. Thus the predicted energy transfer rate of the anharmonic relaxation model is too low, but it is still more accurate than values from Landau Teller model. Another advantage of using Ruffin's model is that it is computationally very inexpensive compared to the full master equation model. For example, although L-T model takes only 1 s for this simulation, Ruffin's simplified anharmonic model takes almost 4 s on the same. It should be noted that full master

equation model would take almost *1500 s* on the Cray Y-MP computer.

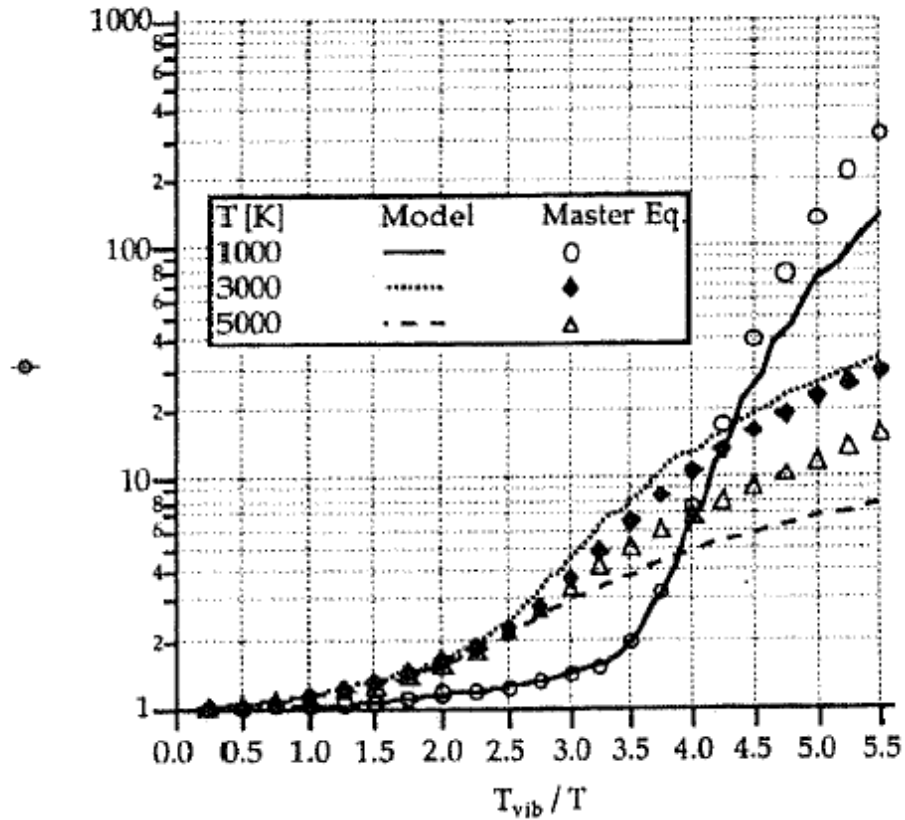


Fig 4.9 Comparison of the three models [58]

4.7 Chemical Models

For quasi-steady state flows, the reaction rate constant is modeled using the Arrhenius equation in the form:

$$k_f(T_{eff}) = C_f T_{eff}^n \exp(\theta_d / T_{eff}), \quad (4.17)$$

where $T_{eff} = T_{translational}$. However for the cases when the thermodynamic state of the gas is undergoing such rapid changes that the internal energy state does not satisfy the quasi-steady state condition, the above equation cannot be used for $T_{eff} = T_{translational}$. Thus, a model is needed which reflects the physics of nonequilibrium flows.

The main problem consists in determining the influence of molecular vibrational distribution on the rate of dissociation and recombination. The secondary objective is to quantify the influence of recombination and dissociation on the vibrational energy distribution. There are two main approaches found in literature:

- (1) Physicochemical studies which allow the construction of interaction models based on a specific and detailed approach of dissociative collisions and the determination of statistical properties such as dissociation constants, vibrational energy lost per dissociation etc ([35]-[39]). These models are difficult to implement computationally, but are physically more realistic in spite of frequent restrictive assumptions.
- (2) Semi-empirical approach for building models leading to simple relations which gives rate constants as a function of vibrational temperature ([23],[40],[41]). These models are more attractive and useful for hypersonic flows.

For the present study, we consider models based on approach (2). To understand these couplings, it is important to understand the primary coupling (vibration-chemistry) and secondary coupling (chemistry-vibration) separately. Basic steps for the derivation of the most general vibration-chemistry coupling model will be shown. This will be followed by the determination of models which are simpler than the general model.

4.7.1 Vibration –Chemistry Coupling

Consider the following reactions:



The latter reaction represents the summation of the former reaction for different combinations of v and w . Thus, we can write

$$\frac{\partial c_{AB}}{\partial t} = c_{AB}c_C \sum f_{AB}(v)k_d(v) - c_{AC}c_B \sum f_{AC}(w)k_d(w), \quad (4.18)$$

where $k_d(v) = \sum_{w=0}^{w_{\max}} k(v, w)$, $k_d(w) = \sum_{v=0}^{v_{\max}} k(w, v)$.

$k(v, w)$ represents the rate constant of the reaction in which a v -excited AB molecule decomposes, and an AC molecule excited in the w -th state is formed. $f_i(v)$ represents the population distribution function of the discrete vibrational states v of molecule i

However, we can also write

$$\frac{\partial c_{AB}}{\partial t} = c_{AB}c_C k_f - c_{AC}c_B k_b \quad (4.19)$$

Thus comparing the above two equations, we can obtain expression for the bulk rate constants k_f and k_b , if we know the distribution functions $f_i(v)$. Thus,

$$k_f = \sum f_{AB}(v) k_d(v)$$

$$k_b = \sum f_{AC}(w) k_d(w) \quad (4.20)$$

4.7.2 Chemistry-Vibration Coupling

Consider collision of molecule AB in v th vibrational state with another molecule C. This can be represented by the reaction shown above:



The total vibrational energy content of species AB is diminished by an amount that is equal to the vibrational energy content of $AB(v)$, represented as $\varepsilon_{vib,AB}(v)$. However, some energy also appears due to the formation of $AB(w)$, which is represented as $\varepsilon_{vib,AB}(w)$. Thus the rate at which vibrational energy for molecule AB is produced and the rate at which it is lost are given as

$$\begin{aligned} \dot{\omega}_{va,AB} G_{va,AB} &\equiv \dot{\omega}_{va,AB} \sum_{v=0}^{v_{\max}} \frac{k_d(v)}{k_f} f_{AB}(v) \varepsilon_{vib,AB}(v) \\ \dot{\omega}_{app,AB} G_{app,AB} &\equiv \dot{\omega}_{app,AB} \sum_{v=0}^{v_{\max}} \varepsilon_{vib,AB}(v) \sum_{w=0}^{w_{\max}} \frac{k(w,v)}{k_b} f_{AC}(w) \end{aligned} \quad (4.21)$$

where the subscripts va and app represent the vanishing and appearing energies. Thus, in general, the evolution equation of vibrational energy for molecule i will have an extra term Q_{C-V} given as

$$Q_{C-V,i} = \sum_j (\dot{\omega}_{app,ij} G_{app,ij} - \dot{\omega}_{va,ij} G_{va,ij}) \quad (4.22)$$

4.7.3 Coupled Vibrational-Chemistry-Vibrational(CVCV) Modeling

Based on above concepts, the CVCV model is derived after making the following assumptions:

- 1.) All vibrational states of a molecular species X_i are populated according to a Boltzmann distribution characterized by a vibrational temperature $T_{vib,i}$.
- 2.) The molecule X_i is an rotationless harmonic oscillator

Thus the relation for the rate constant $k(v,d)$ can be written as

$$k(v,d) = \Lambda k^E \exp[(\varepsilon_{vib,i}(v)/\Re)(1/T + 1/U_i)] \quad \varepsilon_{vib,i}(v) \leq \alpha A$$

$$k(v,d) = \Lambda k^E \exp[\varepsilon_{vib,i}(v)/\Re U_i + \alpha A/\Re T_i] \quad \varepsilon_{vib,i}(v) > \alpha A$$

where,

$$\Lambda = \frac{\exp(-\alpha A/RT) Q_{vib,i}^{D_i}(T)}{\exp(-\alpha A/RT) Q_{vib,i}^{\alpha A}(-U_i) + Q_{vib,i}^{D_i}(T_i^*) - Q_{vib,i}^{\alpha A}(T_i^*)} \quad (4.23)$$

D_i and A represent the dissociation energy of molecule X_i and activation energy of the reaction respectively. $Q_{vib}^r(T)$ denotes the partition function given as

$$Q_{vib}^r(T) = \frac{1 - \exp(-\Upsilon/\Re T)}{1 - \exp(-\Theta_{vib,i}/\Re T)} \quad (4.24)$$

U_i is taken to be a measure of the extent to which the upper vibrational levels are more reactive due to a cross section enlargement at higher excitation.

The other models can be derived from this general model by setting the different parameters particular values. One such model given by Treanor and Marrone assumes that only dissociation reaction takes place. This is the case when $A = D_i$ and $\alpha = 1$ in the above formulation, and is called preferential coupled vibration-dissociation-vibration (CVDV) model [23]. Neglecting the effects of the dissociation reactions on the vibrational energy exchange ($Q_{C-V} = 0$) leads us to preferential coupled vibration-dissociation (CVD) model.

Making the assumption that dissociation occurs only from the last bound quantum state, we obtain the ladder model [24]. The formula for rate constant becomes

$$k_{d_{eff}}(T, T_v) = k_{d_{eq}}(T) \exp[\varepsilon_v(\frac{1}{T} - \frac{1}{T_v})] \frac{Z_{vib}[T]}{Z_{vib}[T_v]}, \quad (4.25)$$

where Z_{vib} is the vibrational partition function and ε_v is the energy of quantum level v . Assuming $U_i = \infty$, for the above methods, we get the non-preferential CVDV [22] and CVD [21] models. Thus dissociation is assumed to occur from all vibrationally excited states with equal probability. For the CVD model, the rate constant is given as [20]

$$k_{d_{eff}}(T, T_v) = k_{d_{eq}}(T) \frac{\theta}{T_d} \frac{1 - \exp(-T_d/T_v + T_d/T)}{\exp(\theta/T_v - \theta/T) - 1} \frac{\exp(\theta/T_v) - 1}{\exp(\theta/T) - 1} \quad (4.26)$$

The above models are complex and not easy to implement in CFD codes. Thus a much simpler empirical formula was given by Park [3] where T_{eff} is modeled as

$$T_{eff} = \sqrt{TT_v} \quad (4.27)$$

Therefore, the rate constant can be modeled as

$$k_{d_{eff}} = k_d(T_{eff}) = C_d T_{eff}^n \exp(\theta_d / T_{eff}) \quad (4.28)$$

This approach is named as the Park's two temperature model [20]. Currently, this is the most commonly used model for hypersonic simulations. The various models and the corresponding assumptions are shown in figure 4.10.

4.8 Transport Models

The accurate prediction of mixture viscosity, thermal conductivity and diffusion coefficient is a critical component in the computation of hypersonic viscous flows. Prediction of these parameters in hypersonic nonequilibrium flows becomes a big challenge as they deviate from the values for thermally and calorifically perfect gases. We still do not have well established models for such cases. The early research in this field focused on the determination of single or binary gas mixture properties based on kinetic theory [26]-[29]. However, the subsequent work focused on curve fits or approximations to obtain mixture viscosity, thermal conductivity and diffusion coefficient of multi component gas mixtures [30]-[34]. Using the first approach of models based on exact kinetic theory for the determination of transport properties can make the problem CPU intensive. Thus curve fitting methods are preferred for simulation of hypersonic flows.

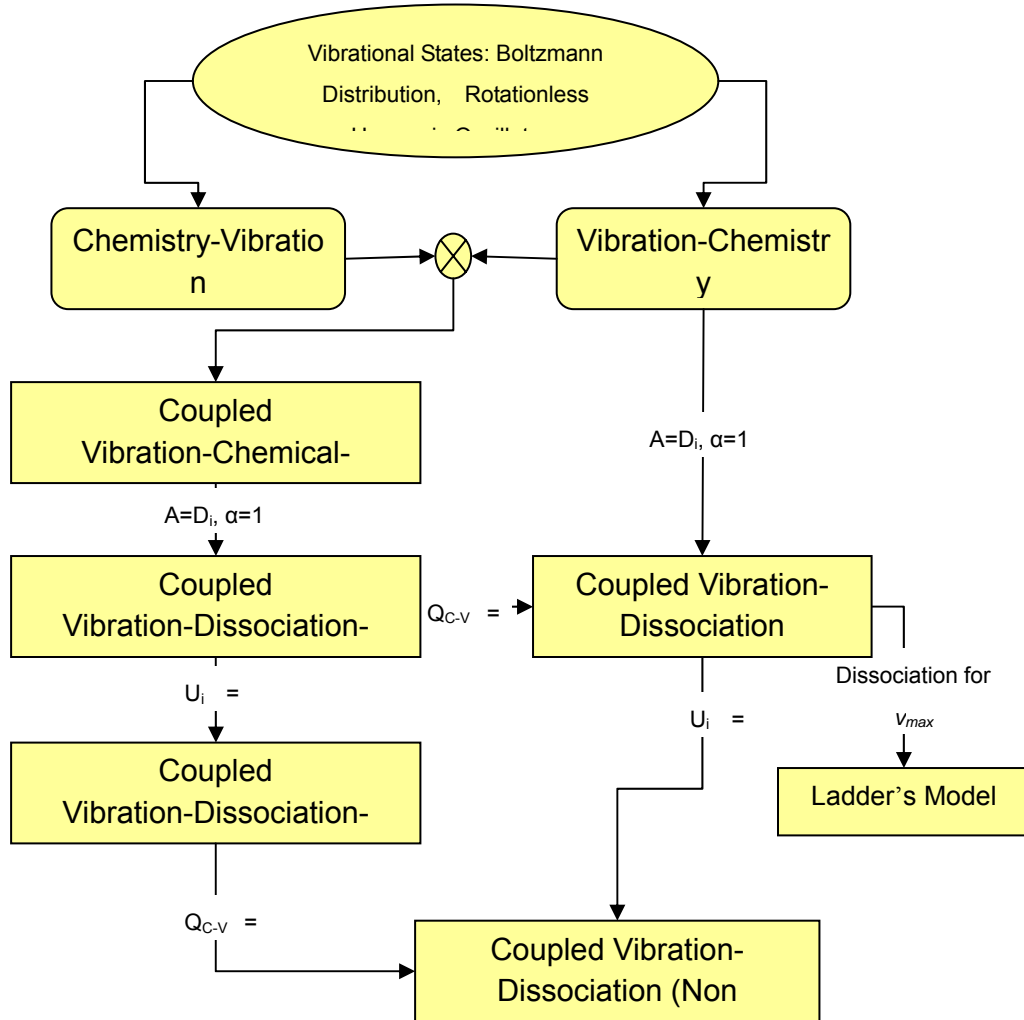


Fig 4.10 Classification of the chemistry models

For a single species, the viscosity and thermal conductivity are given to a good approximation by the following formulas,

$$\mu_i = 2.6693 \times 10^{-5} \frac{\sqrt{M_i T}}{\bar{\Omega}_{ii}^{(2,2)}} \frac{gm}{cm - sec} \quad (4.29)$$

And

$$K_{tr,i} = \frac{15}{4} \frac{\mu_i R}{M_i} \frac{cal}{cm\text{-sec}\text{-}K}, \quad (4.30)$$

$$K_{int,i} = R \frac{\mu_i}{M_i} \left(\frac{\rho D_{ii}}{\mu_i} \right) \left(\frac{C_{p,i}}{R} - \frac{5}{2} \right) \frac{cal}{cm\text{-sec}\text{-}K} \quad (4.31)$$

where $K_{tr,i}$ is the translational component of the thermal conductivity and $K_{int,i}$ is the component of thermal conductivity resulting from the diffusion of internal excitation energy of the molecules, M_i is the molecular weight in gm/gm-mole, R is the universal gas constant, D_{ii} is the component of self diffusion, and Ω_{ii} is average collision cross-in range of sections for the molecules within an Armstrong. The self diffusion component is the reciprocal Schmidt number and is related to the collision cross sections through the relation:

$$D_{ii} = 2.6280 \times 10^{-3} \frac{\sqrt{T^3 / M_i}}{\bar{\Omega}_{ii}^{(1,1)} p} \frac{cm^2}{sec} \quad (4.32)$$

The complication in the above relations arises due to the presence of the term Ω_{ii} , which brings an uncertainty in the determination of transport properties. The expression for Ω_{ii} further complicates the above relations. Thus it is computationally practical to find the transport properties as a polynomial of temperature T . This polynomial is found by curve fitting on experimental data.

Thus the expressions for the transport properties are found as,

$$\begin{aligned}
\mu_i &= e^{E_{\mu_i}} T^{[A_{\mu_i}(\ln T)^3 + B_{\mu_i}(\ln T)^2 + C_{\mu_i} \ln T + D_{\mu_i}]}, \frac{gm}{cm - sec} \\
K_{f,i} &= K_{tr,i} + K_{int,i} = e^{E_{K_{f,i}}} T^{[A_{K_{f,i}}(\ln T)^3 + B_{K_{f,i}}(\ln T)^2 + C_{K_{f,i}} \ln T + D_{K_{f,i}}]}, \frac{cal}{cm - sec} \\
\bar{D}_{ij} &= e^{D_{\bar{D}_{ij}}} T^{[A_{\bar{D}_{ij}}(\ln T)^2 + B_{\bar{D}_{ij}} \ln T + C_{\bar{D}_{ij}}]}, \frac{cm^2 - atm}{sec}
\end{aligned} \tag{4.33}$$

The values of the curve fit coefficients are given in [20]. The values obtained from the tables from the mentioned reference are for a $p = 1 \text{ atm}$ and thus needs to be corrected depending on the pressure. This is done using the relation:

$$\begin{aligned}
\frac{\mu_i(p_e)}{\mu_i(1 \text{ atm})} &= \frac{K_{ir,i}(p_e)}{K_{ir,i}(1 \text{ atm})} = \frac{K_{int,i}(p_e)}{K_{int,i}(1 \text{ atm})} = \\
&= \frac{\ln \left[2.09 \times 10^{-2} \left(\frac{T}{1000} \right)^4 + 1.52 \left(\frac{T}{1000} \right)^{8/3} \right]}{\ln \left[2.09 \times 10^{-2} \left(\frac{T}{1000 p_e^{1/4}} \right)^4 + 1.52 \left(\frac{T}{1000 p_e^{1/4}} \right)^{8/3} \right]}
\end{aligned}$$

The problem becomes more complex when a mixture of different species is present in the flow. For such cases, the standard approaches are

(a) Wilke's mixing formula

In this method, kinetic theory with some simplifying assumptions is used to compute the mixture transport properties. Using this method, the mixture viscosity is expressed as [29]

$$\mu = \sum_i \frac{\chi_i \mu_i}{\phi_i} \frac{N-s}{m^2} \quad (4.34)$$

Similarly, the mixture thermal conductivity becomes,

$$\kappa = \sum_i \frac{\chi_i \kappa_i}{\phi_i} \frac{J}{m-s-K} \quad (4.35)$$

Here, ϕ_i is defined as

$$\phi_i = \sum_j \frac{\chi_j \left[1 + \sqrt{\frac{\mu_i}{\mu_j}} \left(\frac{M_j}{M_i} \right)^{1/4} \right]^2}{\sqrt{8 \left(1 + \frac{M_i}{M_j} \right)}} \quad (4.36)$$

The multicomponent diffusion coefficient D_m is related to the binary diffusion coefficients D_{ij} for the diffusion of the species i into j by means of the expression

$$D_{im} = \frac{1 - \chi_i}{\sum_j \frac{\chi_j}{D_{ij}}} \quad (4.37)$$

where χ is the species mole fraction and M is the molecular mass.

(b) Collision Integrals

This is the most rigorous method of obtaining the mixture properties and uses an

approximation to Chapman-Enskog formula [20]. The total mixture viscosity under this formulation is given as

$$\kappa_{\text{int}} = \sum_i \frac{\chi_i \frac{R}{M_i} \frac{C_{P_{\text{int},i}}}{R}}{\sum_j \chi_j \frac{Sc_{ij}}{\mu_{ij}}} \quad \frac{J}{m-s-K}$$

Defining $\mu_{ij} = \frac{1}{\bar{\Delta}_{ij}^{(2)}}$, the formula for the total viscosity can be rewritten as

$$\mu = \sum_i \frac{\chi_i}{\sum_j \frac{\chi_j}{\mu_{ij}}} \quad \frac{N-s}{m^2}$$

where $\bar{\Delta}_{ij}^{(2)}$ is defined as

$$\bar{\Delta}_{ij}^{(2)} = \frac{8}{3} \left[\frac{2M_i M_j}{\pi N_A k T (M_i + M_j)} \right]^{1/2} \pi \bar{\Omega}_{ij}^{(1,1)}$$

Curve fits for μ_{ij} for 11 species air are available in [42]. The mixture translation thermal conductivity thus becomes

$$\kappa_{tr} = \sum_i \left[\frac{\frac{15}{4} \frac{R}{M_i} \chi_i}{\sum_j \frac{\alpha_{ij} \chi_j}{\mu_{ij}}} \right] \quad \frac{J}{m-s-K}$$

where

$$\alpha_{ij} = 1 + \frac{\left[1 - \frac{M_i}{M_j}\right] \left[0.45 - 2.54 \frac{M_i}{M_j}\right]}{\left[1 + \frac{M_i}{M_j}\right]^2}.$$

The mixture internal thermal conductivity can be written as

$$\kappa_{\text{int}} = \sum_i \frac{\chi_i \frac{R}{M_i} \frac{C_{P,\text{int},i}}{R}}{\sum_j \chi_j \frac{Sc_{ij}}{\mu_{ij}}} \frac{J}{m-s-K},$$

where Sc_{ij} is the Schmidt number, the curve fits for which can be found in [42].

(c) Species Summation

In this method, the mixture viscosity/thermal conductivity is obtained by computing the sum of the products of species mole fraction with each species' viscosities/conductivities. It is assumed that there is no interaction between the various species. Thus the mixture viscosity is given as

$$\mu = \sum_i \chi_i \mu_i \quad \frac{N-s}{m^2}$$

And the mixture thermal conductivity becomes

$$\kappa = \sum_i \chi_i K_i \qquad \frac{J}{m-s-K}$$

CHAPTER V

NUMERICAL METHODS: NS, BGK AND SA MODELS

In this chapter, the numerical methods pertaining to Navier Stokes(NS) method, Boltzmann BGK method and Spalart Allmaras(SA) turbulence model are discussed.

5.1 Navier Stokes Equations

The analytical solution of the Navier-Stokes equations is practically impossible to solve for most of the practical flow problems barring a very few simple flows. Iterative numerical methods have been used to solve these equations. A wide range of numerical techniques are available to solve such kind of equations. Such techniques can be broadly classified into the following groups based on the discretization method:

1. Finite Difference schemes [62, 63, and 64]: In this approach, the solution domain is represented by a structured array of discrete nodes. The Navier Stokes equations are written in terms of the nodal values by replacing the derivatives with their finite difference approximations, obtained through Taylor series expansion about the nodal values. Although the method tends to be very accurate, problems occur due to the finite difference representation of the derivatives when discontinuities are present in the solution. Additionally, the advantage of higher accuracy is lost when solving for complex geometries. For such cases, the solution domain has to be mapped from physical space to the computational space using Jacobians.
2. Finite Volume Schemes [65, 66]: In this approach, the solution domain is divided into small control volumes termed as cells. The integral form of Navier Stokes is solved for

each of these cells. This is done by keeping an account of the net flux passing through each cell and updating the cell properties based on this residual or net flux. A steady state is achieved when the net flux passing through each cell becomes almost zero. The flux passing through a cell interface is calculated based on the properties of the cells sharing a common interface boundary.

The advantage of Finite Volume method over the finite difference method is in its ability to handle the discontinuities in the flow field. Since the Navier Stokes equations are solved in their integral form, it becomes easier to treat the derivatives which otherwise are theoretically infinite. Another main advantage of the Finite Volume methodology is the conservative nature of the approach. Since the flux being added into one cell will be deducted from one of the neighboring cells, the scheme remains conservative over the whole solution domain. Treatment of complex geometries becomes simpler using this approach. However, extending the accuracy of the scheme to higher orders is not straightforward and one needs to implement reconstruction schemes.

3. Finite Element Schemes [67]: In this approach, the solution domain is broken down into subdomains which are termed as elements. These elements can be of arbitrary shape and sizes. Unlike the Finite Volume scheme where the flow properties are assumed to be constant or vary linearly in the cells, in Finite Element methodologies the solution is assumed to take some particular functional form within an element. Therefore the solutions obtained from Navier Stokes equations lie in such a functional domain. Finite element methods have been used successfully to solve incompressible as well as compressible flow problems. One of the major disadvantages of using these methods is the computational cost. Since the Finite Element methods involve matrix inversions, the solvers are much slower in terms of computational time when compared to FDM and FVM solvers and needs parallelization to be used for practical purposes.

After comparing the pros and cons of the three methodologies listed above, it was decided to go ahead with the Finite Volume methodology.

5.2 Finite Volume Methods

As discussed in previous section, the first step for this approach is to subdivide the computational domain into finite volumes. This can be done in many ways, but it must be ensured that the volumes should fill the entire domain without overlapping. In the node centered approach there is one node in each volume and the flow properties are solved for at this node. The node in most cases coincides with the centroid of the volume. The volumes can have any polygon shape (triangles, quadrilaterals) in 2D and polyhedral shapes (tetrahedrons, hexahedrons, prisms etc.) in 3D. For this study, structured 2D grids are used and therefore the cells are almost rectangular.

The second step involves discretization of the integral form of Navier Stokes equations for application to finite volume cells. In finite volume, the cell centre flow properties are assumed to represent the cell average value as shown in equation (5.1), i.e.,

$$Q_{ctr} = \frac{1}{V_r} \int Q(x, y, z) dV \quad (5.1)$$

where V_r is the volume of r^{th} cell.

Also, the fluxes are assumed to be uniform along each cell interface. Using these two assumptions one can simplify the integral form of Navier Stokes equation to the equation represented in equation.

$$Q_{ctr}^{n+1} = Q_{ctr}^n - \frac{1}{V_r} \int_{t_n}^{t_{n+1}} \sum_k F_k \cdot \hat{n}_k dS_k dt \quad (5.2)$$

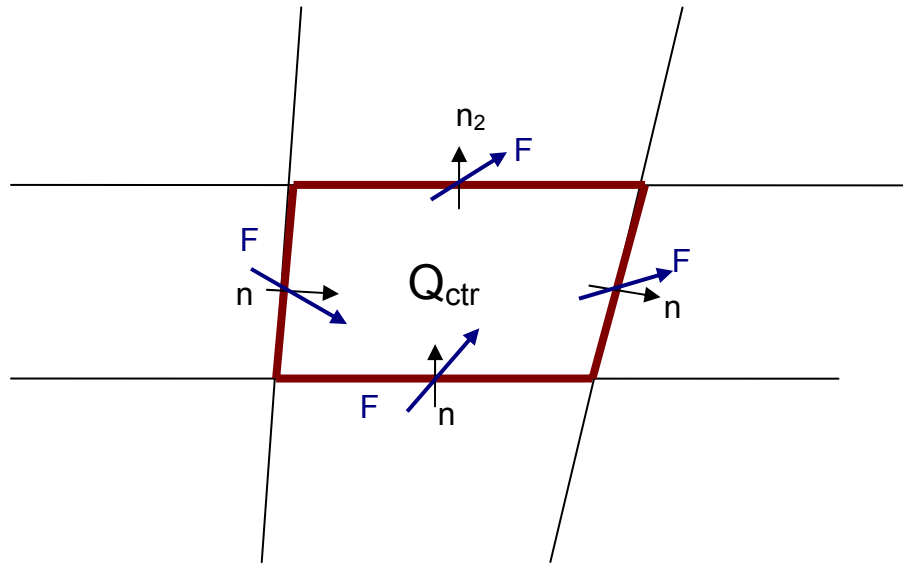


Fig 5.1 Fluxes across the edges of a cell

For 2D, the fluxes across the edges of a cell are shown in fig 5.1. Thus, knowing the solution in the domain at time step n , the solution at time step $n+1$ can be determined by calculating the fluxes across all the boundary interfaces. The fluxes are calculated using flux solvers and are represented as a function of the properties of the cells sharing the interface on which flux is being solved. It should be noted that for second order accurate flux calculation, the flux can be a function of flow properties at three or more cells surrounding the interface. Details of such calculations will be discussed in the chapter VI.

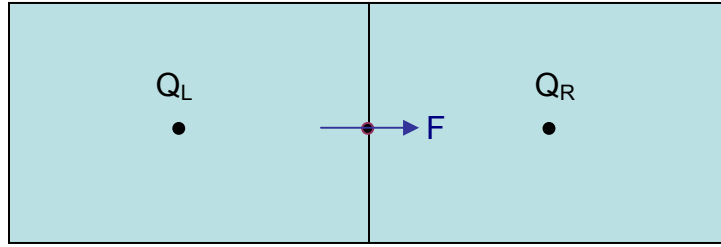


Fig 5.2 Flux across a cell interface

The flux along the common edge shown in figure 5.2 can be represented mathematically as

$$F = F(Q_L, Q_R) \quad (5.3)$$

The simplest form of flux solver is to obtain flux at the interface by averaging the fluxes at the neighboring cell centers. However such an approach leads to poor accuracy and completely fails when shocks [68] are present in the flow. An ideal solver should have low level of dissipation to handle the discontinuities in the flow. This is because a high dissipation leads to smearing of discontinuities such as shocks or contact discontinuities. On the other hand, low levels of dissipation can lead to generation of noise such as spurious oscillations in the solution. Hence most of the present flux solvers try to vary the dissipation levels with the flow parameters. Thus dissipation levels are lowered in the smooth regions of the flow whereas in the regions of discontinuities the dissipation levels can be very high.

It should be remembered that the flux term shown above has both inviscid and viscous fluxes. The methods for calculation of the inviscid fluxes are discussed in the next section. Numerical techniques to integrate the term on the RHS of equation (5.2) are presented in chapter VII.

5.3 Inviscid Fluxes

The flux solvers discussed in this section belong to the wave approach category of flux calculation methods [69]. These wave based methods can be further categorized into two classes: the Flux Vector Splitting method and Flux Difference Splitting method. Two schemes, each of them belonging to one of these two classes, have been implemented in this study.

5.3.1 Steger Warming Schemes

Steger and Warming (55) proposed the first flux vector splitting scheme, based on wave speed splitting. The flux vector can be split as

$$F(U) = F^+(U) + F^-(U) \quad (5.4)$$

where the characteristic values of df^+/du are all nonnegative and the characteristic values of df^-/du are all nonpositive. In standard notation,

$$\frac{dF^+}{dU} \geq 0, \quad \frac{dF^-}{dU} \leq 0 \quad (5.5)$$

Therefore the flux is split on the basis of the direction in which it is traveling. The flux can be written in terms of the characteristic diagonal matrix as

$$F = \frac{dF}{dU} U = AU = Q\Lambda Q^{-1}U, \quad (5.6)$$

where

$$\Lambda = \begin{vmatrix} \lambda_1 & 0 & 0 \\ 0 & \lambda_2 & 0 \\ 0 & 0 & \lambda_3 \end{vmatrix}, \quad \lambda_1 = u - a, \lambda_2 = u, \lambda_3 = u + a \quad . \quad (5.7)$$

Q is the eigen matrix corresponding to eigenvalues of $A = dF/dU$

Thus the split equation can also be written as

$$F(U) = Q\Lambda^+Q^{-1} + Q\Lambda^-Q^{-1} \quad (5.8)$$

where Λ^+ and Λ^- are based on eigenvalues split as $\lambda = \lambda^+ + \lambda^-$. One of many such possible splits was proposed in [55]:

$$\begin{aligned} \lambda_i^+ &= \max(0, \lambda_i) = \frac{1}{2}(\lambda_i + |\lambda_i|) \\ \lambda_i^- &= \min(0, \lambda_i) = \frac{1}{2}(\lambda_i - |\lambda_i|) \end{aligned} \quad (5.9)$$

Thus using the above values, F^+ and F^- come out to be

For $M \leq -1$:

$$F^+ = 0$$

$$F^- = F$$

For $-1 < M \leq 0$:

$$F^+ = \frac{\rho}{2\gamma} (u+a) \begin{bmatrix} 1 \\ u+a \\ \frac{u^2}{2} + \frac{a^2}{\gamma-1} + au \end{bmatrix}, \quad F^- = \frac{\gamma-1}{\gamma} \rho u \begin{bmatrix} 1 \\ u \\ \frac{u^2}{2} \end{bmatrix} + \frac{\rho}{2\gamma} (u-a) \begin{bmatrix} 1 \\ u-a \\ \frac{u^2}{2} + \frac{a^2}{\gamma-1} - au \end{bmatrix}$$
(5.10)

For $0 < M \leq 1$:

$$F^+ = \frac{\gamma-1}{\gamma} \rho u \begin{bmatrix} 1 \\ u \\ \frac{u^2}{2} \end{bmatrix} + \frac{\rho}{2\gamma} (u+a) \begin{bmatrix} 1 \\ u+a \\ \frac{u^2}{2} + \frac{a^2}{\gamma-1} + au \end{bmatrix}, \quad F^- = \frac{\rho}{2\gamma} (u-a) \begin{bmatrix} 1 \\ u-a \\ \frac{u^2}{2} + \frac{a^2}{\gamma-1} - au \end{bmatrix}$$
(5.11)

For $M > 1$:

$$F^+ = F,$$

$$F^- = 0$$

Therefore, for supersonic right running flows, all of the waves are right running and the flux vector splitting correctly attributes all of the flux to right running waves and none to left running waves. Similarly, for supersonic left running flows all of the waves are left running and the flux vector splitting correctly attributes all of the flux to left running waves and none to right running waves. For subsonic flows, waves are both left and right running, and the flux vector splitting correctly attributes some to left and some to right running waves, although it should be noted that the exact physical proportions

may not be correct. Thus the flux in figure 5.2 can be given as

$$\begin{aligned} F(U_L, U_R) &= F(U_L), \quad u_{edge} \geq a \\ &= F(U_R), \quad u_{edge} \leq -a \\ &= F(U_L, U_R), \quad -a < u_{edge} < a \end{aligned}$$

5.3.2 Roe's Scheme

Suppose the flow properties are assumed to be constant along the cell. Therefore one can pose a Riemann problem at the interface as shown in the figure (5.3). Therefore, the flux on the edge can be given as

$$\hat{F}_{i+1/2}^n = F(u_{RIEMANN}(x_{i+1/2}, t)) \quad (5.12)$$

where $F(u_{RIEMANN}(x_{i+1/2}, t))$ is found using the Roe's scheme.

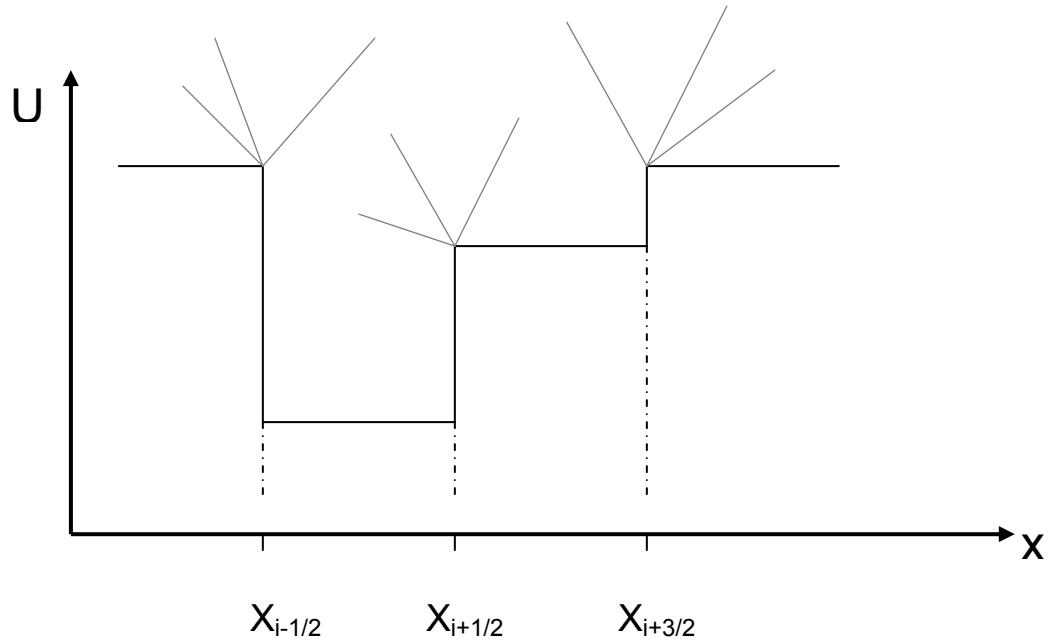


Fig. 5.3 Piecewise-constant reconstruction (Riemann problem)

It should be noted that the Riemann solution assumes that the waves from the different cell edges do not interact during a single time step. Since the CFL condition is applied at the beginning of the time step, it is usually advisable to leave a safety margin by choosing CFL number less than one.

Due to the nonlinear nature of the Flux vector, finding the exact solution to the Riemann problem can be very expensive. Also, since the flow properties are constant over the whole cell, it does not really make sense to solve the Riemann problem exactly as the initial conditions are approximate. Therefore in Roe's scheme, simplifying assumptions are made to solve an approximate Riemann problem [53].

One of the most important assumptions is the linearization of Flux vector, which can be represented as follows:

$$F(U) = F(U_L) + A_{RL}(U - U_L) \quad (5.13)$$

Solving the approximate value of A_{RL} the flux at the interface can be found as

$$\hat{F}_{i+1/2}^n = \frac{1}{2}(F(U_{i+1}^n) + F(U_i^n)) - \frac{1}{2} \sum_{j=1}^3 (R_{i+1/2}^n)_j | \lambda_{i+1/2}^n |_j (\Delta v_{i+1/2}^n)_j \quad (5.14)$$

Here, $\lambda_{i+1/2}^n$ are the j^{th} eigenvalues corresponding to A_{RL} ; $R_{i+1/2}^n$ is the j^{th} right eigenvector corresponding to A_{RL} ; and $\Delta v_{i+1/2}^n$ is the jump (left to right) in the j^{th} characteristic variable. Derivation of the parameters in the RHS of equation above is tedious and can be found in [69].

5.4 Boundary Conditions

The boundary conditions are the constraints applied to the boundaries and play an important role in determining the solution of the domain. For finite volume methods, use of ghost cells is very popular. The center of the ghost cell is the mirror image of the boundary cell about the boundary edge/surface in 2D/3D. A typical ghost cell is shown in figure 5.4.

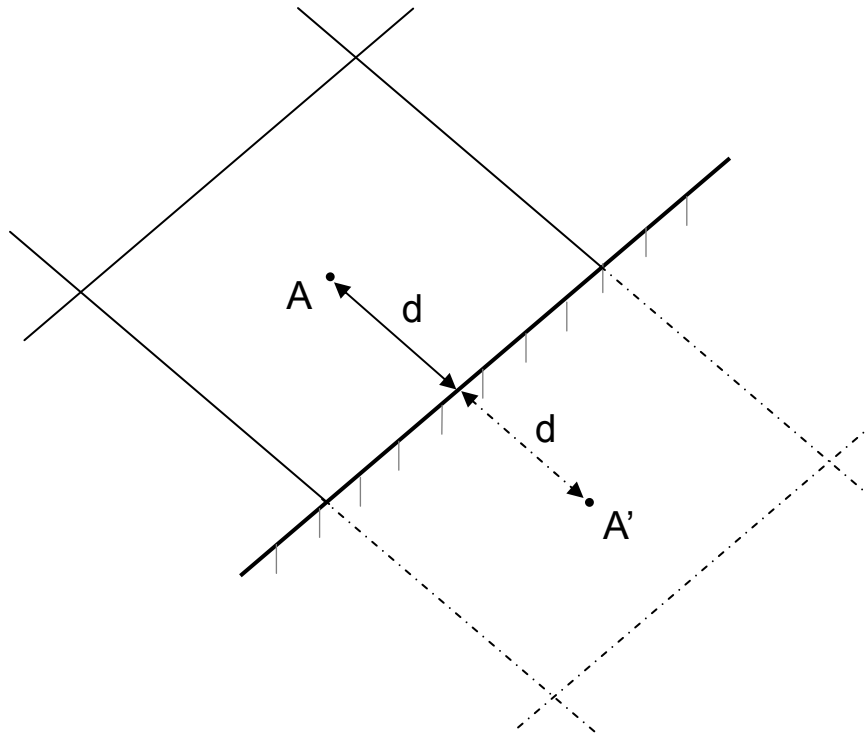


Fig.5.4 Layout of the ghost cell

For the inflow ghost cells, the flow properties are initialized according to the inflow conditions specified and these values are kept constant throughout the simulation. This is because the inflow conditions used are supersonic and thus the solution should not affect the supersonic inflow values. Similarly properties at the outflow ghost cells are set to be equal to the adjacent internal cell.

For the inviscid walls, all the flow properties at the ghost cell are set as those of the adjacent internal cell except for the velocities. The velocity at the ghost cell is set as the mirror image of the velocity of the internal cell about the boundary interface. Mathematically, this means that the component of velocity along the boundary remains constant whereas the velocity along the normal reverses direction. Therefore the velocity at the ghost cell can be expressed as

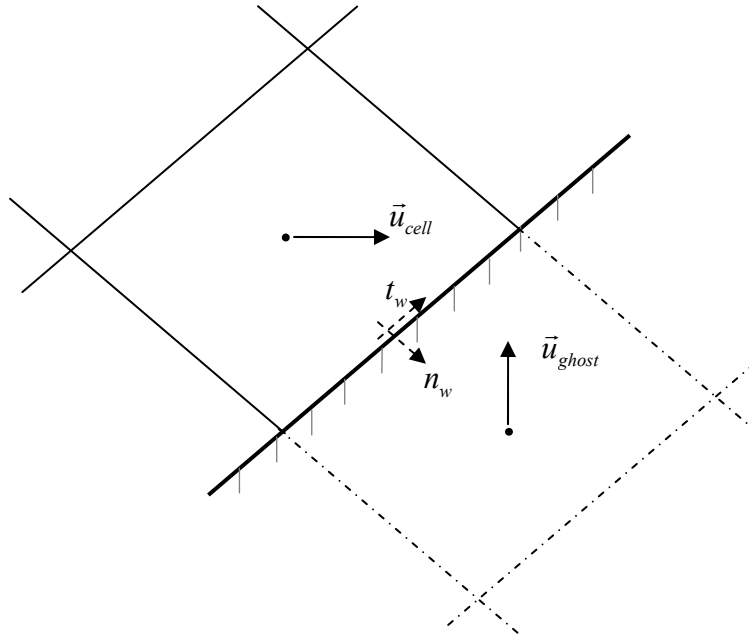


Fig 5.5 Boundary condition for inviscid wall

$$\vec{u}_{ghost} = -(\vec{u}_{cell} \cdot n_w) n_w + (\vec{u}_{cell} \cdot t_w) t_w \quad (5.15)$$

where n_w and t_w are the unit vectors along the normal and tangential directions to the boundary as shown in figure 5.5. It should be noted that the symmetry boundary conditions are also calculated using the same formula.

For viscous walls, both the normal as well as tangential components need to be reversed. Thus it is easy to see that the ghost cell velocity will be given as

$$\vec{u}_{ghost} = -(\vec{u}_{cell} \cdot n_w) n_w - (\vec{u}_{cell} \cdot t_w) t_w \quad (5.16)$$

Since in both kinds of wall boundary conditions we have copied the temperatures

from the internal cell to the ghost cells, it follows that all the walls are assumed to be adiabatic for this study.

5.5 BGK Boltzmann Equation

The exact solution of the BGK Boltzmann equation at a cell interface $x_{j+1/2}$ at time t can be written as

$$f(x_{j+1/2}, t, u, v, \xi) = e^{-t/\tau} f_0(x_{j+1/2} - ut) + \frac{1}{\tau} \int_0^t e^{-(t-t')/\tau} g(x', t', u, v, \xi) dt' \quad (5.17)$$

where $x' = x_{j+1/2} - u(t-t')$ represents the particle trajectory and f_0 is the initial gas distribution function f at the beginning of each time step ($t=0$). Assuming cell interface as the origin, we can set $x_{j+1/2} = 0$ without any loss of generality.

The gas distribution function f_0 which is given at the beginning of each time step can be written in the neighborhood of a cell interface as

$$f_0 = \begin{cases} g^l[1+a^l x] - \tau g^l(a^l u + A^l), & x \leq 0 \\ g^r[1+a^r x] - \tau g^r(a^r u + A^r), & x \geq 0 \end{cases} \quad (5.18)$$

The first part of the expression represents the equilibrium part of the distribution function. The quantities g^l and g^r are the Maxwellian distributions at the left and right of a cell interface. The slopes a^l and a^r represent the spatial derivative of a Maxwellian and are calculated using the slopes of the conservative variables.

The second term which is first order in τ represents the nonequilibrium part of distribution function and is obtained from the Chapman-Enskog expansion of the BGK

model. Detailed formulation on the calculation of coefficients (a^l, A^l, a^r, A^r) can be found in [74].

It should be noted that for flow simulations where the cell size cannot properly resolve the viscous flow structure, the nonequilibrium part vanishes. An example where this term becomes significant would be the region inside a shock. Therefore, if the cell size is fine enough to resolve the physical shock structure, the distribution will deviate from the Maxwellian because of the presence of this nonequilibrium term.

The second term in equation (5.17) can be evaluated using the following expression for g :

$$g = g_0[1 + (1 - H[x])\bar{a}^l x + H[x])\bar{a}^r x + \bar{A}t] \quad (5.19)$$

where $H[x]$ is the Heaviside function defined as

$$H[x] = \begin{cases} 0, & x < 0, \\ 1, & x \geq 0. \end{cases}$$

g_0 is the local Maxwellian distribution function located at the cell interface. As a consequence of the above relation it can be seen that g has different slopes for $x < 0$ and $x > 0$. The details for the calculation of \bar{a}^l , \bar{a}^r and \bar{A} can be found in [74].

Making the substitutions from eq (5.18) and eq (5.19) into eq (5.17) we get the expression for f as:

$$\begin{aligned}
f(x_{j+1/2}, t, u, v, \xi) = & (1 - e^{-t/\tau}) g_0 + \tau(t/\tau - 1 + e^{-t/\tau}) \bar{A} g_0 \\
& + (\tau(-1 + e^{-t/\tau}) + t e^{-t/\tau})(\bar{a}^l H[u] + \bar{a}^r(1 - H[u])) u g_0 \\
& + e^{-t/\tau}((1 - u(t + \tau)a^l)H[u]g^l + (1 - u(t + \tau)a^r)(1 - H[u])g^r) \\
& + e^{-t/\tau}(-\tau A^l H[u]g^l - \tau A^r(1 - H[u])g^r)
\end{aligned} \tag{5.20}$$

Thus the flux along x-direction can be found by integrating the above f to give:

$$\begin{pmatrix} F_\rho \\ F_{\rho u} \\ F_{\rho v} \\ F_E \end{pmatrix} = \int u \begin{pmatrix} 1 \\ u \\ v \\ \frac{1}{2}(u^2 + v^2 + \xi^2) \end{pmatrix} f(x_{j+1/2}, t, u, v, \xi) d\xi \tag{5.21}$$

The same procedure can be repeated to calculate the flux along y-direction.

5.6 Collision Time

As derived in section 4.4, the final expression for τ comes out to be

$$\tau = \mu / P$$

This formula works well for cases when cell size is much smaller than the dissipative length scale determined by the physical viscosity. However, in cases of shocks where the cell sizes are usually not enough to resolve the wave structure and thus the physical structure has to be replaced by a numerical one. Since the shock thickness is determined by the viscosity, the effective viscosity should also be changed to account for this new shock thickness. The additional dissipation is provided by the following term:

$$\tau = \frac{\mu}{p} + \frac{|\rho_l/\lambda_l - \rho_r/\lambda_r|}{|\rho_l/\lambda_l + \rho_r/\lambda_r|} \Delta t$$

It can be seen that in the smooth regions the second term on the RHS vanishes. However, the term will have a significant value at the interface of a discontinuity such as a shock.

It should be noted that the ratio of average collision time τ and the numerical time step Δt has a significant effect on the stability of the BGK method. For the cases when $\tau/\Delta t \gg 1$, there are effectively no collisions taking place for any particular iteration i . Since viscous effects are a direct consequence of the collision between molecules, the effective viscosity for the whole domain will decrease. Therefore there is a higher chance of the solver becoming unstable since less amount of dissipation is available to handle the discontinuities. It is therefore important to keep the ratio $\tau/\Delta t < 1$. In Euler cases, this ratio is maintained around 0.01-0.05 by defining the collision time as

$$\tau = C_1 \Delta t + \frac{|\rho_l/\lambda_l - \rho_r/\lambda_r|}{|\rho_l/\lambda_l + \rho_r/\lambda_r|} \Delta t$$

5.7 Spalart Allmaras Model

The compressible Spalart Allmaras model is given as

$$\rho \frac{D\tilde{v}}{Dt} = \rho b_{prod}(S, \tilde{v}, d) - \rho b_{dest}(\tilde{v}, d) + \rho b_{trip}(d_T) + b'_{dif}(\tilde{v})$$

Using the discretizations discussed in chapter II for the terms on the RHS, the implicit backward Euler solution procedure [85] can be used to ensure a positive turbulence field at each update. However, such a method requires expensive inversion of

a large sparse matrix in 2-D or 3-D. Therefore an approximate factorization of the implicit operator is required although the unconditional positivity is lost. Thus a small timestep is required so that factorization error does not ruin the positivity of the solution.

For 2-D, the conventional ADI method can be used. The equation can be written as

$$[\rho I - \Delta t \bar{M}_\xi] [\rho I - \Delta t \bar{M}_\eta] [\rho I - \Delta t (\bar{P} - \bar{D})] \Delta v^n = \Delta t (M_\xi + M_\eta + P - D) v^n \quad (5.22)$$

where M_ξ and M_η are finite differences in the ξ and η coordinate directions respectively, while \bar{M}_ξ and \bar{M}_η are the corresponding implicit operators. For an unsteady problem, the Alternating Direction Implicit (ADI) method can have convergence problems and requires several sub-iterations for every timestep. A more efficient factorization is suggested in [83]. However, for steady state problems, such subiterations are not required and the conventional ADI method can be applied.

It should be noted that although the turbulence equations are solved implicitly, the mean flow equations can still be updated using explicit method. Such an approach is discussed in [86].

5.8 Boundary and Initial Conditions

The eddy viscosity variable $\tilde{\nu}$ is put to zero on the no slip boundary. On the inlet boundary $\tilde{\nu} < \nu/10$ is suggested in literature [83]. However, in case of a steady state flow over smooth flat plate with no shocks present, there is no instability to induce turbulence in the flow. Therefore, $\tilde{\nu}$ of the order of 10ν has to be used to see turbulence effects.

On the extrapolation boundaries like supersonic outflows, the Neumann condition is used, i.e.,

$$\nabla \tilde{v} \cdot \hat{n} = \frac{\partial \tilde{v}}{\partial \hat{n}} = 0$$

A uniform initial condition equal to the freestream value can be given.

CHAPTER VI

RECONSTRUCTION AND LIMITERS

6.1 Introduction

The discussion of the last chapter assumed that the flux solver is of first order accuracy. To increase the accuracy to higher orders, reconstruction schemes are used. The reconstruction can be achieved in two steps: interpolation and limiting. In the interpolation step, the value of the flow variables is found at particular locations such as a cell interface or a vertex using the values of flow properties in the surrounding cells. In the limiter step the reconstructed values are recalculated to prevent oscillations to develop in the solution. These reconstructed values are then used as input to the flux solver. In an alternate postprocessing form, the reconstruction can also be applied to the calculated flux instead of applying them to the flow properties in the preprocessing form. However, only the former approach will be discussed here.

6.2 Linear Interpolation

In the previous chapter, it was assumed that the value at the cell center is constant throughout the cell region, the constant value being the value at the cell center. Thus the flowfield was approximated as a series of piecewise constant states. Such an approach is also known as Gudonov's first order scheme [75]. Thus the flow conditions to the immediate left and right of the cell interface are given as

$$Q_{i+1/2}^L = Q_i, \quad Q_{i+1/2}^R = Q_{i+1}$$

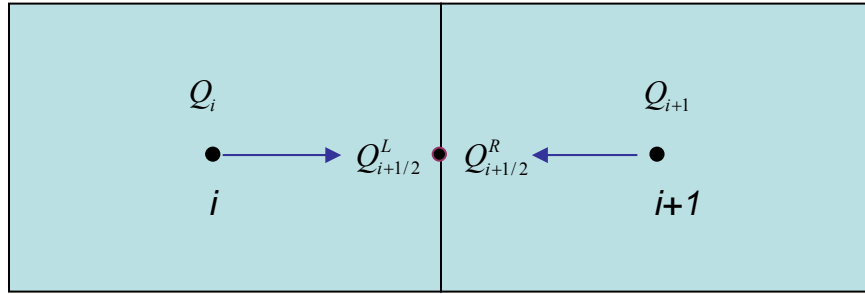


Fig 6.1 Left and right states of Q

The locations of these variables are depicted in figure 6.1.

Such a scheme tends to be inaccurate and causes smearing of flow features, especially shocks and discontinuities. One of the simplest methods of increasing this accuracy is to assume the flow property to vary linearly across a cell region. Thus we can define the interface values as

$$\begin{aligned} Q_{i+1/2}^L &= Q_i + S_L \cdot (x_{i+1/2} - x_i) \\ Q_{i+1/2}^R &= Q_{i+1} - S_R \cdot (x_{i+1} - x_{i+1/2}) \end{aligned} \quad (6.1)$$

The values of S_L and S_R depend on the choice of reconstruction method and the choice of limiter. Logically the simplest choice of S_L and S_R would be

$$\begin{aligned} \vec{S}_L &= \nabla Q_i \\ \vec{S}_R &= \nabla Q_{i+1} \end{aligned} \quad (6.2)$$

The methods discussed in the coming sections are based on the above idea. Since information of nodes i or $i+1$ or both may be required for calculation of the slopes S_L and S_R , the stencil for the scheme will have 3 or more points. Therefore it is possible to increase the accuracy to higher orders by appropriately choosing these slopes.

Two of the popular linear interpolations schemes are discussed here.

6.2.1 MUSCL Based Scheme

The Monotone Upstream-centered Schemes for Conservation Laws (MUSCL) [68] based scheme is the most commonly used method for interpolation on structured grids. The left and right state values are calculated using the following relation

$$\begin{aligned} Q_{i+1/2}^L &= Q_i + \frac{1}{4}[(1-\kappa)\Delta_i^- + (1+\kappa)\Delta_i^+] \\ Q_{i+1/2}^R &= Q_{i+1} - \frac{1}{4}[(1-\kappa)\Delta_{i+1}^+ + (1+\kappa)\Delta_{i+1}^-] \end{aligned} \quad (6.3)$$

here $\Delta_i^- = Q_i - Q_{i-1}$, $\Delta_i^+ = Q_{i+1} - Q_i$ and κ is a parameter which blends the upstream and downstream information. The constraint of κ is

$$-1 \leq \kappa \leq 1$$

For the special case $\kappa = -1$, the MUSCL scheme reverts to fully one sided scheme. In this study the fully one sided scheme was implemented.

However the formulation given above is applicable to uniform grids only. For non-uniform grids, a modified MUSCL scheme [76] can be used:

$$\begin{aligned} Q_{i+1/2}^L &= Q_i + \frac{1}{2}\psi(r_L)(U_i - U_{i-1}) \\ Q_{i+1/2}^R &= Q_{i+1} - \frac{1}{2}\psi(r_R)(U_{i+2} - U_{i+1}) \end{aligned} \quad (6.4)$$

where

$$r_L = \frac{Q_{i+1} - Q_i}{Q_i - Q_{i-1}} \frac{b}{a}, \quad r_R = \frac{Q_{i+1} - Q_i}{Q_{i+2} - Q_{i+1}} \frac{c}{a} \quad (6.5)$$

$$a = \| \vec{r}_{i+1} - \vec{r}_i \|, \quad b = \| \vec{r}_i - \vec{r}_{i-1} \|, \quad c = \| \vec{r}_{i+2} - \vec{r}_{i+1} \|$$

Even though this method is applicable for non-uniform grids, it still assumes that the mesh on which the flow is being solved is orthogonal. Therefore MUSCL scheme cannot be applied to unstructured grids in the above two forms, (6.3) and (6.4).

6.2.2 Green Gauss Reconstruction

The Green Gauss reconstruction is based on the following exact integral relation:

$$\int_{\Omega'} \nabla u d\Omega = \int_{\partial\Omega'} u \vec{n} dS$$

where

Ω : volume for 3D/ area for 2D

S : area for 3D/ perimeter for 2D

u : V_x, V_y, ρ, P or T

\vec{n} : the normal to cell face/edge

These quantities are depicted in figure 6.2. Assuming that u varies linearly, the above relation can be approximated for as

$$\nabla u d\Omega = \frac{1}{2} \sum_i^N (u_i + u_0) \vec{n}_i dS_i \quad (6.6)$$

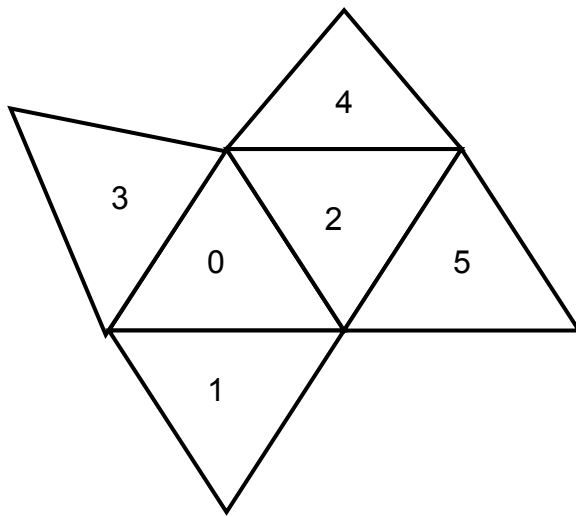


Fig 6.2 Gradient at vertex 0 using values of immediate neighbors 1,2, and 3

Therefore after calculating the gradient, the value at the interface can be reconstructed as

$$\begin{aligned} Q_{i+1/2}^L &= Q_i + \nabla Q_i \cdot (\vec{x}_{i+1/2} - \vec{x}_i) \\ Q_{i+1/2}^R &= Q_{i+1} - \nabla Q_{i+1} \cdot (\vec{x}_{i+1} - \vec{x}_{i+1/2}) \end{aligned} \quad (6.7)$$

It can be seen that unlike MUSCL scheme, we cannot control the proportion of upstream and downstream information to be used in reconstruction.

6.3 Limiters

The methods discussed above work well if the flow properties vary smoothly in the domain. However in presence of discontinuities or strong variation in properties, the above methods can result in oscillatory solutions and instability. This is because at such extreme conditions the value of the gradient calculated can be unusually high.

Therefore limiters are used to limit the reconstructed values by scaling the value of the gradient. An ideal limiter should reduce the interpolation to first order Godunov scheme in regions of severe discontinuities, and should have no effect in the smooth regions. For this study, the Total Variation Diminishing (TVD) Reconstruction Schemes are discussed.

6.4 TVD Schemes

Ideally the solution should be free of any sort of numerical oscillations. A scheme satisfying the monotonicity condition as well as the entropy condition will give such a solution. However, it is very difficult to devise higher order monotone schemes. Therefore the schemes are tested against a less severe condition which ensures oscillation free solutions. One such condition is the based on the Total Variation (TV) of the solution. Examples of monotonic and non-monotonic solutions are shown in figure 6.3.

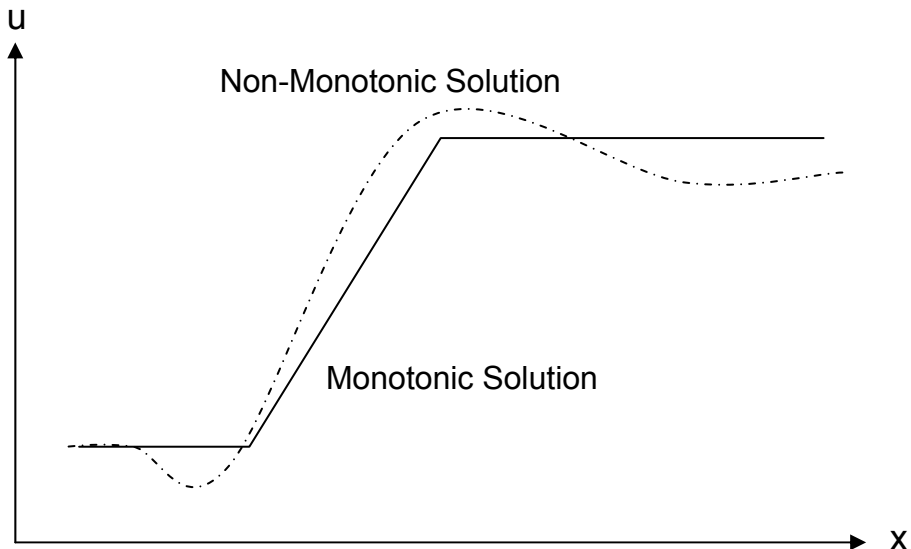


Fig 6.3 Example of monotonic and non-monotonic solution

TV is defined as

$$TV = \int_{\Omega} \left| \frac{\partial u}{\partial x} \right| dx \quad (6.8)$$

which for discrete solution translates to

$$TV(u) = \sum_i^N |u_{i+1} - u_i| \quad (6.9)$$

A numerical scheme is TVD if it satisfies the following condition:

$$TV(u^{n+1}) \leq TV(u^n).$$

The useful property of TVD schemes is that the solutions are monotonicity preserving. However, these schemes do not satisfy the entropy condition.

An example is shown here of how a limiter works. In the first step of reconstruction, the solution can be represented as shown in the fig 6.4.

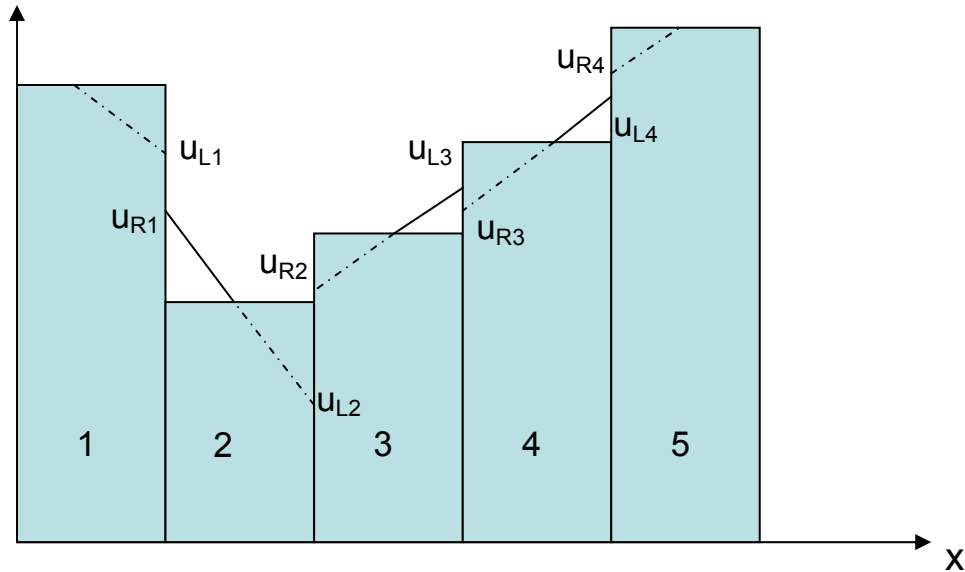


Fig 6.4 Solution without use of limiter

In this example, it can be seen that as we go across from cells 3 to 4, the values vary as $u = u_{R2}, u_{L3}, u_{R3}, u_{R4}$. It can be clearly seen that such a distribution is not monotonic. The function of the limiter is to ensure the TVD condition and thus ensure monotonicity. Thus after the second step of applying the limiter, the solution shown in the above example may typically look like the solution shown in fig 6.5.

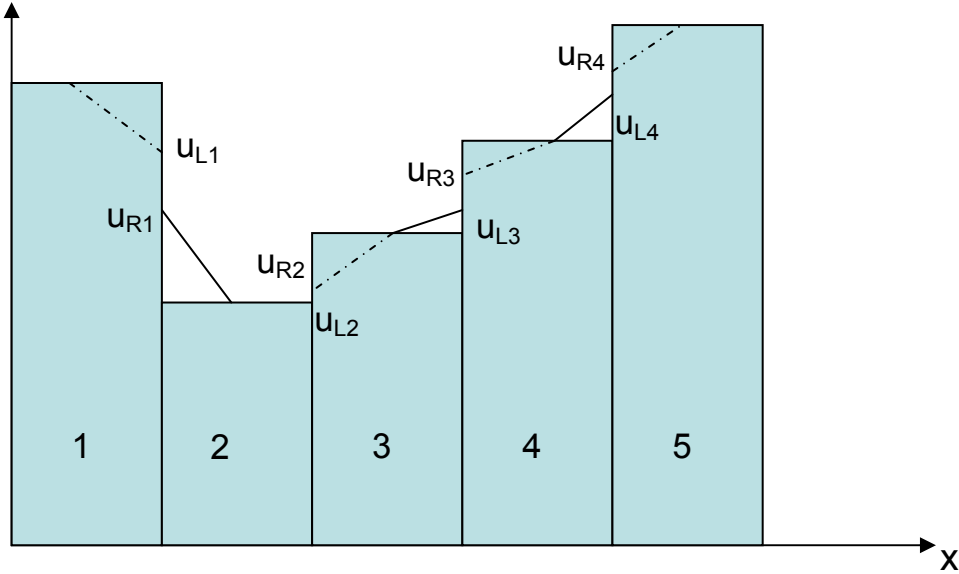


Fig 6.5 Solution after using limiter

Such a solution is monotonic locally at every interface. In the next two sections, description of two limiters used to ensure TVD conditions are given.

6.4.1 MinMod Limiter

Consider the interpolation step as given below

$$Q_{i+1/2}^L = Q_i + \phi(r_i) \nabla Q_i \cdot (\vec{x}_{i+1/2} - \vec{x}_i) \quad (6.10)$$

The effect of the limiter is introduced through the variable ϕ . It can be seen that limiter has no effect if the function $\phi = 1$. For this case, Minmod limiter function [68] is defined as

$$\phi(r) = m(1, r)$$

where r is defined as $r = \Delta^+ / \Delta^-$ and the function m is based on the minimum-modulus (minmod) function given as

$$m(x, y) = m(y, x) = sign(x) \max \{0, \min[|x|, y \cdot sign(x)]\} \quad (6.11)$$

This function returns 0 if x and y have different signs or the value of the argument with the smallest modulus.

The minmod limiter is popular for flow problems in which strong shocks are present. One of the disadvantages of this limiter is that it is not differentiable.

6.4.2 Van Albada Limiter

Using non-differentiable limiters can result in very slow convergence to a steady state solution. This is because such limiters can cause temporal oscillations due to which the residues never fall to the machine precision levels.

The Van Albada limiter [77] is a differentiable one. It is defined as

$$\phi(r) = \frac{r^2 + r}{r^2 + 1} \quad (6.12)$$

This limiter is good for steady state smooth flows. However, one of the disadvantages is that it can not be applied to unsteady flows.

CHAPTER VII

NUMERICAL ISSUES

7.1 Introduction

As mentioned in [43], a very common joke shared amongst CFD practitioners correctly describes a perceived problem with numerical predictions: “Everyone believes experimental results except the person who performed the experiment, and no one believes numerical results except the person who performed the prediction.” Nowhere is this statement more true (and more of a problem) than in hypersonic flow simulation.

The following complex features of hypersonic flows are what make their CFD analysis a challenging task:

- (a) Presence of vibrational, chemical nonequilibrium
- (b) Thin shock layers (high compression)
- (c) Entropy layers caused by highly swept and curved shock waves
- (d) Viscous/inviscid interactions
- (e) Real gas effects, including dissociation, ionization (high temperatures)
- (f) Rarefaction (high altitudes)

In the next few sections, some of the common practices in CFD used to counter some of the above mentioned problems will be discussed. The main steps involved in developing a CFD solver are discussed in the next section.

7.2 CFD Solver for Nonequilibrium Flow

The general governing equation for single species flow in vibrational nonequilibrium can be written as

$$\frac{\partial \underline{Q}}{\partial t} + \frac{\partial(G - G_v)}{\partial x} + \frac{\partial(H - H_v)}{\partial y} = S_{cv} \quad (7.1)$$

Where,

$$\underline{Q} = \left\{ \rho_1 \dots \rho_{vn} \ \rho u \ \rho v \ E \right\}^T$$

$$S_{cv} = \left\{ \dot{w}_1 \dots \dot{w}_{vn} \ 0 \ 0 \ 0 \right\}^T$$

The inviscid and viscous flow matrices are written as

$$G = \begin{Bmatrix} \rho_1 u \\ \vdots \\ \rho_{vn} u \\ \rho u^2 + p \\ \rho u v \\ (E + p)u \end{Bmatrix}, \quad G_v = \begin{Bmatrix} 0 \\ \vdots \\ 0 \\ \tau_{xx} \\ \tau_{xy} \\ \tau_{xx} u + \tau_{xy} v - (q_{tx} + q_{rx} + q_{vx}) \end{Bmatrix}$$

Here,

$$\begin{aligned} E &= \rho C_v T + \frac{1}{2} \rho |\vec{u}|^2 + E_v \\ \tau_{ij} &= \mu \left(\frac{\partial u_i}{\partial x_j} + \frac{\partial u_j}{\partial x_i} \right) + \delta_{ij} \lambda' \frac{\partial u_k}{\partial x_k}, \quad \lambda' = -\frac{2}{3} \mu \end{aligned} \quad (7.2)$$

$$\vec{q}_{t,r,v} = -\kappa_{t,r,v} \nabla T_{t,r,v}$$

$$P = \rho R T$$

The general flowchart showing the important steps in the CFD methods used for solving the above equations can be depicted in fig. 7.1.

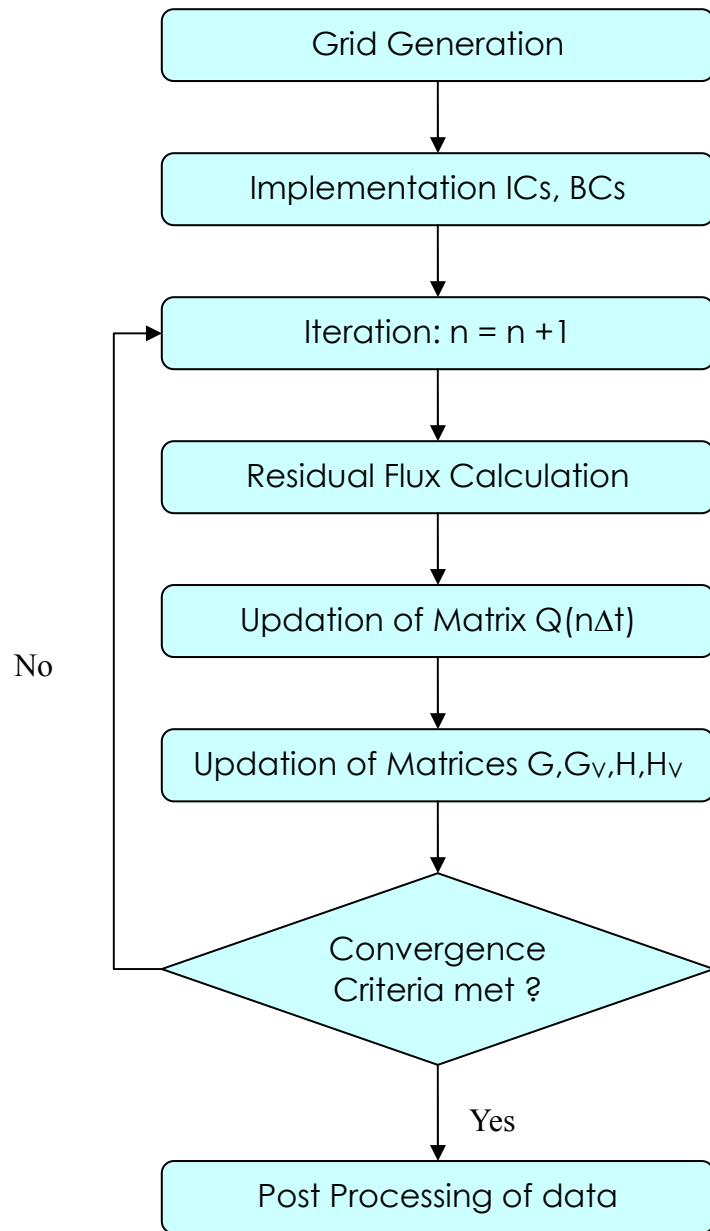


Fig 7.1 Basic Steps for a general CFD solver

The presence of complex hypersonic flow features makes the above steps (specially the process of grid generation, calculation of residual fluxes using differencing scheme and updation of matrices using integration schemes) a challenging task. The approaches found in literature for these steps will be presented in the next few sections.

7.3 Grid Generation

Grid generation has made great strides over the past decades and a number of commercially available programs are available that do a reasonably good job of creating grids around complex geometries. However, many of these softwares fail when creating grids for CFD analysis of hypersonic flows due to its difficult requirements. Grid generation for complex geometries can take anywhere from weeks to months even after using these commercial softwares.

Grids can be categorized as body fitted and non body fitted. The body fitted grids can be further categorized as structured and unstructured grids, while the non body fitted grids found in literature are the Cartesian grids.

Most industry still relies on body fitted grids for the grid generation process. For such grids, surface geometry definition and grid generation are still considered to be the biggest bottlenecks in the CFD process. However, unstructured grids are gaining popularity over structured grids as the process is more or less automated and requires much less human hours. They also offer geometric flexibility and efficient refinement capabilities which are not available in structured grids.

However even for unstructured grid generation, an initial explicit generation of surface grid is required which calls for a high level of expertise and has been one of the least automated steps in the numerical simulation process.

The requirement of surface grids is removed when using the non body fitted Cartesian grids. In this case the surface grid is obtained as a byproduct when the whole

grid has been generated. Such grid also helps to get rid of highly skewed cells that are sometimes obtained on the boundaries using the former approach. They also remove the need for transformation from physical to computational space.

However, such grids can cause timestep restriction, especially when the Cartesian grids intersect with the solid body giving rise to arbitrarily small cut cells. For steady state calculations, local time stepping can be used to avoid this limitation.

The quality of grids can have significant effects on the hypersonic flow solutions. One of the factors is the orientation of the grid relative to a shock. The numerical schemes need to address how to handle shocks with the grid in different orientations to the shock (discussed by Kim et al. [44]). Mesh refinement is required in regions of high flow gradients, which can be challenging without the knowledge of where all of those regions are located a priori. Adaptive mesh refinement methods such as that given by Pirzadeh (2001) have proven useful for improving the grid in regions of high flow gradients.

Near the surface of geometry, grid resolution can be crucial to the aerothermodynamic predictions being made. Papadopoulos et al. [45] showed that, “a computational mesh and a level of convergence which result in accurate surface-pressure and shear stress values do not guarantee accurate heat-transfer values.” It was also found that accurate predictions require careful monitoring of both the cell Reynolds number and the temperature jump near the wall. The cell Reynolds number is given by

$$\text{Re}_{cell} = \frac{\rho_{wall} a_{wall} \Delta y}{\mu_{wall}}$$

where, Re_{cell} is the cell Reynolds number,

ρ_{wall} is the density at the wall,

α_{wall} is the speed of sound at the wall,

Δy is the y-step size of the cell,

and μ_{wall} is the viscosity at the wall.

This parameter helps to ensure that the initial grid spacing near the wall is small enough to accurately deal with the viscous and heat-transfer effects that are present at the surface.

7.4 Time Integration Schemes

In order to obtain a steady state solution of hypersonic flows, the marching of unsteady solutions in an explicit manner is widely used. However, when chemical reactions are taking place, this approach creates a problem. This is due to the presence of the source terms that represent the production of species from finite rate chemical reactions, which causes stiffness in the system of equations.

Therefore a small CFL number is required which further results in limiting the timestep for the simulation. Thus the rate of convergence of the solution is affected. The problems listed here as well as the approaches used to avoid them are shown in fig. 7.2. These approaches are:

- (a) Sequential Method: In this method, the chemical equations are uncoupled from rest of the fluid dynamics equations and are solved sequentially [47].
- (b) Point Implicit Method: For this approach, the chemical source terms are treated implicitly at the time step $n+1$ while evaluating the convective terms effectively [48].
- (c) Implicit Method: The whole system of governing equations is solved implicitly in a coupled manner [49], [50].
- (d) Semi Implicit Method: This method is a combination of implicit as well as explicit schemes [51].

The implicit schemes, although computationally slower, had been very popular till recent times. The Implicit methods can be further categorized as Alternating Direction Implicit (ADI) and Lower-Upper (LU) methods.

The ADI method has been a popular one, but its inefficiency in 3D calculations and the requirement of matrix inversion makes it unattractive for nonequilibrium flow simulations. The LU schemes are found to be much more efficient and are gaining popularity. The

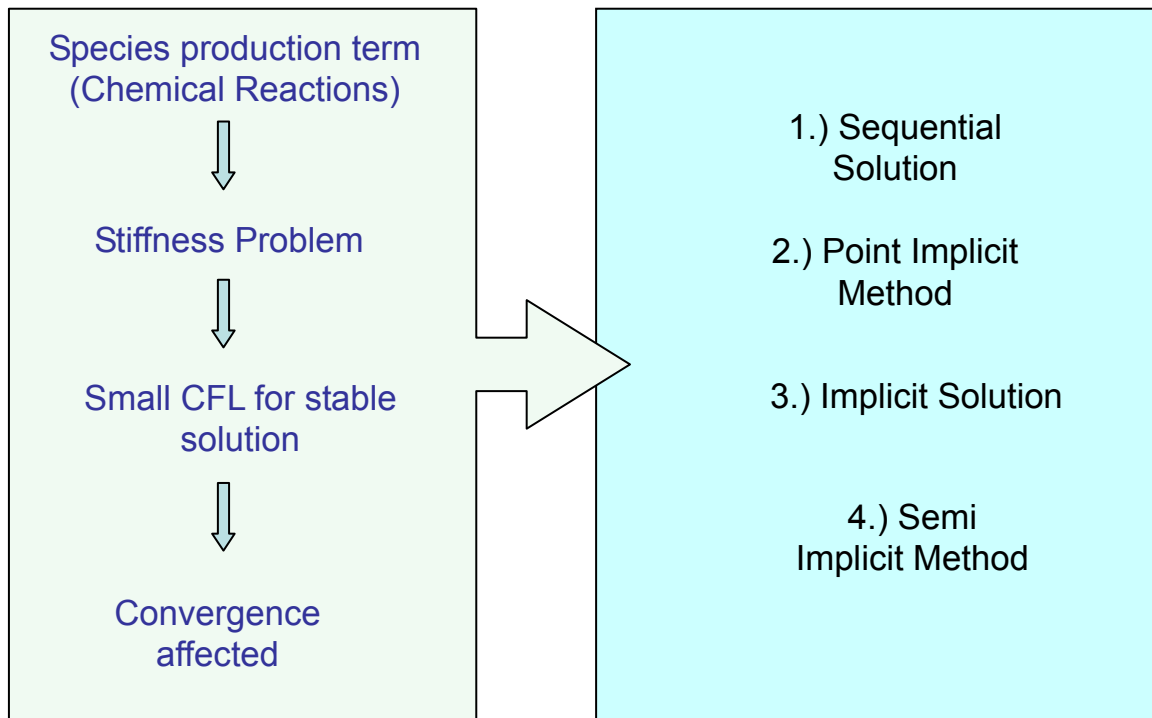


Fig 7.2 Timestepping limitations and the methods to eliminate it

The LU schemes can be further categorized into two methods [52]: LU-SSOR

(symmetric successive over relaxation) and LU-SW (Steger Warming). While the LU-SSOR gives a simpler implicit operator with less temporal damping [52], the LU-SW converges faster but requires more computations for each iteration. The comparison of LU and ADI methods is shown in fig 7.3.

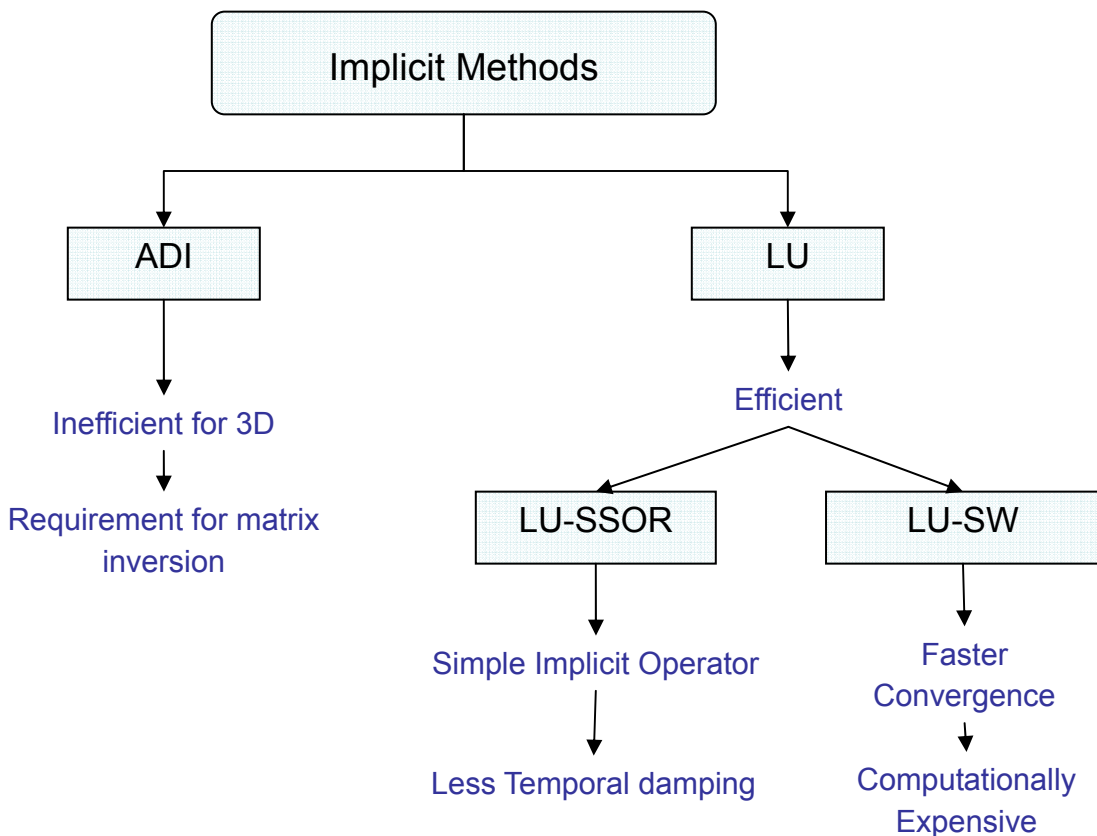


Fig 7.3 Comparison of different Implicit methods

7.5 Spatial Differencing Schemes

A variety of important numerical schemes have been developed over the years specifically to deal with the shocks that are formed at supersonic and hypersonic speeds.

A majority of these methods fall into the “shock capturing” approach, where the equations of fluid motion are solved to determine shock locations and strengths. One of the first approaches of this kind was the explicit method of Lax & Wendroff (1960) and the predictor-corrector scheme of MacCormack (1969).

A second method for predicting shocks is “shock fitting” approach, which was proposed by Moretti (1974). In this method, the Rankine-Hugoniot shock relations are used to determine shock jump conditions once the position of the shock is known. Most of the algorithms developed over the years belong to the shock capturing category.

It is very well known that shocks cause instabilities in numerical methods and the scheme should have the capability to take care of them. This is done either through explicit addition of numerical dissipation or through some sort of upwind differencing. However, the method of addition of numerical dissipation needed to dampen the shock leads to inaccurate predictions of viscous phenomenon such as vortical flows or boundary layers.

Therefore upwind schemes are preferred for eliminating the problem of shock instabilities. Gudonov’s exact Reimann solver was the first scheme which was able to capture shock waves without inducing spurious oscillations. Although Reimann Solvers were widely used due to their robustness and high resolution of shock waves, they were computationally very expensive.

Approximate Reimann Solvers were developed in order to make the above approach more practical. The flux difference schemes based on this method are Roe’s scheme [53], Osher’s scheme and the HLL scheme [54].

Another approach, known as the flux vector splitting method, is used for upwinding. The popular schemes that fall under this category are Steger-Warming [55], Van Leer [56] and Advection Upstream Splitting Method (AUSM) by Liou & Steffen [57].

The categorization of these upwind schemes and some advantages and

disadvantages are shown in the fig. 7.4.

Upwind Schemes		
Gudonov's Method	Approx. Riemann Solvers	Flux Splitting
<ul style="list-style-type: none"> Exact Riemann Solver <ul style="list-style-type: none"> Robust and high resolution of discontinuities Very Expensive 	<ul style="list-style-type: none"> Roe's Scheme <ul style="list-style-type: none"> Second order accuracy using MUSCL Minmod limiter to degenerate solution to 1st order accuracy near shocks HLL Scheme Osher's Scheme 	<ul style="list-style-type: none"> Steger Warming <ul style="list-style-type: none"> Preferred for steady state solution, FVS Van Leer <ul style="list-style-type: none"> Continuously Differentiable Flux Distribution, FVS Inclusion of nonequilibrium chemistry simple AUSM <ul style="list-style-type: none"> Low diffusion Flux Splitting

Fig 7.4 Classification of upwind schemes

CHAPTER VIII

RESULTS

The results obtained from the computational code for five test cases are presented in this chapter. The test cases and their intended purposes are shown in table 8.1.

Test Case	Purpose
Geometric Conservation Law Test	<i>Verification of conservation of mass momentum and energy of the domain.</i>
Shock tube test	<i>Comparison of shock capturing capabilities of BGK and Steger Warming, Roe's scheme</i>
Viscous flow over flat plate	<i>Testing capability of BGK in capturing the viscous effects</i>
Nonequilibrium hypersonic over blunt body using SW	<i>Comparison of performance of Green Gauss and MUSCL reconstruction scheme for supersonic flows</i>
Nonequilibrium hypersonic over blunt body using SW, BGK	<i>Comparison of performance of SW and BGK schemes for nonequilibrium flows.</i>

Table 8.1 The test cases and their objectives

8.1 Geometric Conservation Law Test

By the way of its construction, the Finite Volume methodology ensures that CFD codes observe the Geometric Conservation Law (GCL). This is a necessary condition to

maintain the integrity of the physical conservation laws. In this test case, it is verified whether the present Finite Volume implementation ensures GCL or not.

The geometry for the test case consists of a simple channel grid shown in fig 8.1. There are 100 cells along the x-direction and 50 cells along the y-direction. The ratio of specific heats is assumed to be constant at 1.4. At the start of the simulation, random velocities are assigned where the magnitudes of the velocities are less than the free stream velocity. The inflow is maintained at Mach 3. Since the inflow is supersonic, the inflow remains constant throughout the simulation. The wall boundaries are assumed to be adiabatic and frictionless.

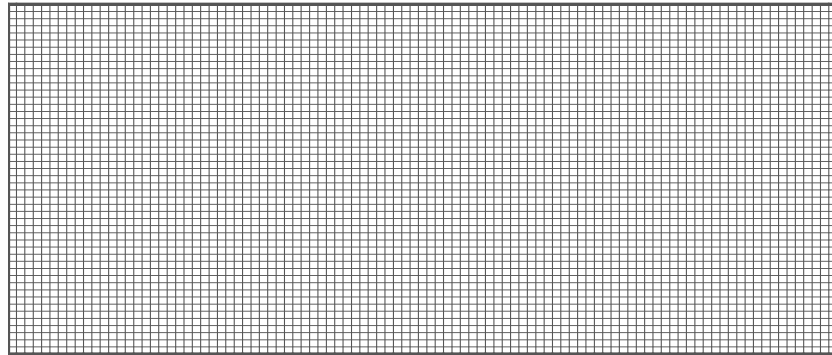


Fig 8.1 Mesh for the channel flow

Since the inflow boundary conditions are unchanged, physically the whole domain should have identical values with the inflow when convergence is reached. However, a code not satisfying GCL would incorrectly introduce perturbations into the solution and will be expected to gain or lose total mass.

The test case was run for Steger Warming, Roe's scheme and BGK scheme. The mass leakage in all the three cases turned out to be of the order of 10^{-16} . The order of error is acceptable since it is close to the machine precision. Therefore, it can be concluded that the current formulation satisfies the GCL.

8.2 Shock Tube Problem

Using the 1-D shock tube problem, we can compare the ability of different schemes in resolving shocks, contact discontinuity and expansion fans. The two dimensional shock tube considered in the present simulation has 100 cells along x-direction from $x=0$ to $x=1$, and 50 cells along y-direction from $y=0$ to $y=0.5$. Symmetrical initial and boundary conditions along the y-direction allows the code to effectively solve a 1-D problem.

Initially a diaphragm exists at $x=0.5$ m inside the shock tube. Conditions on the left of the diaphragm are specified to be

$$\rho_L = 1 \text{ kg/m}^3, u_L = 0 \text{ m/s}, p_L = 100,000 \text{ N/m}^2$$

At the right of the diaphragm, the tube was filled initially with gas at a lower pressure and density

$$\rho_R = 0.01 \text{ kg/m}^3, u_R = 0 \text{ m/s}, p_R = 1,000 \text{ N/m}^2$$

For the present test case, calorifically perfect gas was chosen. The simulation was started with the removal of the imaginary diaphragm. The results have been presented in figure 8.2 and figure 8.3 for time $t = 6.4 * 10^{-6}$ s. For this study, the temporal as well as the spatial order is 1. The schemes tested were Steger Warming, Roe's Scheme and BGK

scheme.

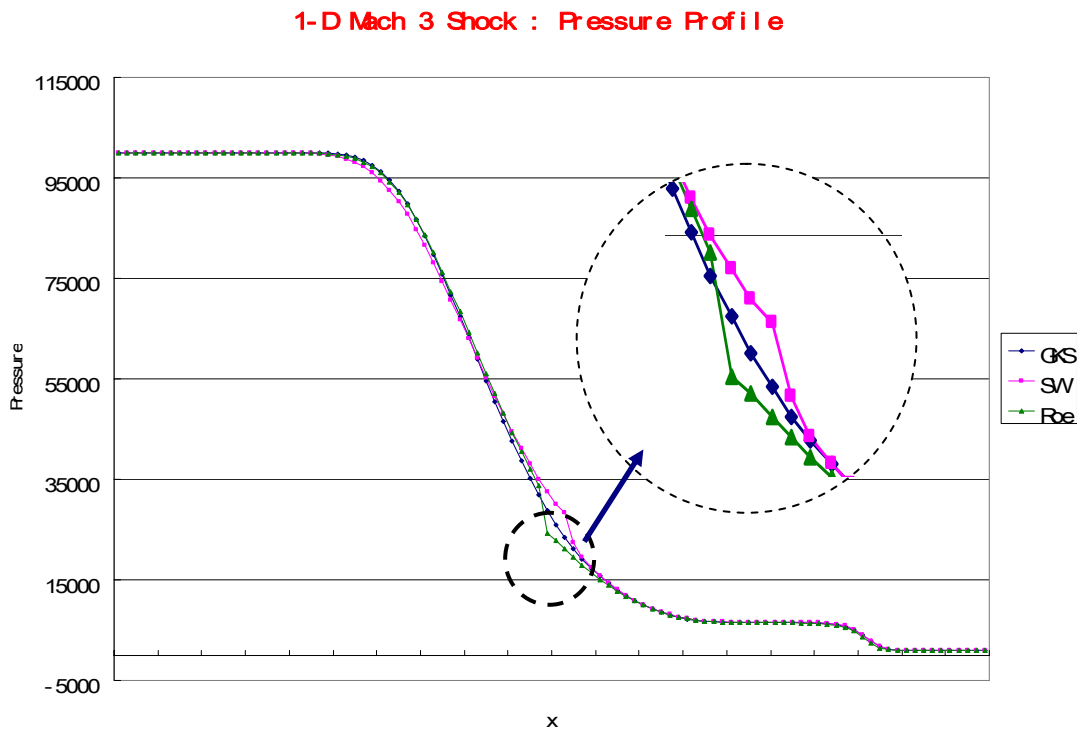


Fig 8.2 Pressure profiles along the shock tube

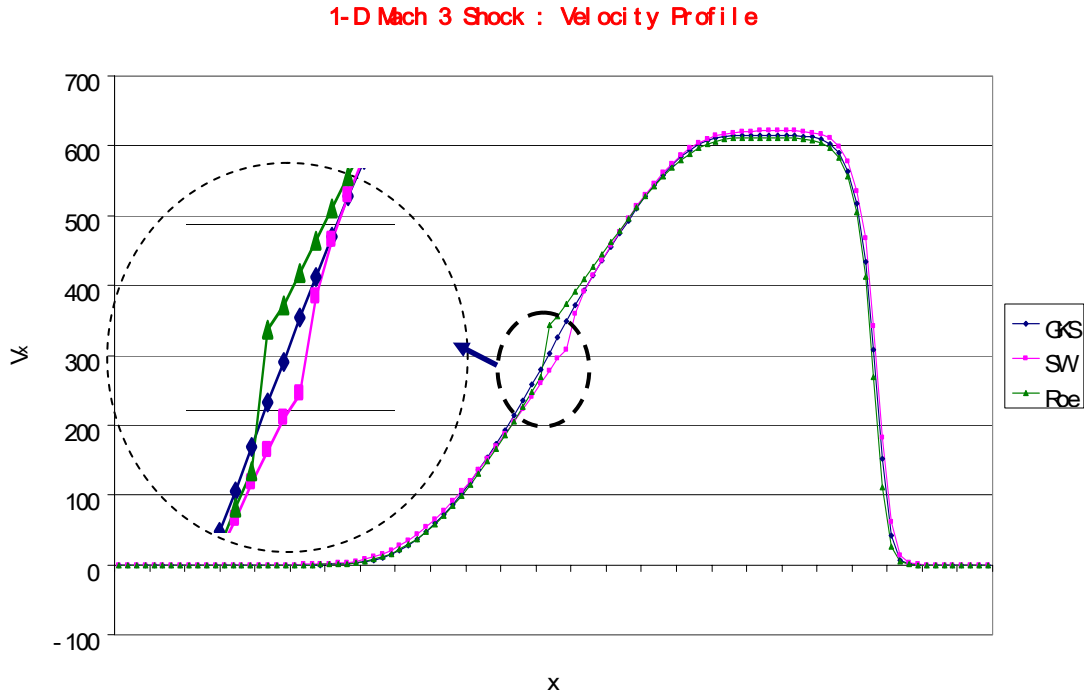


Fig 8.3 Velocity profiles along the shock tube

From the results, it is evident that the Steger-Warming and Roe's schemes do not give smooth shock profile and suffer from kinks in the solution. The Gas Kinetic or BGK method on the other hand does not produce in any such kinks. The reason for superior results from BGK scheme can be attributed to the difference in construction of these three schemes. The Steger-Warming and Roe's scheme belong to the class of Wave based approaches. In such an approach, both fluxes as well as waves are modeled, specially the interaction between the various families of waves. For Euler equations, the wave speeds are found to be

$$\lambda^i = \{\lambda_1^i \ \lambda_2^i \ \lambda_3^i \ \lambda_4^i\} = \{u-a \ u \ u \ u+a\}$$

where i is the index of the cell. We can have situations where the wave velocities on the neighboring cells have different directions. There are two possibilities:

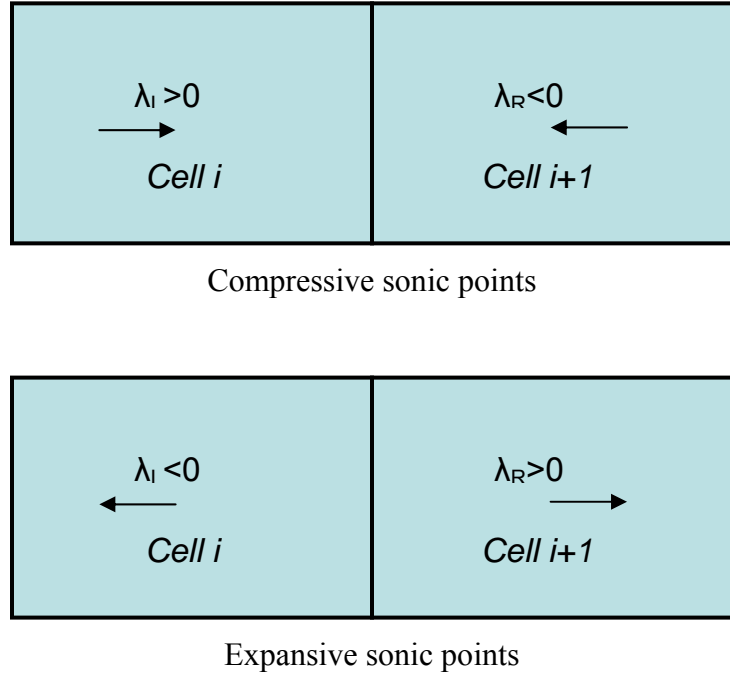


Fig 8.4 Compressive and expansive sonic points

The expansive shock shown in figure 8.4 is not physically present since it violates the entropy condition [69]. However, numerical solvers are approximations of the exact solutions and are solved for finite dx and dt . They can permit such unphysical phenomenon in the solution. Therefore, both Steger Warming and Roe's schemes allow expansion shocks in the solution and give rise to the unphysical kinks shown in the solution.

To order to avoid such spurious phenomenon in the solution, the entropy fix methods are applied to modify these schemes. The basic idea behind such a fix is to increase the artificial viscosity in regions where expansion shocks can occur. Therefore, the expansion shock gets smeared and is no longer strong enough to have an effect on the final solution. However, such fixes can be highly grid dependent. Also, incorrect

solutions can be easily overlooked until they are compared with data from experiments or from more accurate simulation results.

The BGK method, on the other hand, does not suffer from expansion shocks. The approach here is not wave-based but Boltzmann Equation-based. It has already been shown that the Boltzmann equation with BGK collision model satisfies the entropy condition. Therefore, we do not observe any kinks for the BGK scheme.

8.3 Viscous Flow over Flat Plate: BGK Scheme

In this section, the results from supersonic viscous flow over a flat plate are presented. The Crocco-Busemann relationship [78] was verified and the results were also compared with the exact numerical laminar-flow computations by van Driest [79]. For his computations, van Driest used the Crocco method [79] to solve the simultaneous differential equations of momentum and energy involved in such flows. Prandtl number for the flow is 0.71 and Sutherland law for viscosity was used to take into account the variation with respect to temperature.

The fluid medium was taken to be air. The inflow Mach number was taken to be 3.0 with a free stream temperature of 300 K and density of 1.19 kg/m^3 . The wall was assumed to be adiabatic.

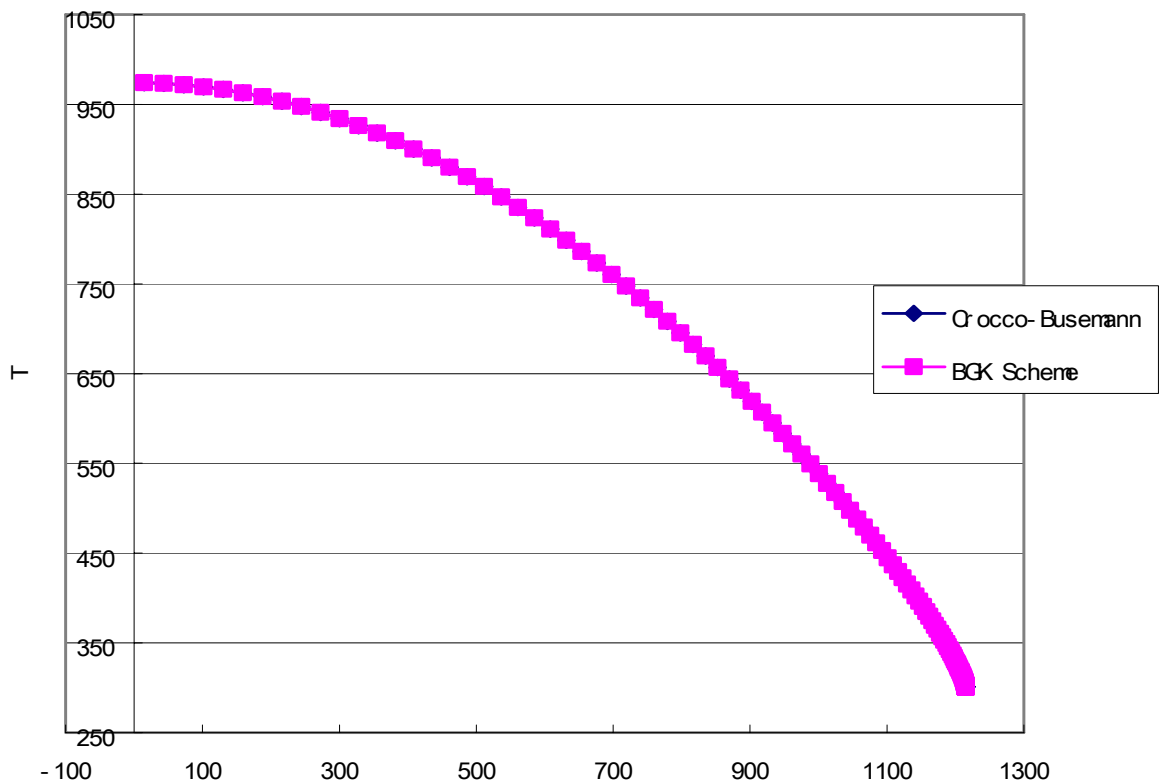


Fig. 8.5 Verification of the Crocco-Busemann relationship

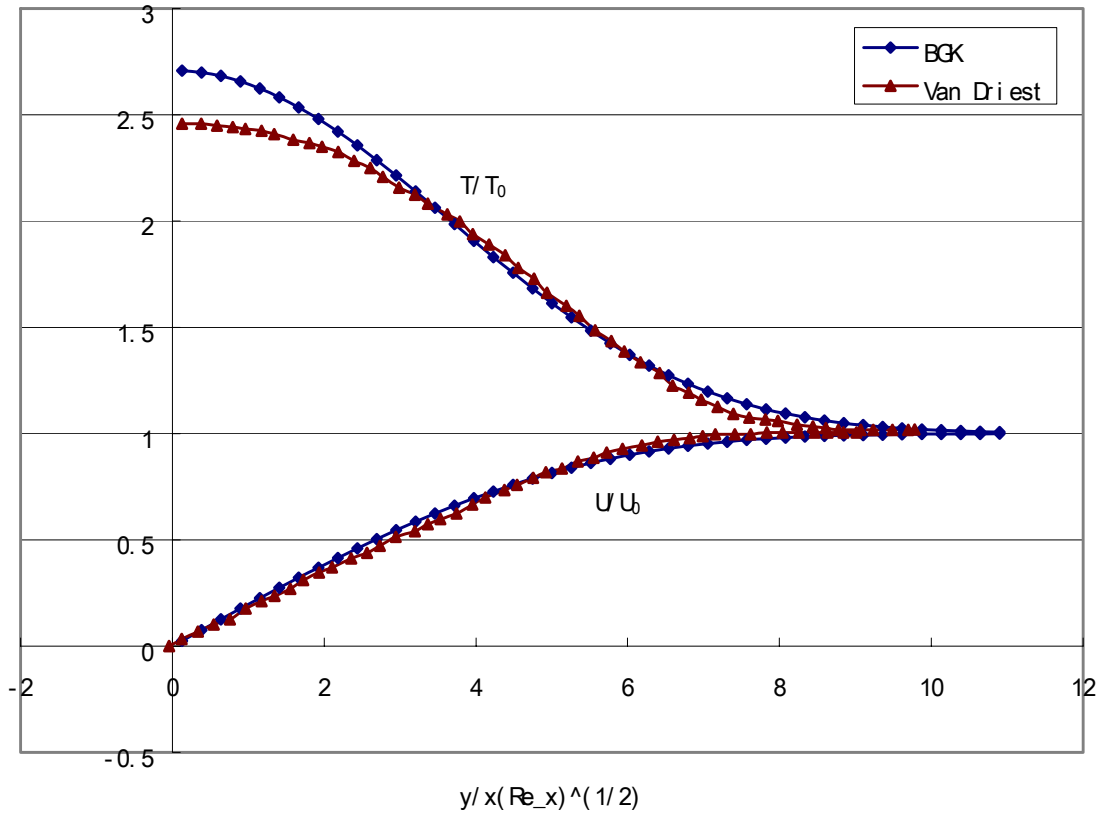


Fig 8.6 Van Driest profile using BGK scheme.

Although the results agree well with the Crocco-Busemann curve (figure. 8.5), there is some error for temperature when comparing with the Van Driest profile as seen in figure. 8.6. The maximum error occurs at the origin and is smaller than 7 %. Since the methods used by Van Driest is very different from the one used in the present case, some error can be expected. Although 7 % error is not very big, it can be further reduced by making the current approach more similar to approach used by Van Driest in terms of calculation of viscosity and heat transfer coefficient. However such an attempt resulted in affecting the stability of the BGK solver and further analysis would be required in order to reduce this error.

8.4 Reconstruction Schemes: Green Gauss and MUSCL Scheme

As discussed in Chapter VI, accuracy of the Finite Volume schemes can be increased to higher orders using reconstruction schemes. In this study, the two popular approaches, namely Green Gauss Reconstruction and MUSCL scheme are investigated and compared using Steger-Warming scheme.

Inviscid flow of N_2 past a flat ended cylinder of nose radius 1.0, placed in a hypersonic uniform stream, is considered. The stream is assumed to be in thermal nonequilibrium. A description of computational mesh along with the freestream conditions is tabulated in the figure 8.7:

Gas	M_∞	$T_\infty(K)$	$p_\infty(Pa)$
Nitrogen	6.5	300	50

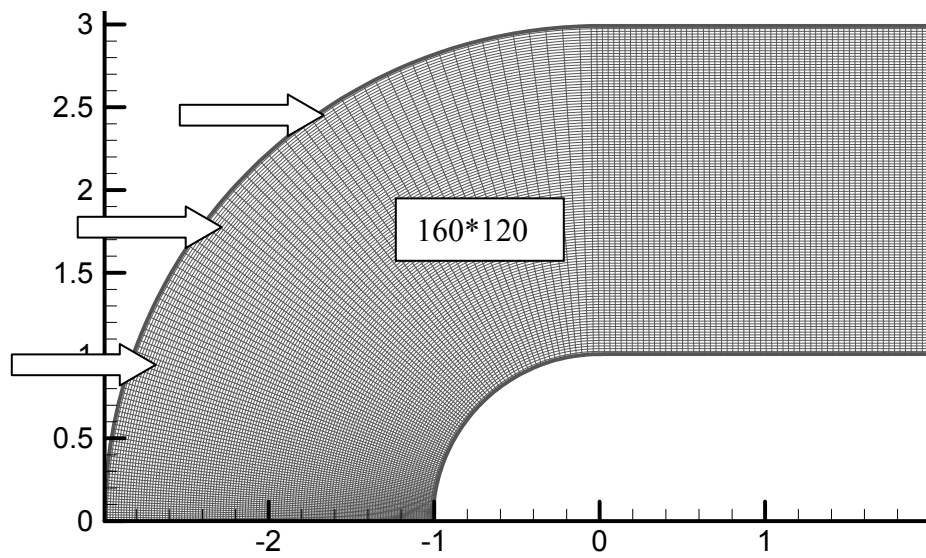


Fig 8.7 Computational mesh for the blunt body problem

The reasons for choosing to study a blunt body problem are:

- (a) Since the nose of hypersonic vehicles has a blunt shape, the results from a blunt body flow provides us with a preliminary picture of actual flight cases.
- (b) The bow shock obtained is not attached to the body and thus the effects of shock boundary layer interaction need not be considered.

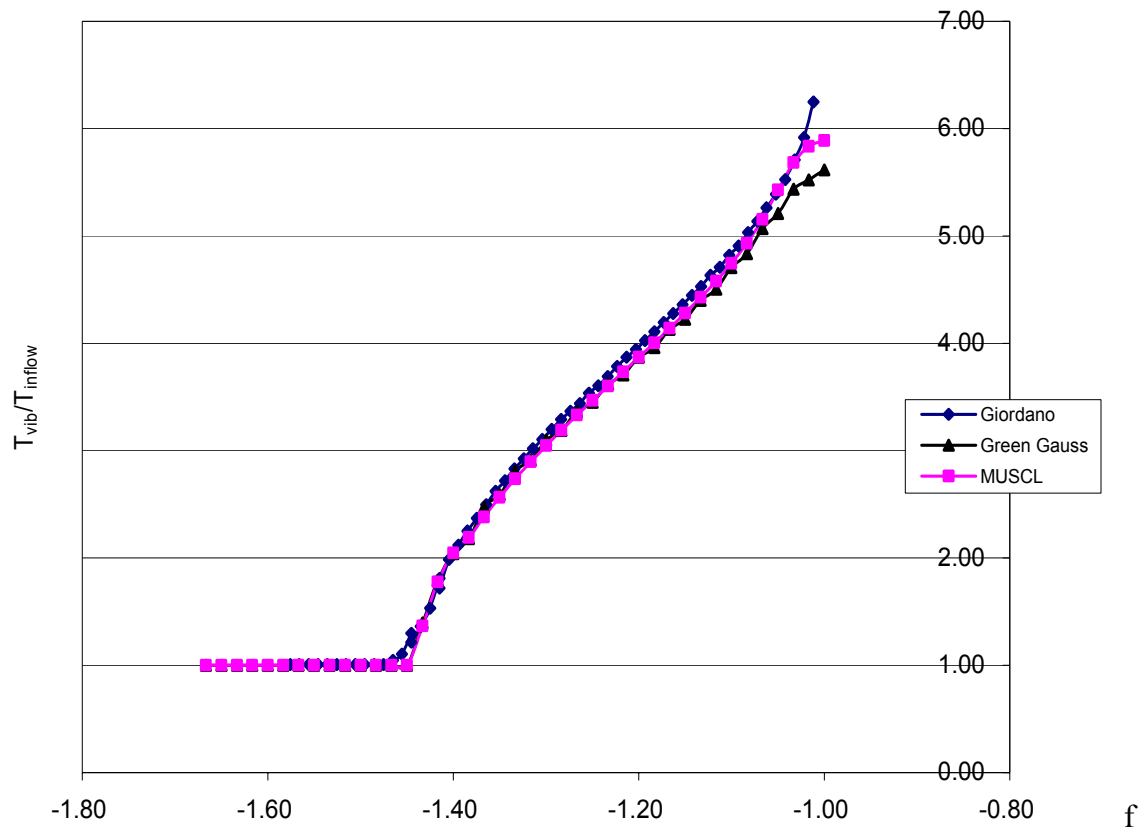
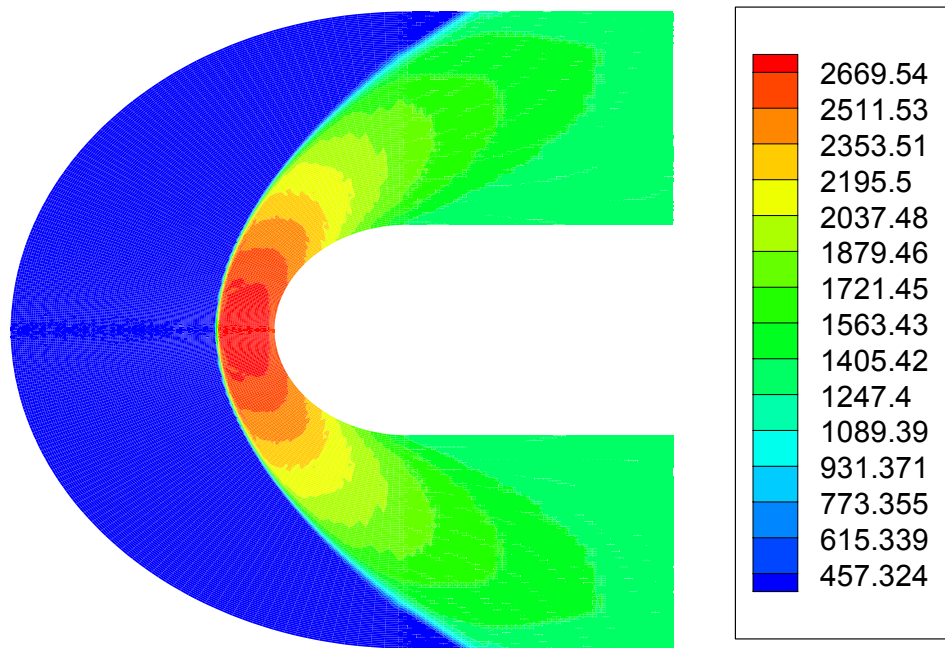


Fig 8.8 Normalized temperature profiles along stagnation line



Translational Temperature (K) Contour (Green Gauss Reconstruction)

Fig 8.9 Contour plot for the translational temperature using Green Gauss scheme

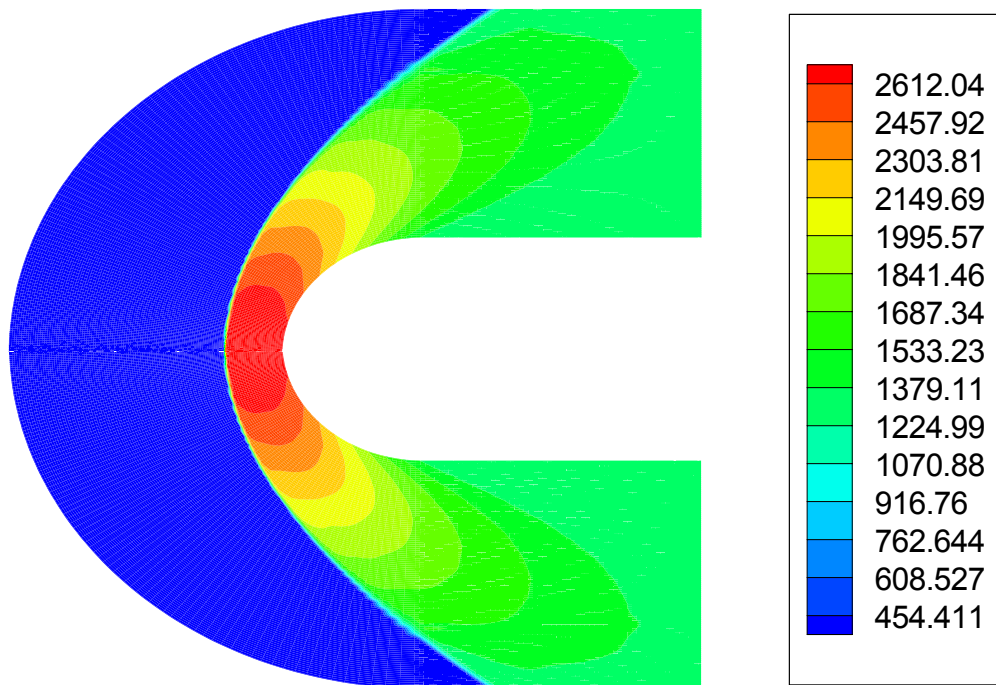


Fig 8.10 Contour plot for the translational temperature using MUSCL scheme

From the results (figures 8.8, 8.9 and 8.10), it is concluded that the MUSCL scheme is superior compared to the Green Gauss reconstruction scheme. The profile for vibrational temperature obtained using the Green Gauss method is underpredicted and suffers from oscillations. Similar oscillations are also observed in the contour plot for translational temperature.

The Green Gauss reconstruction scheme, by virtue of its construction, is supposed to provide superior results compared to the MUSCL scheme for non-orthogonal grids. Therefore the former approach is more popular for unstructured grid solver. Since, the grid for the current problem is structured and almost orthogonal, it is expected that the results obtained would not be superior to those obtained from the MUSCL scheme. However, it was unexpected to see the results being inferior and oscillatory when compared to the MUSCL Scheme.

To find the possible reasons for the above observation, Green Gauss gradient calculation has to be given a closer look. For a cell with N sides, the gradient is defined as

$$\nabla u d\Omega = \sum_i^N u_i \vec{n}_i dS_i$$

Therefore, the calculation of gradient uses information from all of the surrounding neighbors. The reconstructed values therefore, have contribution from all the neighbors. Hence the flux being calculated is influenced by cells in upstream as well as downstream of the flow. Since in a supersonic flow the information travels only in one direction, the use of Green Gauss scheme affects the upwinding of the Steger Warming scheme and causes numerical oscillations in the solution. The MUSCL scheme, on the other hand, uses one-sided information for the construction of gradients and thus maintains the

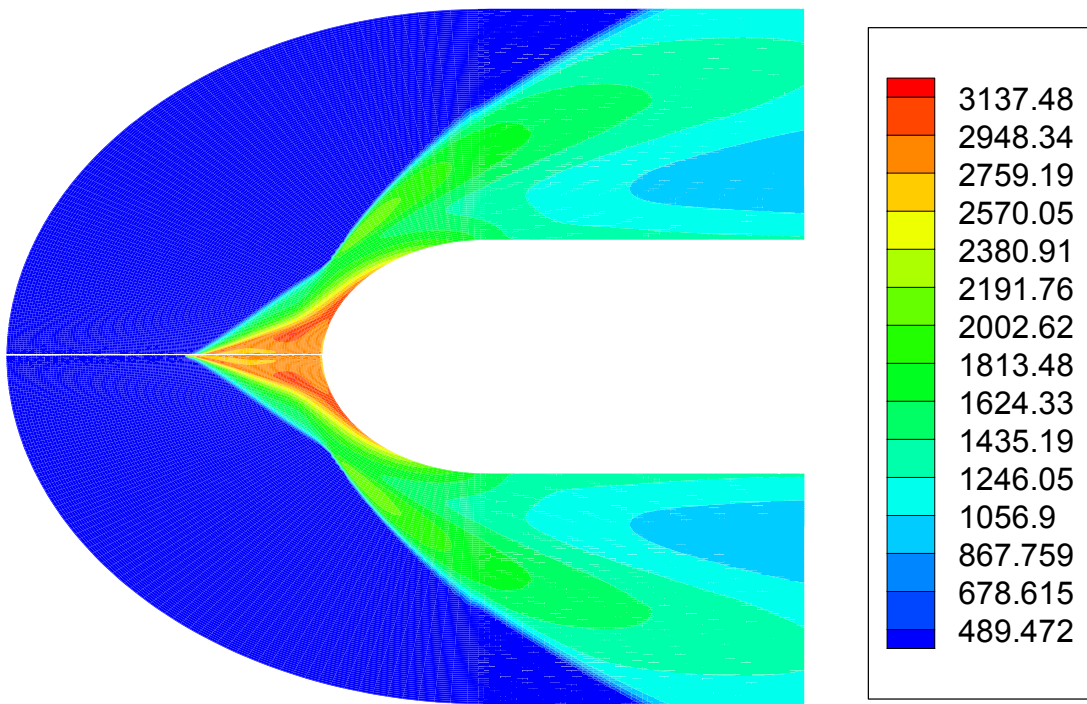
upwinding nature of the scheme. Therefore, in solving high Mach number flows on structured meshes, MUSCL scheme has clear advantages.

8.5 Nonequilibrium Hypersonic Flow over Blunt Body

In this section, the performances of the continuum based schemes (Steger Warming and Roe's scheme) and the Boltzmann based schemes (BGK scheme) are compared for hypersonic nonequilibrium flows. The test case used for this purpose is the blunt body problem. The reasons for selecting such a test case were discussed in previous section. The test case also provides the opportunity to test the BGK scheme for any possible failure because of the carbuncle phenomenon (described later in the section).

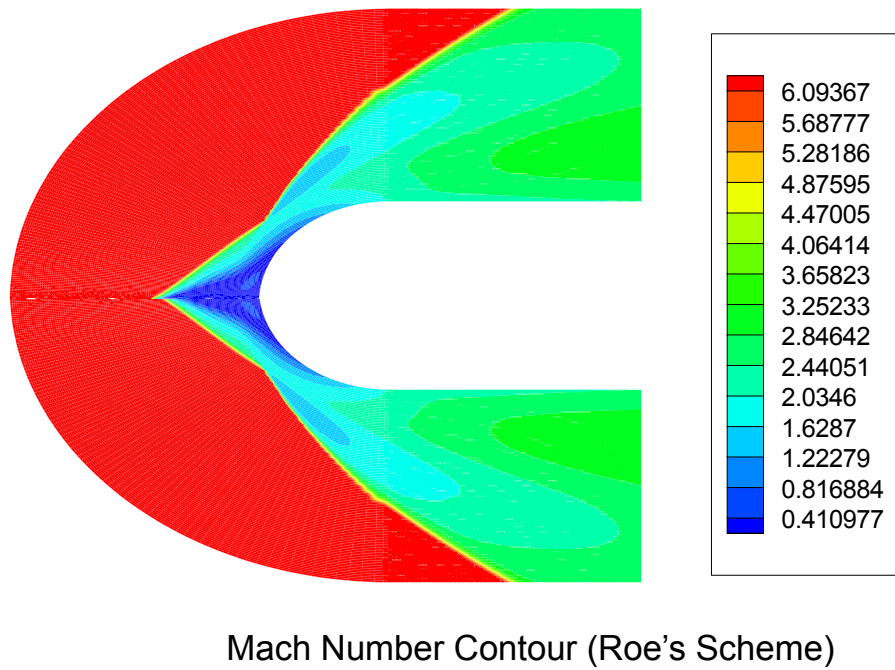
The grid and flow details are exactly the same as previous test case. The initial condition in the domain is assumed to be the same as the free stream condition. The flux is calculated using Steger Warming, Roe's Scheme and BGK scheme. Second order accuracy is obtained using the MUSCL scheme along with the Minmod limiter. Iterations are carried out until steady state is reached. The vibrational nonequilibrium physics is modeled using the Landau Teller method. The expression for the vibrational relaxation time proposed by Millikan and White [19] is used. The specific heat ratio is varied with temperature using the relation:

$$\gamma = \frac{(7/2)RT + e_{vib}}{(5/2)RT + e_{vib}}$$



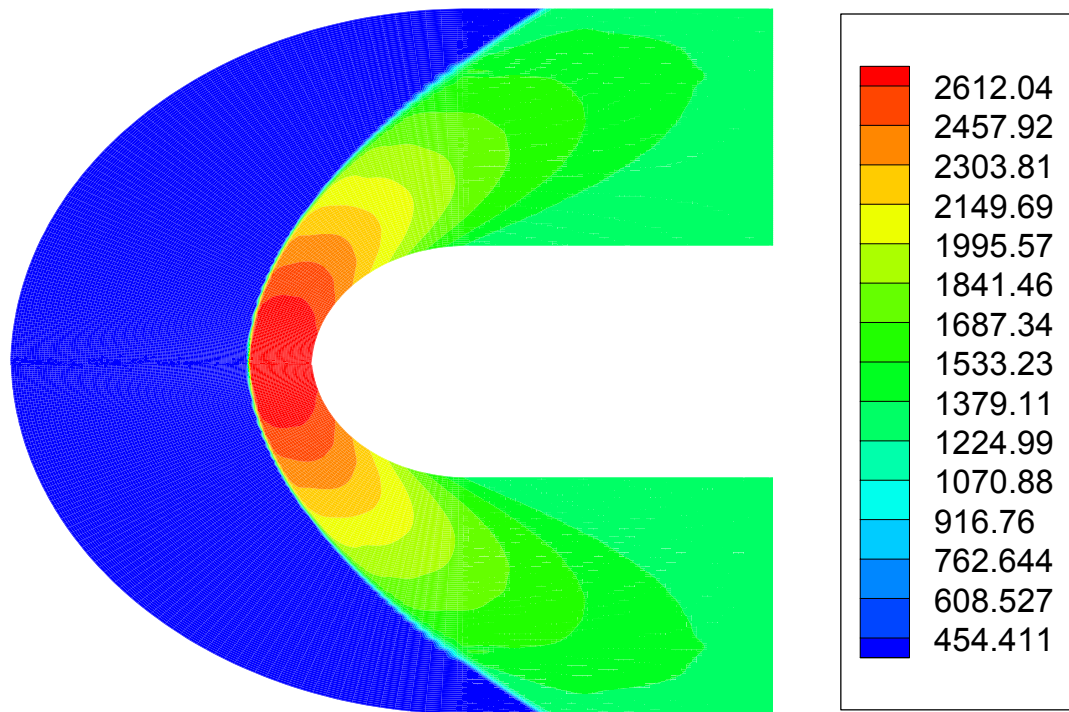
Translational Temperature (K) Contour (Roe's Scheme)

Fig 8.11 Contour plot for the translational temperature using Roe's scheme



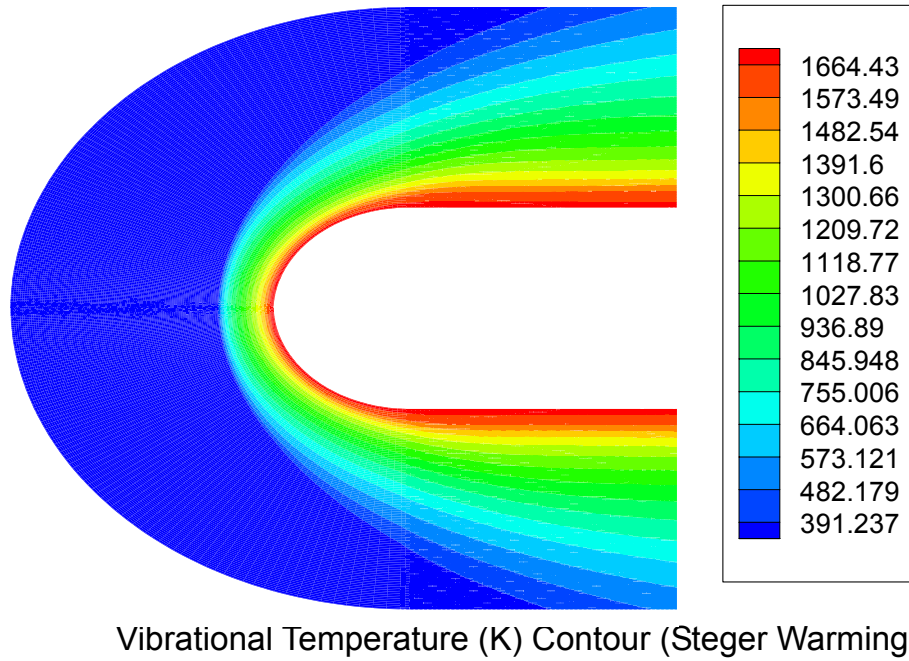
Mach Number Contour (Roe's Scheme)

Fig 8.12 Contour plot for the Mach number using Roe's scheme



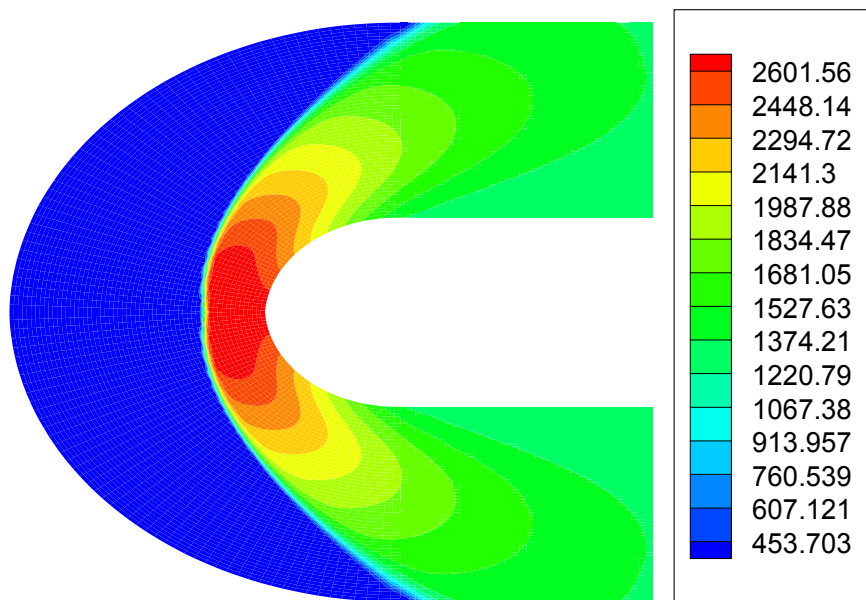
Translational Temperature (K) Contour (Steger Warming)

Fig 8.13 Contour plot for the translational temperature using Steger Warming



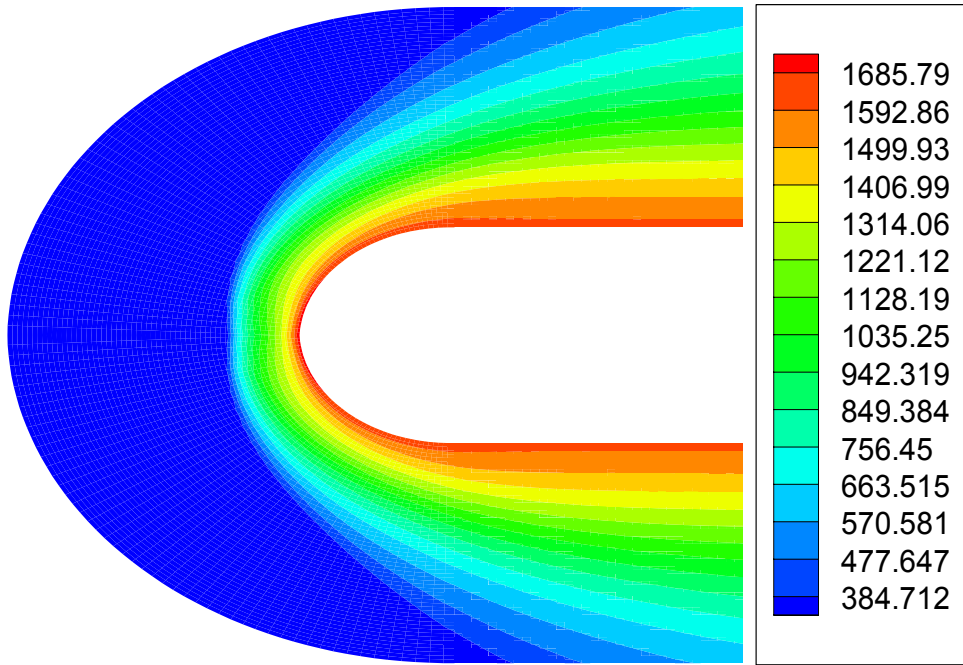
Vibrational Temperature (K) Contour (Steger Warming)

Fig 8.14 Contour plot for the vibrational temperature using Steger Warming



Translational Temperature (K) Contour (BGK Scheme)

Fig 8.15 Contour plot for the translational temperature using BGK's scheme



Vibrational Temperature (K) Contour (BGK Scheme)

Fig 8.16 Contour plot for the vibrational temperature using BGK's scheme

From the contour plots in figures 8.11 and 8.12, it can be clearly seen that the expected bow shape of the shock is not retrieved using Roe's scheme. Thus Roe's scheme fails to produce correct results for the blunt body flow. The phenomenon observed in the plot is called the carbuncle solution. By definition, the carbuncle solution is characterized by a stable solution that includes a recirculating pointed region ahead of the stagnation point. The phenomenon was first reported in 1988 by Peery and Imlay [80]. The onset of such a solution is thought to be associated with an unfavorable coupling between the normal and transverse directions across the shock wave. In order to get rid of such spurious solutions, entropy fixes are applied. As pointed out in the previous section, such fixes increase the artificial dissipation in order to smear the expansion shocks.

However as seen in figures 8.13 and 8.14, the Steger-Warming scheme, which belongs to the Flux Vector Splitting (FVS) family, does not suffer from the carbuncle phenomenon. One of the main reasons is that FVS schemes, due to their dissipative nature, dampen the transverse perturbations in the planar shock problem. It should be noted that the scheme is able to capture the bow shock correctly, even though the solution for 1-D shock tube problem suffered from kinks. This is because solutions which look physically correct can be obtained even if entropy condition is violated. Therefore for the present case, results besides the contour plots are needed to ensure the reliability of these results.

From figures 8.15 and 8.16 it can be said that the BGK scheme is able to capture the bow shock accurately, and the contour plots also appear admissible. Comparing to the shock profile obtained from Steger Warming scheme, it is observed that BGK produces similar profiles close to the stagnation line. However as we move away from the line of symmetry, slight perturbations can be seen in the profile obtained from the Steger Warming scheme. These perturbations can be attributed to the loss of shock-grid alignment as one move away from the center line. Surprisingly, the BGK scheme was not affected by this misalignment. Although, the most probable cause seems to be the excessive dissipation of Steger Warming scheme, it is difficult to point out the exact mechanism for the cause.

The vibrational temperature contour plots (figure 8.14 and figure 8.16) for both the BGK and the Steger Warming appear to be physically correct. From the contour plots, the mechanism for the onset of vibrational nonequilibrium in the flow can be studied. Downstream of the bow shock, there is a sudden rise in the translational temperature, which can be attributed to the abrupt rise in pressure (which in turn can be attributed to the sudden compression of the flow). However, there is no such mechanism available for the vibrational temperature to change abruptly. Since the translational and vibrational

temperatures are no longer equal, the source term in the vibrational temperature gets activated.

$$\frac{de_v}{dt} = \frac{e_v^{eq}(T_{tr}) - e_v(T_{vib})}{\tau}$$

Since the source term is positive, it contributes to an increase in vibrational energy and thus the vibrational temperature. It should be noted that the source term is not large enough to produce a sudden jump in the vibrational energy across the shock.

The variation of the two temperatures along the stagnation line is shown in figure 8.17. The stagnation line is along the x-axis from $x = -3$ to $x = -1$. Comparisons are made against Giordano et al.[81], who uses a finite volume central difference scheme. The dissipation is provided using an adaptive dissipation model which in turn uses a blend of second and fourth order differences. Landau Teller model is used to account for vibrational energy.

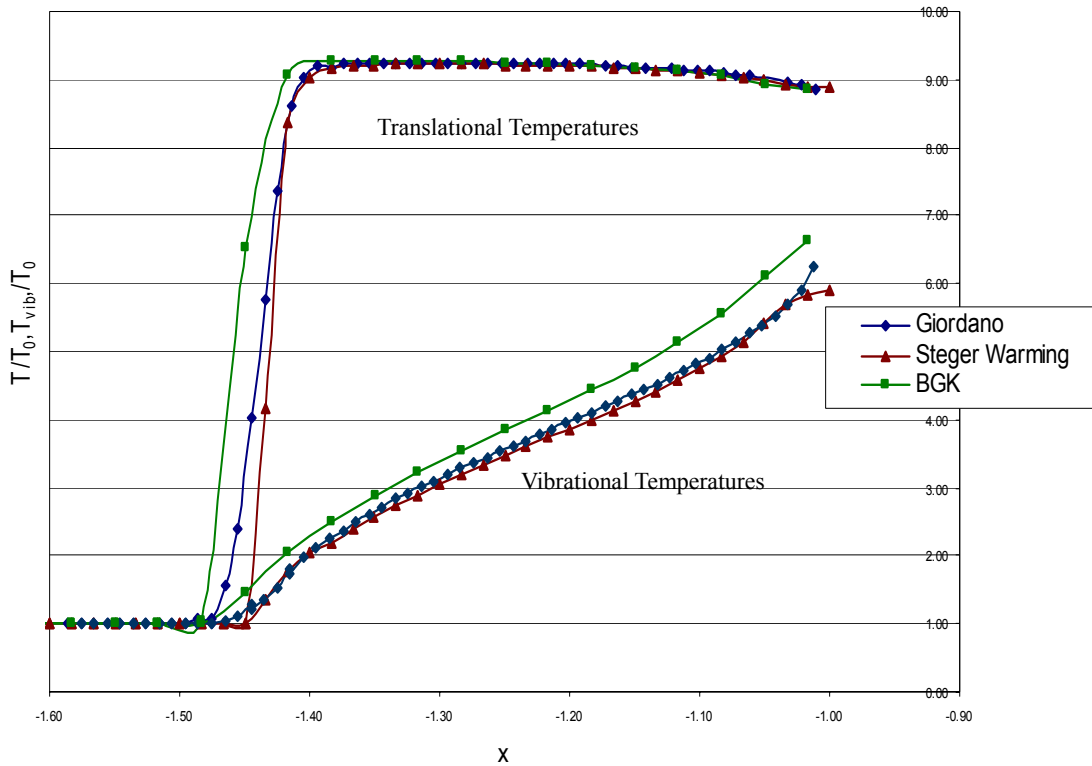


Fig 8.17 Normalized temperature profiles along stagnation line

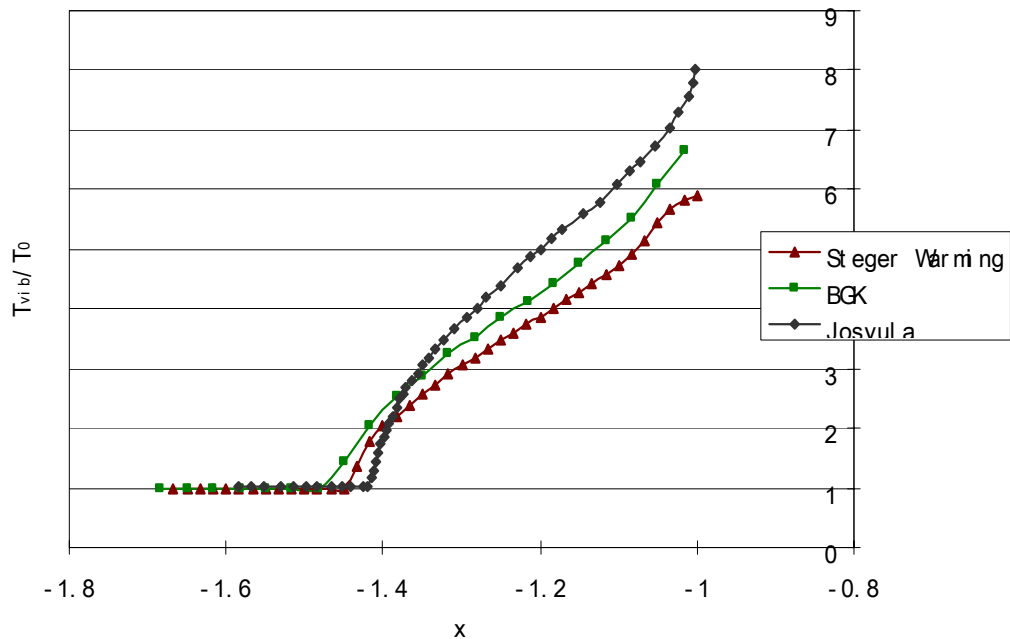


Fig 8.18 Normalized vibrational temperature profiles a long stagnation line

As can be seen in figure 8.17, the temperature profile is almost identical for Giordano, Steger Warming and BGK scheme. The shock standoff positions obtained are different for all the three cases. However the error in shock position is still less than 2 %. Such small differences can be expected when different schemes are used for a shock simulation. There is a small dip in the temperature profile just ahead of the shock in case of BGK scheme. The cause for this numerical oscillation will be discussed in a later section.

In the vibrational temperature profile (figure 8.17), it can be observed that the profile obtained from Steger Warming scheme is closer to the one obtained by Giordano et. al. However both SW and Giordano results are far from the more accurate results obtained by Josyula[9] for the same test case. In his computation, Josyula uses the Multiquantum transition (MQT) approach to account for the vibrational nonequilibrium. It has been discussed in previous chapter that the MQT approach is an almost exact calculation to account for vibrational nonequilibrium and thus the predictions can be expected to be much closer to real flows. Therefore, a more informative comparison would be the one shown in figure 8.18, where the vibrational temperature profiles are compared with the profile obtained by Josyula.

From figure 8.16, it can be concluded that when compared to results obtained by Josyula, at the stagnation point the Steger Warming scheme underpredicts the vibrational temperature by 27.5 %, whereas the BGK scheme underpredicts by 16.2 %. Since the Landau Teller model has been used by both Steger Warming and BGK schemes, some errors are expected. However BGK scheme does show an improvement of almost 11 % when compared to Steger Warming scheme.

The Steger Warming scheme shows yet another discrepancy for the vibrational temperature profile at $x = -1.0$. The profile almost becomes parallel to the x-axis at this point. This implies that the vibrational temperature obtained by SW becomes constant

very near to the stagnation point. This is not the case with the results obtained by Josyula [9], where vibrational temperature keeps increasing even at the stagnation point. The reason for this drop is again the high inherent dissipation present in the Steger Warming scheme. The BGK scheme, on the other hand, does not show such a drop in slope and thus once again outperforms the Steger Warming scheme.

CHAPTER IX

CONCLUSIONS AND SCOPE FOR FUTURE WORK

9.1 Conclusions

After a detailed literature survey and observations from the numerical results obtained for various test cases, the following conclusions have been made.

- (a) To account for vibrational nonequilibrium the Multiquantum transition or vibrational kinetics method is the more accurate compared to Landau Teller model and Ruffin's model. However, due to its high computational demands, the Landau Teller(L-T) model is more popular because of its simplicity and ease of implementation. The L-T model is especially more popular for blunt body problems. This is because for flow over blunt body undergoes compression. For such a case the V-T transfer dominates all the vibrational energy levels. Hence even though the L-T model takes into account only the V-T transfer (neglecting the V-V-T transfer), reasonable predictions can be expected from it.
- (b) To take into account another effect of nonequilibrium: on the chemical reaction rate constants, the main approaches found in literature are those based on physiochemical models and on semi empirical models. The most popular model used currently is the Park's two temperature model, which is simple and easy to implement in CFD codes.
- (c) As in chemical models, two approaches can be used to model transport coefficient: kinetic theory and curve fit based models. It was found that the curve fit models are preferred for hypersonic flow simulations.
- (d) From the results of shock tube problem, it can be concluded that the Boltzmann BGK method has a clear advantage over the continuum based Steger Warming and Roe's

schemes. The Steger Warming scheme, belonging to the Flux Vector Splitting class, and Roe's scheme, belonging to the Flux Difference Splitting class, may allow entropy violating solutions and is the reason for the inaccurate results obtained. The Boltzmann BGK always satisfies the entropy condition and hence accurately captures the shock.

(e) The Green Gauss reconstruction scheme performs poorly when compared to MUSCL scheme when used to simulate vibrational nonequilibrium flow. It was found that the Green Gauss scheme affects the upwinding of the scheme and thus results in oscillations in the solution.

(f) The Boltzmann BGK scheme outperforms in Steger Warming schemes and Roe's schemes for the case of nonequilibrium flow over a blunt body. The Roe's scheme completely fails since it allows for expansion shocks in the solution. The Steger Warming scheme, on the other hand produces poorer results due to excessive dissipation. Although these failings can be avoided by using entropy fixes, such fixes tend to be highly grid dependent. Since the hypersonic aircrafts have a blunt shape for the nose, the Boltzmann BGK scheme seems to be a better option for simulating actual flight cases.

9.2 Scope for Future Work

- (a) The Multiquantum transition model to account for vibrational nonequilibrium can be implemented so that the code can be used to solve expanding flows as well.
- (b) The chemical nonequilibrium effects can be added by implementing the Park's two temperature model.
- (c) The relation for relaxation time in the BGK model was derived assuming the nonequilibrium distribution to be a first order expansion around the equilibrium distribution. However a modified relaxation time can be implemented using a higher order expansion for the nonequilibrium distribution function. This would enable the code to be applicable to higher Knudsen number flows.

(d) The turbulence effects can be included using a one equation Spalart Allmaras model.

REFERENCES

- [1] Anderson JD Jr. *Hypersonic and High Temperature Gas Dynamics*. McGraw-Hill; New York, 1989.
- [2] Napolitano LG. Belotserkovski OM. *Computational Gasdynamics*. CISM Courses and Lectures n. 40; New York, 1975.
- [3] Park C. *Nonequilibrium Hypersonic Aero Thermodynamics*. John Wiley and Sons: New York, 1990.
- [4] Ivanov MS, Gimelshein SF. Computational Hypersonic Rarefied Flows. *Annu. Rev. Fluid Mech.* 1998; 30:469–505.
- [5] Leonardo CS, Boyd ID. *Development of an Unstructured Navier-Stokes Solver for Hypersonic Nonequilibrium Aerothermodynamics*. 38th AIAA Thermophysics Conference, Toronto, Canada, 6-9 June 2005.
- [6] Schwartzenruber TE, Boyd ID. *Detailed Analysis of a Hybrid CFD-DSMC Method for Hypersonic Non-Equilibrium Flows*. 38th AIAA Thermophysics Conference, Toronto, Ontario Canada, 6-9 June 2005.
- [7] Josyula E, Bailey WF. *Multiquantum Vibrational Energy Exchanges in Nonequilibrium Hypersonic Flows*. 38th AIAA Thermophysics Conference, Toronto, Ontario Canada, 6-9 June 2005.
- [8] Josyula E, Bailey WF., *Nonequilibrium Relaxation in High Speed Flows*. 37th AIAA Thermophysics Conference, Portland, Oregon, 28 June-1 July 2004.
- [9] Josyula E. Computational Study of Vibrationally Relaxing Gas Past Blunt Body in Hypersonic Flows, *Journal of Thermophysics and Heat Transfers*, vol. **14**, 2000; pp. 18-26.
- [10] Adamovich IV, Rich JW. Three-dimensional nonperturbative analytic model of vibrational energy transfer in atom–molecule collisions. *The Journal of Chemical Physics*, vol. **109**, Issue 18, November 8, 1998, pp.7711-7724.

- [11] Herzfeld KF, Litovitz TA. *Absorption and Dispersion of Ultrasonic Waves*. Academic Press.: New York, 1959.
- [12] Rapp D, Sharp TE. Vibrational Energy Transfer in Molecular Collisions Involving Large Transition Probabilities. *J. Chem. Phys*, vol. **38**, 1963; pp 2641.
- [13] Rapp D, Golden PE. Resonant and Near Resonant Vibrational—Vibrational Energy Transfer between Molecules in Collisions, *J. Chem. Phys*. vol. **40**, 1964; pp 3120 .
- [14] Sharma RD, Brau CA. Energy Transfer in Near-Resonant Molecular Collisions due to Long-Range Forces, *J. Chem. Phys*, vol. **50**, 1969; pp 924-930.
- [15] Kerner EH, Note on The Forced and Damped Oscillator in Quantum Mechanics, *Can. J. Phys*, vol. **36**, 1958.: pp 371.
- [16] Treanor CE. Vibrational Energy Transfer in High Energy Collisions, *J. Chem. Phys*, vol. **43**, 1965; pp 532.
- [17] Zelechow A, Rapp D, Sharp TE. Vibrational-Vibrational Translational Energy Transfer Between Two Diatomic Molecules, *J. Chem. Phys*, vol. **49**, 1968; pp 286.
- [18] Kelley JD, Vibrational Energy Transfer Processes in Collisions between Diatomic Molecules, *J. Chem. Phys*. **56**, 1972; pp 6108.
- [19] Millikan RC, White DR. Systematics of Vibrational Relaxation, *J. of Chem. Phys.*, vol. **39**, 1963; pp. 3209–3213.
- [20] Gupta RN, Yos JM, Thompson RA. *A Review of Reaction Rates and Thermodynamic and Transport Properties for the 11 Species Air Model for Chemical and Thermal Nonequilibrium Calculations to 30000 K*, NASA TM-101528, 1989.
- [21] Hammerling P, Teare JD, Kivel B. Theory of Radiation from Luminous Shock Waves in Nitrogen, *Physics of Fluids*, vol. **2**, no. (4), 1959; pp. 422–426.
- [22] Treanor CE, Marrone PV. Effects of Dissociation on the Rate of Vibrational Relaxation, *Physics of Fluids*, vol. **5**, no. (9), 1962; pp. 1022–1026.

- [23] Marrone PV, Treanor CE. Chemical Relaxation with Preferential Dissociation from Excited Vibrational Levels, *Physics of Fluids*, vol. **6**, no. (9), 1963; pp. 1215–1221.
- [24] Josyula E, Bailey WF, Xu K. *Nonequilibrium Relaxation in High Speed Flows*, 37th AIAA Thermophysics Conference, Portland, Oregon, 28 June - 1 July 2004.
- [25] Knab O, Fruhauf HH, Messerschmid EW. Theory and Validation of the Physically Consistent Coupled Vibration-Chemistry-Vibration Model, *Journal of Thermophysics and Heat Transfer*, vol. **9**, no. (2), 1995; pp. 219–226.
- [26] Curtiss C, Hirschfelder JO. Transport Properties of Multicomponent Gas Mixtures, *J. Chem. Phys.*, vol. **17**, no. (6), 1949; p. 550-555.
- [27] Hirschfelder JO, Curtiss CF, Bird RB. *Molecular Theory of Gases and Liquids*, John Wiley and Sons, New York, 1954.
- [28] Hirschfelder JO. Heat Conductivity in Polyatomic or Electronically Excited Gases II., *J. Chem Phys.*, vol. **26**, no. (2), 1957; pp. 282-285.
- [29] Wilke CR. A Viscosity Equation for Gas Mixtures, *J. Chem. Phys.*, vol. **18**, no.(4) , 1950; p. 517-519.
- [30] Mason E, Saxena S. Approximate Formula for the Thermal Conductivity of Gas Mixtures, *Physics of Fluids*, vol. **1**, no. (5), 1958; pp. 361-369.
- [31] Hanson C. *Approximations for the Thermodynamic and Transport Properties of High-Temperature Air*; NASA TR-50, 1960.
- [32] Viegas J, Howe J. *Thermodynamic and Transport Property Correlation Formulas for Equilibrium Air from 1,000 K to 15,000 K*, NASA TN D-1429, 1962.
- [33] Blottner F. *Chemically Reacting Viscous Flow Program for Multi-Component Gas Mixtures*, Sandia Labs Report SCRR-70-754, 1971.
- [34] Candler G. The Computation of Weakly Ionized Hypersonic Flows in Thermo-Chemical Nonequilibrium, *Journal of Thermophysics and Heat Transfer*, vol. **5**, no.(3) , 1991; pp 266-273.

- [35] Macheret SO, Rich JW. Nonequilibrium Dissociation Rates behind Strong Shock Waves. *Chemical Physics*, vol. **174**, no.(1), 1993; pp 25-43.
- [36] Macheret SO, Fridman AA, Adamovich IV, Rich JW, Treanor CE. *Mechanisms of Nonequilibrium Dissociation of Diatomic Molecules*. Joint Thermophysics and Heat Transfer Conference, 6th, Colorado Springs, Colorado, 20-23 June 1994.
- [37] Gonzales DA, Varghese P.L. Evaluation of Simple Rate Expressions for Vibration-Dissociation Coupling. *Journal of Thermophysics and Heat Transfer*, vol **8**, no.(2), 1994; pp 236-243.
- [38] Kiefer JH, Hadjuk JC. A Vibrational Bias Mechanism for Diatomic Dissociation : Induction Times and Steady Rates for O₂, H₂ and D₂ Dilute in Argon,. *J. Chem. Phys.*, vol. **38**, 1979; pp 329-340.
- [39] Sharma SP, Huo WM., Park C. Rate Parameters for Coupled Vibration-Dissociation in a Generalized SSH Approximation. *Jour. Thermo. Heat. Transf.*, vol. **6**, no.(1), 1992; pp 9-21.
- [40] Losev SA, Makarov VN, Pogosbekyan MJ, Shatalov OP. *Thermochemical Nonequilibrium Kinetic Models in Strong Shock Waves in Air*. Joint Thermophysics and Heat Transfer Conference, 6th, Colorado Springs, Colorado, 20-23 June 1994.
- [41] Park C. *Assessment of a Two-Temperature Kinetic Model for Dissociating and Weakly Ionizing Nitrogen*. AIAA and ASME, Joint Thermophysics and Heat Transfer Conference, 4th, Boston, Massachusetts, June 2-4, 1986.
- [42] Palmer G. *An Assessment of Transport Property Methodologies for Hypersonic Flows*, AIAA, Aerospace Sciences Meeting & Exhibit, 35th, Reno, Nevada, Jan. 6-9, 1997.
- [43] Bertin JJ, Cummings RM. Critical Hypersonic Aerothermodynamic Phenomena. *Annu. Rev. Fluid Mech.* vol. **38**, 2006; pp 129–57.
- [44] Kim KH, Kim C, Rho OH. Methods for the Accurate Computations of Hypersonic

- Flows: AUSMPW+ scheme. *J. Comput. Phys.*, vol. **174**, 2001; pp 38–80.
- [45] Pirzadeh S. *Vortical Flow Prediction Using an Adaptive Unstructured Grid Method*. RTO Applied Vehicle Technology (AVT) Panel, Loen, Norway, May 2001.
- [46] Papadopoulos P, Venkatapathy E, Prabhu D, Loomis MP, Olynick D. Current Grid-generation Strategies and Future Requirements in Hypersonic Vehicle Design, Analysis, and Testing., *Appl. Math. Model.*, vol. **23**, 1999; pp 705–735.
- [47] Ait-Ali-Yahia D, Habashi WG. Finite Element Adaptive Method for Hypersonic Thermochemical Nonequilibrium Flows. *AIAA Journal*, vol. **35**, no. (8), August 1997; pp 1294.
- [48] Palmer G, Venkatapathy E. Comparison of Nonequilibrium Solution Algorithms Applied to Chemically Stiff Hypersonic Flows. *AIAA Journal*, vol. **33**, no. (7), July 1995; pp 1211-1219.
- [49] Ju Y. Lower-Upper Scheme for Chemically Reacting Flow with Finite Rate Chemistry. *AIAA Journal*, vol. **33**, no. (7), July 1995; pp 1418-1425.
- [50] Park C, Yoon S. *Fully Coupled Implicit Method for Thermochemical Nonequilibrium Air at Suborbital Flight Speeds*. AIAA Computational Fluid Dynamics Conference, 9th, Buffalo, New York; 13-15 June 1989;. pp. 440-449.
- [51] Bertolazzi E. A Finite Volume Scheme for Two Dimensional Chemically Reactive Hypersonic Flow. *International Journal of Numerical Methods for Heat & Fluid Flow*, vol. **8**, no. (8), 1998; pp 888-933.
- [52] Tsai YLP, Hsieh KC. *Comparative Study of Computational Efficiency of Two LU Schemes for Non-Equilibrium Reacting Flows*. Aerospace Sciences Meeting, 28th, Reno, Nevada, Jan 8-11, 1990.
- [53] Roe PL. Approximate Riemann Solver, Parameter Vector and Difference Schemes, *Journal of Computational Physics*, vol. **43**:1981: pp 357-372,
- [54] Harten A, Lax PD, Leer BV. On Upstream Differencing and Godunov-type

- Schemes for Hyperbolic Conservation Laws, *SIAM Rev.*, vol. **25**, 1983; pp 35-61.
- [55] Steger JL, Warming RF. Flux Vector Splitting of the Inviscid Gas Dynamics Equations with Application to Finite Difference Methods. *Journal of Computational Physics*, vol. **40**, 1981, pp 263-293.
- [56] B. Van Leer. Flux-Vector Splitting for the Euler Equations, *Lecture Notes in Physics*, 170:507-512, 1982; pp 507-512.
- [57] Liou MS, Steffen CJ. A New Flux Splitting Scheme, *Journal of Computational Physics*, vol. **107**, July 1993, pp.23-39.
- [58] Ruffin SM. *Vibrational Energy Transfer of Diatomic Gases in Hypersonic Expanding Flows*, PhD. Dissertation, SUDDR 635, Stanford Univ., Stanford, California, June 1993.
- [59] Ruffin SM. Prediction of Vibrational Relaxation in Hypersonic Expanding Flows Part I : Model Development. *Journal of Thermophysics and Heat Transfer*, vol. **9**, no. (3), 1995; p. 432.
- [60] Ruffin S M. Prediction of Vibrational Relaxation in Hypersonic Expanding Flows Part II: Results. *Journal of Thermophysics and Heat Transfer*, vol. **9**, no. (3), 1995; pp. 438.
- [61] Wang WL, Boyd ID. *Hybrid DSMC-CFD Simulations of Hypersonic Flow over Sharp and Blunted Bodies*, 36th AIAA Thermophysics Conference, Orlando Florida, June 23-26, 2003.
- [62] Anderson JD. *Computational Fluid Dynamics: The Basics with Applications*, McGraw-Hill: New York, 1995.
- [63] MacCormack RW. The Effect of Viscosity in Hypervelocity Impact Cratering, *AIAA Paper*, 1969; pp 354.
- [64] Hirsch C. The Finite Difference Method, *Numerical Computation of Internal and External Flows*, vol. **1**, chap. 4, John Wiley and Sons: Chichester, United Kingdom,

1988, pp. 167–200.

- [65] Hirsch C, Finite Volume Method and Conservative Discretizations, *Numerical Computation of Internal and External Flows*, vol. **1**, chap. 6, John Wiley and Sons: Chichester, United Kingdom, 1988, pp. 237–264.
- [66] Rizzi AW, Inouye M. Time-Split Finite-Volume Method for Three-Dimensional Blunt-Body Flow, *AIAA Journal*, vol. **11**, no. (11), Nov. 1973; pp. 1478–1485.
- [67] Hirsch C. The Finite Element Method, *Numerical Computation of Internal and External Flows*, vol. **1**, chap. 5, John Wiley and Sons: Chichester, United Kingdom, 1988, pp. 201–236.
- [68] Hirsch C. *Numerical Computation of Internal and External Flows*, John Wiley & Sons: New York 1991.
- [69] Laney CB. *Computational Gas Dynamics*. Cambridge University Press: New York 1998.
- [70] Harris S. *An Introduction to the Theory of the Boltzmann Equation*, Dover Publications: New York 1971.
- [71] Bhatnagar PL, Gross EP, Krook M. A Model for Collision Processes in Gases. *Phys. Rev.*, 1954; pp. 511.
- [72] Vincenti WG, Kruger CH. *Introduction to Physical Gas Dynamics*. John Wiley & Sons: New York 1965.
- [73] Xu K, Martinelli L, Jameson A, Gas-kinetic Finite Volume Methods, Flux-Vector Splitting, and Artificial Diffusion. *Journal of Computational Physics*, vol. **120**, no.(1), Aug. 1995; p.48-65.
- [74] Xu K. A Gas-Kinetic BGK Scheme for the Navier-Stokes Equations and Its Connection with Artificial Dissipation and Godunov Method. *Journal of Computational Physics*, vol. **171**, no (1), 20 July 200; pp. 289-335.
- [75] Godunov SK. A Difference Scheme for Numerical Computation of Discontinuous

- Solution of Hydrodynamic Equations, *Matematicheskii Sbornik*, vol. **47**, 1959; pp. 271–306 (in Russian).
- [76] Leonardo S, Boyd I. *Numerical Simulation of Weakly Ionized Hypersonic Flow for Reentry Configurations*. 9th AIAA/ASME Joint Thermophysics and Heat Transfer Conference, San Francisco, California, 5-8 June, 2005.
- [77] Choi H, Liu JG. The Reconstruction of Upwind Fluxes for Conservation Laws: Its Behavior in Dynamics and Steady State Calculations, *Journal of Computational Physics*, vol. **144**, no. (2), Aug. 1998; pp. 237–256.
- [78] White FM. *Viscous Fluid Flow*. McGraw Hill: New York 2005.
- [79] Van Driest R. *Investigation of Laminar Boundary Layer and Compressible Fluids Using the Crocco. Method*. Technical Note. TN. 2597, NACA, January. 1952.
- [80] Peery KM , Imlay ST. Blunt Body Flow Simulations, *AIAA Paper* 1988; pp 2924.
- [81] Belluci GD, Colonna V, Capitelli G, Armenise MI, Bruno C. vibrationally Relaxing Flow of N₂ Past an Infinite Cylinder. *Journal of Thermophysics and Heat Transfer*, vol. **11**, no.(1), 1997; pp. 27-35.
- [82] Tennekes H, Lumley JL. *A First Course on Turbulence*. IBM Univers Medium; Boston, Massachusetts 1972.
- [83] Spalart PR, Allmaras SR A One-Equation Turbulence Model for Aerodynamic Flows. *AIAA Paper*; January 1992; pp 439.
- [84] Baldwin BS, Barth TJ. *A One-equation Turbulence Transport Model for High Reynolds Number for Wall-Bounded Flows*. NASA TM 102847, 1990.
- [85] Schlichting, H. *Boundary Layer Theory*, McGraw-Hill: New York, 1979.
- [86] Jiang YT, Damodaran M, Lee KH. High Resolution Finite Volume Computation of Turbulence Transonic Flow Past Airfoils. *AIAA Journal*, vol. **35**, no.(7), July 1997; pp 1134-1142.
- [87] Raman IR. http://neon.otago.ac.nz/chemlect/chem306/pca/IR_Raman/

Hyperphysics, Principal Component Analysis, University of Otago, New Zealand,
2007

VITA

Name: Sunny Jain

Address: H.R. Bright Building, Rm. 631B
3141 TAMU
College Station, TX 77843-3141

Education: B.Tech., Aerospace Engineering, Indian Institute of Technology Bombay,
2005
M.S., Aerospace Engineering, Texas A&M University, 2007